LABORATORY ANALYSES OF METEORIC DEBRIS IN THE UPPER STRATOSPHERE FROM SETTLING BOLIDE DUST CLOUDS

F.J.M. Rietmeijer[1], V. Della Corte[2], M. Ferrari[2], A. Rotundi[2,3], R. Brunetto[4]

[1]Department of Earth and Planetary Sciences, MSC03 2040, 1-University of New Mexico, Albuquerque, NM 87131-0001, USA; fransjmr@unm.edu

[2]Istituto di Astrofisica e Planetologia Spaziali – INAF, Via del Fosso del Cavaliere, 100, 00133, Roma, Italy; vincenzo.dellacorte@iaps.inaf.it

[2]Istituto di Astrofisica e Planetologia Spaziali – INAF, Via del Fosso del Cavaliere, 100, 00133, Roma, Italy; marco.ferrari@iaps.inaf.it

[2,3]Istituto di Astrofisica e Planetologia Spaziali – INAF, Via del Fosso del Cavaliere, 100, 00133, Roma, Italy AND Dipartimento di Scienze Applicate, Università degli Studi di Napoli "Parthenope", CDN, I C4, 80143, Napoli, Italy; rotundi@uniparthenope.it

[4]Institut d'Astrophysique Spatiale, CNRS, UMR-8617, Université Paris-Sud, bâtiment 121, F-91405 Orsay Cedex, France; rosario.brunetto@ias.u-psud.fr

ABSTRACT: Bolide and fireball fragmentation produce vast amounts of dust that will slowly fall through the stratosphere. DUSTER (Dust in the Upper Stratosphere Tracking Experiment and Retrieval) was designed to intercept the nanometer to micrometer meteoric dust from these events for laboratory analyses while it is still in the upper stratosphere. This effort required extraordinary precautions to avoid particle contamination during collection and in the laboratory. Here we report dust from the upper stratosphere that was collected during two campaigns one in 2008 and another in 2011. We collected and characterized forty five uncontaminated meteoric dust particles. The collected particles are alumina, aluminosilica, plagioclase, fassaite, silica, $CaCO_3$, CaO, extreme F-rich C-O-Ca particles, and oxocarbon particles. These particles are found in friable CI and CM carbonaceous chondrite, and unequilibrated ordinary chondrite meteoroids that are the most common source of bolides and fireballs. The oxocarbons have no meteorite counterparts. Some F-bearing $CaCO_3$ particles changed shape when they interacted with the ambient laboratory atmosphere which might indicate their highly unequilibrated state as a result of

fragmentation. Equilibrium considerations constrain the thermal regime experienced by the collected particles between ~2000°C and ~1000°C, as high as 3,700^{o}C and as low as ~650°C after 9 secs, followed by rapid quenching (μs) to below 1,600^{o}C, but equilibrium conditions during these events is most unlikely. So far the observed thermal conditions in these events put the temperatures between ~4,300^{o}C and ~430°C for 5 seconds and high cooling rates. Such conditions are present in the immediate wake of meteors and fireballs.

1. INTRODUCTION

Meteoric dust trains and persistent dust clouds can linger for hours until they are sheared apart by upper atmospheric winds during continued sedimentation in the mesosphere and stratosphere. This dust is due to fragmentation of meteorite-dropping bolides and fireballs when decelerating in the atmosphere, and interacting with the ambient atmosphere while still entrained inside hot thermally-evolving dust trains (Fig. 1). Lingering persistent dust clouds can be traced settling in the atmosphere until they are dispersed by the upper atmospheric winds. This meteoric dust is fundamentally different from meteoric smoke particles that are the result of photolysis-driven oxidation of mesospheric metals (Plane, 2003), *viz*. Na, K, Ca, Fe and Mg, deposited between ~85-110 km altitudes (McNeil et al., 1998; Murad and Williams, 2002; Janches et al., 2009). The resulting meteoric metal-oxide molecules become the nuclei of noctilucent cloud particles that can be traced falling in the stratosphere (Hervig et al., 2009, 2012; Neely et al., 2011) and well into the upper troposphere (Cziczo et al., 2001).

Figure 1: Smoke train of the Chelyabinsk bolide with the double plumes clearly visible. (Photo: Nikita Plekhanov,
Source:http://en.wikipedia.org/wiki/Chelyabinsk_meteor#/media/File:Chelyabinsk_meteor_trace_15-02-2013.jpg)

Bolides, *i.e.* meteors brighter than -17 magnitude, and fireballs, *i.e.* meteors brighter than -8 magnitudes, are unpredictable events (Ceplecha et al., 1999). We will use these terms interchangeably.

The well documented meteoroid-meteor-meteorite sequence of the asteroid 2008 TC$_3$ on its pre-entry trajectory, its fireball stage, and delivery and recovery of the Almahata Sitta meteorite was the "perfect" fireball (Jenniskens et al., 2009; Millera et al., 2013). It was possible to locate its source in the asteroid belt. With the increased use of cell-phones, dashboard and security cameras, and the Internet these events receive ever increasing world-wide coverage that triggers teams of experts to rush in and conduct eye-witness interviews, collect video footage and search for surviving meteorite fragments. There were four well-documented meteorite-dropping events between 2010 and 2015 (Jenniskens, 2013), *viz*. the Križevci meteorite (Meteoritical Bulletin Database) and the Sutter's Mill (Jenniskens et al., 2012), Novato (Jenniskens et al., 2014) and Chelyabinsk (Borovička et al., 2013; Popova et al., 2013) meteorites but they are only a fraction of these very bright meteors.

Fireballs experience fragmentation events along their trajectory, sudden disintegration (Klekociuk et al., 2005), and the formation of incandescent dust trains and clouds, before reaching 'rest' velocity and the onset of ballistic fall of remaining fragments of recoverable meteorites, as well as the formation of persistent dust clouds, *e.g.* the Morávka (Borovička and Kalenda, 2003) and Tagish Lake (Brown et al., 2000) fireballs. Since ordinary chondrite meteorites make up 81% of all meteorite 'falls' and 93% of all meteorite 'finds' worldwide (*cf*. Rietmeijer, 2002) it stands to reason that most bolides and fireballs should have an ordinary chondrite bulk composition. This is the case, witness the Chelyabinsk LL5 ordinary chondrite (Popova et al., 2013), Novato L6 ordinary chondrite (Jenniskens et al., 2014) and Morávka H5-6 ordinary chondrite (Borovička et al., 2003) bolides. A small fraction of fireballs will have rare carbonaceous chondrite compositions such as the Tagish Lake CI-CM carbonaceous chondrite (Brown et al., 2000), reclassified as an ungrouped Type 2 carbonaceous chondrite (Zolensky et al., 2002), and Sutter's Mill CM carbonaceous regolith breccia (Jenniskens et al., 2012). The thermal conditions and timescales of the physiochemical processes inside these debris-laden trains are poorly known but recently data became available (Borovička and Charvát, 2009; Popova et al., 2013).

Qualitatively, the event starts with rapidly rising temperatures causing near-instantaneous evaporation and flash-melting of the smallest dust and the survival of the largest grains. Following peak heating, ultrafast vapor condensation and ultrafast melt quenching will probably produce newly formed compounds that will mingle with any surviving dust and dust fragments. Surviving dusts might show signs of thermal erosion (Rietmeijer et al., 2003). Ultrafast evaporation and melting followed by ultrafast quenching tends to favor dissipative behavior causing the formation of metastable eutectic compounds (Nuth et al., 2000; Rietmeijer and Nuth, 2012). It is uncertain to what extent the surviving and newly-formed non-equilibrium dust particles may interact with atmospheric nitrogen, oxygen (*incl*. ozone) and water entrained in the trains of these fireball events. These events are still very much targets-of-opportunity especially with regard to the physiochemical processes experienced by the copious amounts

of dust inside their active trains but all of it will settle through the atmosphere while being dispersed. It should be possible to intercept some of this dust while it is still high in the atmosphere. Given the kinetically-controlled interactions inside dust-carrying bolide trains the settling dust particles may be an unpredictable mixture of original, modified and newly-formed dust.

The stratosphere above the stratospheric aerosol layer at 30 km altitude (Renard et al., 2008) is a prime environment for collecting the sub-micron fraction of meteoric dust from bolide disintegration events. Also, most dust from anthropogenic sources, *e.g.* soot from commercial air traffic jet fuel burning (Blake and Kato, 1995) and massive biomass burnings, and natural sources, such as major dust storms and most volcanic activities, are primarily contained below these altitudes. Some fraction of the very fine ash, 0.5 to ~50 μm in diameter, entrained in rising ejecta plumes from eruptions of major magnitudes, *e.g.* Mt. Pinatubo and El Chichón, may reach the upper stratosphere (Rose and Durant, 2009). It is only prudent to avoid the immediate aftermath of such events when planning extraterrestrial dust collections.

This paper reports the laboratory analyses of stratospheric dust collected in the upper stratosphere at the northern hemisphere in 2008 and 2011 between 30 and 40 km altitude (~12 to 3 mbar) by DUSTER (Dust in the Upper Stratosphere Tracking Experiment and Retrieval). DUSTER was developed with stringent contamination controls to insure a high level of confidence that the reported dust particles were in fact present in the stratosphere during the times of collection at the reported altitudes. Proof-of-concept of DUSTER's operational and laboratory protocols was provided by the successful collection and laboratory characterization of CaO and CaF_2 nanograins that were arranged in the delicate "bunch-of-grape" particles that is characteristic of rapidly quenched vapors or liquids (Della Corte et al., 2013).

2. EXPERIMENTAL PROCEDURES

2.1 Dust collector

This balloon-borne instrument for non-destructive dust collection in the upper stratosphere was designed to track and document all particles on the collector surfaces during pre- and post-flight laboratory procedures with the differences being the particles that were present along its stratospheric trajectory. DUSTER is a combination of collector hardware and laboratory protocols. The following is a summary of design and laboratory protocols to ensure cleanliness at all stages of collector handling by taking precautions to ensure high-quality contamination control with the ability to recognize contaminant particles when they occurred (Della Corte et al., 2012, 2014).

DUSTER relies on inertial-impact capture of dust particles between 200 nm to 40 microns at 7 m/s directly onto a clean substrate with no need of sticking material. The collection chamber houses two collectors, (1) the "actual collector" that is opened only when the intended sampling altitude is reached,

and (2) the "blank collector". The "blank collector" which is identical to the "actual collector" is never exposed directly to the airflow. It serves as a monitor of particle contamination during all pre- and post-flight operations that were always conducted inside a class-100 clean room. All mechanical parts are cleaned in an ultrasonic bath of isopropyl alcohol prior to assembly inside the class-100 clean-room. The entire assembly of the actual collection and blank chambers is sealed by two UHV (Ultra-High Vacuum) valves, that is, one connected to the inlet pipe; the other one to the pumping system. The identical collection substrates in the actual and blank collectors each consist of standard TEM (Transmission Electron Microscope) grids covered by holey-carbon thin-film for dust deposition. Each set of TEM grids was housed, but in slightly different configurations, for the 2008 (Fig. 2a) and in the 2011 (Fig. 2b) collections, in a custom-made mechanical holder that consists of a stainless steel base with a pin to fix it inside the FE-SEM (Field Emission Scanning Electron Microscope) chamber for particle analyses. The chamber with both collectors is sealed off from the environment by two automated UHV valves that, when DUSTER has reached collection altitude, are opened by tele-command or on-board software. Prior to descent the collecting chamber seals off automatically.
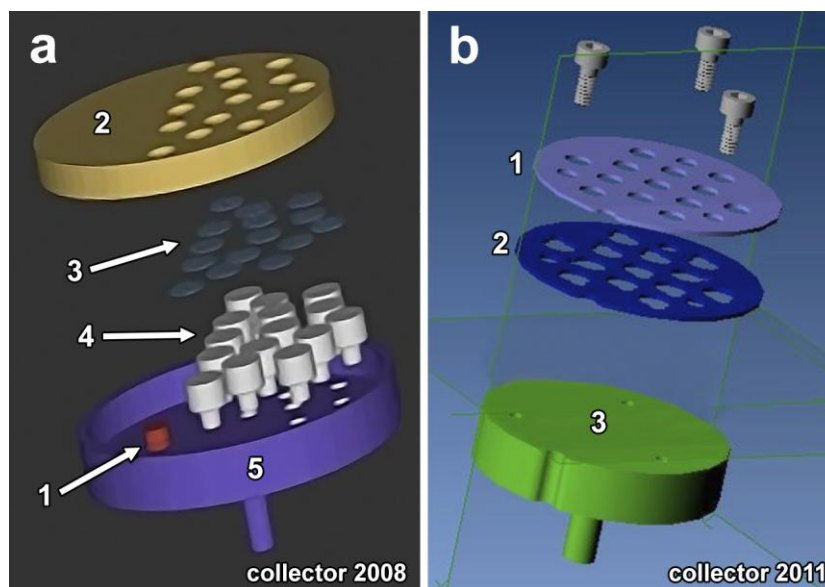

Figure 2: An exploded views of the assemblies holding the substrate for the TEM grids. In a) The 2008 configuration with (1) a screw fixing the gold plated holed-mask to the external stainless steel frame; (2) the gold plated holed-mask; (3) the TEM grids; (4) stainless steel pins and (5) the external stainless steel frame of the assembly and in b) the 2011 configuration wherein the TEM grids (not shown) are sandwiched between the two holed discs (1,2) mounted on a round stainless steel base (3).

Prior to integration in the collecting and blank chambers the entire surface of each set of TEM grids already mounted in the actual and blank collectors was characterized using automated high resolution FE-SEM imaging. A complete scan of an entire collector produces about 150,000 images that are electronically processed into a mosaic of each individual TEM grid with a spatial resolution to detect

particles >100 nm. FE-SEM scanning of the entire collectors is performed before they are mounted into DUSTER and after the flight. The collecting and the blank chambers are open only during sampling at altitude when both collectors are exposed to the same environment. Comparing the mosaics of the pre- and post-flight collector scans reveals all "new" particles following stratospheric flight. The DUSTER configuration ensures that no stratospheric particles can reach the blank collector during active sampling when the blank collector is in contact with the air present in the collection chamber acting as a monitoring surface. But, the 'air-flux + dust' is not directly impinging on the blank collector. Short of catastrophic failure, it is impossible that stratospheric particles will be deposited on the blank collector. Strict laboratory protocols are in place to identify collected stratospheric particles and to safeguard the integrity of *bona fide* stratospheric particles (Della Corte et al., 2014).

2.2. Laboratory analyses.

The chemical composition of each particle was obtained using a ZEISS Supra FE-SEM that is equipped with an Oxford INCA Energy 350 system with a Si(Li) INCA X-sight PREMIUM EDX (Energy Dispersive X-ray) detector that was operated at 10 or 20 keV accelerating voltages allowing detections of K_α peaks of elements with atomic numbers from 6 (C) to 22 (Ti), and L and M peaks of elements with atomic number >22. FE-SEM imaging of particles on the actual and blank collectors, while avoiding electric charging, was performed at either 2 kV or 4 kV accelerating voltages. All certified stratospheric particles were characterized using a combination of FE-SEM imaging and EDS analysis. For the 2008 collections the stainless steel pins (Fig. 2a; #4) became a Fe, Cr and Ni contamination source (Ciucci, 2011). Most analyses could be adjusted for this source contribution but others were relocated on clean TEM grids using a SEM-FIB FEI Helios 600 NanoLab with a high-resolution, high-magnification Elstar Schottky FEG for scanning electron microscopy (spatial resolution 0.7 nm at 15kV) with a high-resolution Sidewinder focused Ga^+ ion beam column for controlled, nanoscale-material addition and excavation with a Continuous Dynode Electron Multiplier detector (CDM detector). Platinum deposition used a metallo-organic gas ($C_9H_{17}Pt$) carrier for welding a subset of the collected particles onto the new substrate. This process precipitated variable amounts of carbon onto the particles and gave rise to the 1450 cm^{-1} FTIR (Fourier Transfer Infrared) the C=C bond. For EDS analyses of particles collected in 2011 all TEM grids with the stratospheric particles were removed from the collector. Thus there was no need for particle manipulation and welding onto a different substrate.

Sample contamination in the laboratory is an always present concern when handling small particles. In the case of DUSTER there is extensive photo documentation of each *bona fide* stratospheric particle. As a result, the presence of an unrelated particulate, *i.e.* an environmental contaminant, is immediately recognizable (Della Corte et al., 2014).

3.   OBSERVATIONS

3.1 Grain size distribution

Stratospheric dust in 2008 was collected drifting from Svalbard to Greenland (~78^0 N to ~72^0 N) during 21-24 June at 37-38.5 km altitude for 55h of continuous sampling, and a second collection drifting over northern Sweden (~67^0 N) on 11 April, 2011 at 31.6-33.7 km altitude for 2.8h of sampling (Della Corte et al., 2012). Forty-five stratospheric particles ranging from ~0.1 µm to 8.5 µm were collected during 57.8h of sampling (Fig. 3). Each particle is identified by its year of collection (D08; D11) plus a number assigned in the order in which it was identified on the collector. Gaps in the numerical sequence are due to contaminant particles. Particle D08-008 consists of three fragments but is counted as a single particle. The histogram does not include a biological particle that was collected in 2011 (Della Corte *et al*. 2014). About 65% of the nanoparticles have a sub-spherical shape; the remainder has elongated (cylindrical) shapes. Of the micrometer particles, 25% are sub-spherical; the rest have elongated shapes.
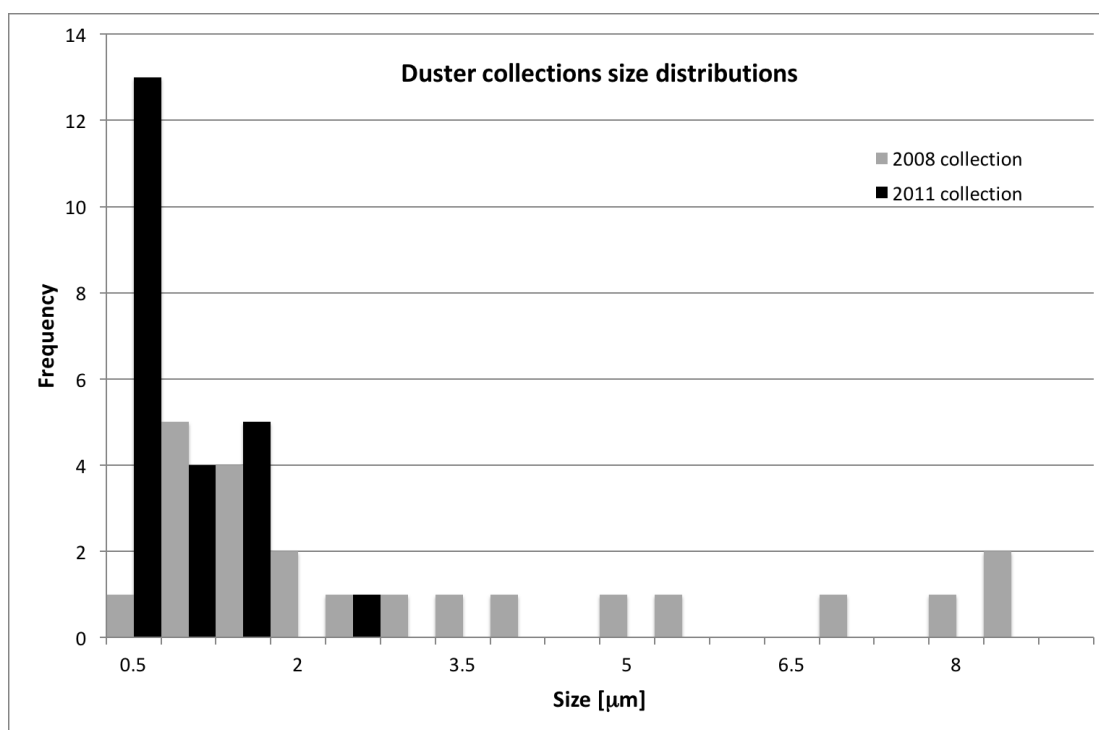
Figure 3: Distribution of the geometric mean diameters of the stratosphere particles collected in 2008 and 2011. The equivalent SQRT grain size is calculated as $(X^2 + Y^2)/2$ where X and Y are the short and long particle dimensions (see below).

The holey carbon thin-film that was the actual collecting surface has many holes with widely different shapes and sizes (Fig. 4a). Thus, an unknown number of stratospheric particles <400 nm may have been

deposited inside the collector main body (Fig. 4b) along with numerous smaller fragments <70 nm. While this seems plausible, if not likely, we don't know if it really happened. While we accurately scanned the collecting surface, *i.e.* the holey carbon films mounted in the collector as part of our standard procedures, we did not scan the surface below the collecting surface, *i.e.* stainless steel pins for the 2008 collection (Fig. 2a, #4) and the round stainless steel base for 2011 collection (Fig. 2b, #3) in pre-flight conditions. Thus, we cannot prove that particles that passed through the holey carbon film were collected during active sampling of the stratosphere. We may only speculate that some might, but we don't know. There are also numerous nanodroplets and rod shaped grains on the collector stainless steel surfaces (Fig. 4c). Similar looking rods, but of unknown composition, were found in collectors that sampled the stratosphere above 30 km. They were thought to have crystallized from a volatile, low-boiling point liquid that had adhered to the collector (Bigg et al., 1971).
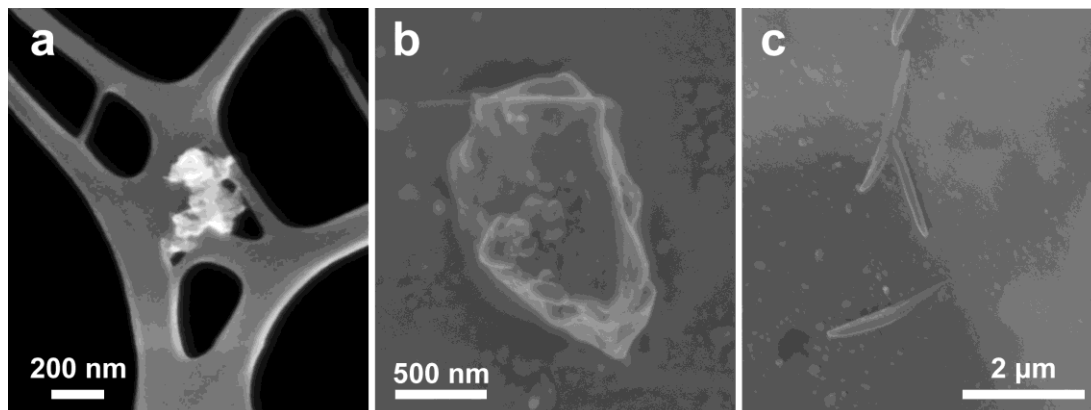
Figure 4: FE-SEM/SE images of (a) a small aggregate particle that missed the big holes in the holey carbon collection substrate in 2008; (b) a 400-nm stratospheric dust particle and (c) rod shaped nanoparticles (~2 x 0.2 μm) and numerous nanodroplets on the stainless steel surface of the collector.

3.2 Condensed stratospheric aerosols

A few of the largest particles collected in 2008 have random Na-K-Cl nanospots at their surface (Fig. 5). The very low abundances, *viz.* K = 0.44 ± 0.37 (range: 0.1-1.4 at.%), Na = 0.99 ± 0.7 (range: 0.3-4.1 at.%) and Cl = 0.3 ± 0.27 (range: 0.06-1.1 at.%), explain why not all three elements always co-occur. Such nanospots were rare on the grains collected in 2011. Sodium is abundant in the mesosphere below ~110 km altitude (Plane, 2003) and is found in meteoritic aerosols in the lower stratosphere (Murphy et al., 1998). Some IDPs falling through the atmosphere acquired a coating of atmospheric volatile elements (Jessberger et al., 1992) including K and Cl with a stoichiometric KCl composition (Rietmeijer, 1995). Sulfur, S = 0.5 ± 0.2 (range: 0.15-0.9 at.%), was found on one silicate and one silica-rich particle collected in 2008. Five out of 23 particles collected in 2011 had minor sulfur on their surface, S = 0.75 ±

0.4 (range: 0.2-1.4 at.%). Low-sulfur aerosols are expected for particles collected above the top of the stratospheric aerosol layer at 30 km altitude.
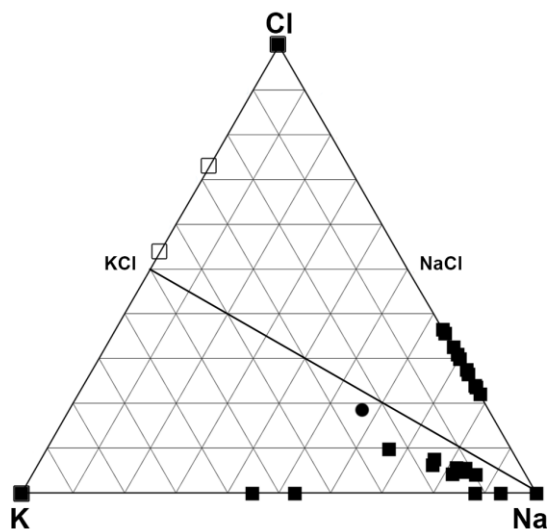

Figure 5: Na-K-Cl (atomic) abundances in patches on some stratospheric particles collected in 2008 (solid squares) and 2011 (open squares). The dot is the average Na-K-Cl composition found during 2008.

3.3. Grain sizes

Table 1 shows the measured sizes (microns) of all grains included in calculating the grain size distribution (Fig. 3) are arranged by particle type and in the order of first appearance in the text. At a glance this table offers a glimpse in the differences and similarities among the particles collected in 2008 at 37-38.5 km altitude in 2011 collected between 31.6-33.7 km altitudes.

Table 1: Grain size (microns) of stratospheric the particles collected by DUSTER in 2008 and 2011 discussed in this paper.

2008		2011	
		Alumina	
		D11-163	0.65 x 0.43
		D11-167	0.95 x 0.735
		D11-159	0.53 x 0.43
		Silicate and aluminosilica	
D08-014	3.0 x 1.85	D11-291	1.6 x 0.92
D08-008	8.5 x 3.9	D11-238	1.39 x 1.0
D08-011	3.5 x 1.6	D11-247	2.54 x 2.1
		Silica	
		D11-033	0.53 x 0.44
		D11-204	0.37 x 0.34
		D11-146	0.71 x 0.48
		D11-165	0.42 x 0.34
		D11-152	0.38 x 0.31
		D11-141	0 24 x 0.15

		D11-232	0.17 x 0.14
		D11-229	0.115 x 0.07
		D11-058	0.37 x 0.28

<div align="center">Oxocarbons</div>

D08-026	0.9 x 0.47	D11-244	1.23 x 1.19
D08-032	0.52 x 0.42	D11-288	0.18 x 0.17
D08-017	1.85 x 0.5	D11-150	0.225 x 0.10
D08-029	0.87 x 0.54	D11-143	0.24 x 0.24
D08-030	0.84 x 0.47	D11-161	0.43 x 0.36
D08-033	0.47 x 0.41		

<div align="center">Mantled aggregate</div>

D08-005	8.2 x 4.4		

<div align="center">CaO</div>

		D11-070	1.28 x 0.72
		D11-285	1.30 x 0.79
		D11-279	1.11 x 1.07

<div align="center">CaCO$_3$</div>

D08-006	7.75 x 5.8		
D08-009	5.4 x 3.9		
D08-007	6.6 x 6.1		

<div align="center">extreme F-rich C-O-Ca</div>

D08-034	5.0 x 2.1		
D08-035	1.2 x 1.1		
D08-031	0.56 x 0.45		

<div align="center">morphing F-bearing CaCO$_3$ particles</div>

D08-012	3.13 x 1.65		
D08-015	2.27 x 1.41		
D08-019	1.14 x 1.00		
D08-021	1.47 x 1.42		
D08-023	1.66 x 0.86		
D08-028	1.07 x 0.44		

4   PARTICLES COLLECTED IN 2008

4.1.1 Silicate and aluminosilica particles

These particles are a small fraction of the collected particles. Particle D08-014 with a somewhat rough, scalloped surface may be a compact aggregate (Figs. 6a). Its chemical composition is homogeneous fassaite (Table 2). Magnesium is a trace element (<0.8 at.%). The FTIR band at 1050 cm^{-1}, assigned to Si–O–Si antisymmetric stretch or Si (Al)-O stretching vibrations, supports its silicate nature. Small low-F Ca-phosphate (F = 1.3 at.%) spots are present at the surface but these could not be linked to specific features as shown in the FE-SEM/BSE image (Fig.6b).
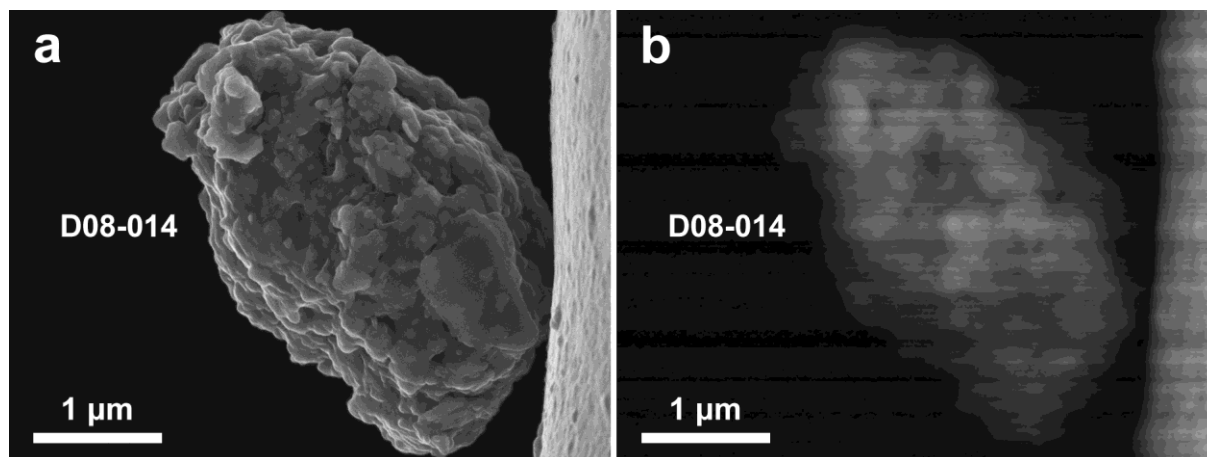
Figure 6: FE-SEM/SE image of particle D08-014 (a) and its FE-SEM/BSE image showing an aggregate texture (b). The webbed background in the SEM images is the holey carbon collection substrate which will appear in other images in this paper.

Table 2: Fassaite (pyroxene) composition (Fe$_2$O$_3$ was calculated)

	Oxide wt.%	Structural formula (O = 6)
SiO$_2$	51.4	Si 1.92
Al$_2$O$_3$	9.8	Al 0.08
		2.00
		Al 0.45
CaO	26.4	Ca 1.06
FeO	10.4	Fe^{2+} 0.33
Fe$_2$O$_3$	2.9	Fe^{3+} 0.08
Total	100.0	1.92
		(Fe^{3+}/Fe^{3+} + Fe^{2+}) = 0.2

Particle D08-008 is an aggregate of angular fragments (Fig. 7a). Fragment 008a is a massive shard-like particle that is a mixture of F-bearing CaCO$_3$ and CaO grains. The Raman feature (1080 cm^{-1}) supports calcite or aragonite (De Angelis et al., 2011). The FTIR band between 1700-1900 cm^{-1} can be assigned to the C=O, carbon-oxygen double bond (Ciucci, 2011), that in our samples confirms the presence of carbonates. This fragment contains 3 at.% fluorine with a single "hot spot" of 12 at.%. Fragment 008b is F-free.
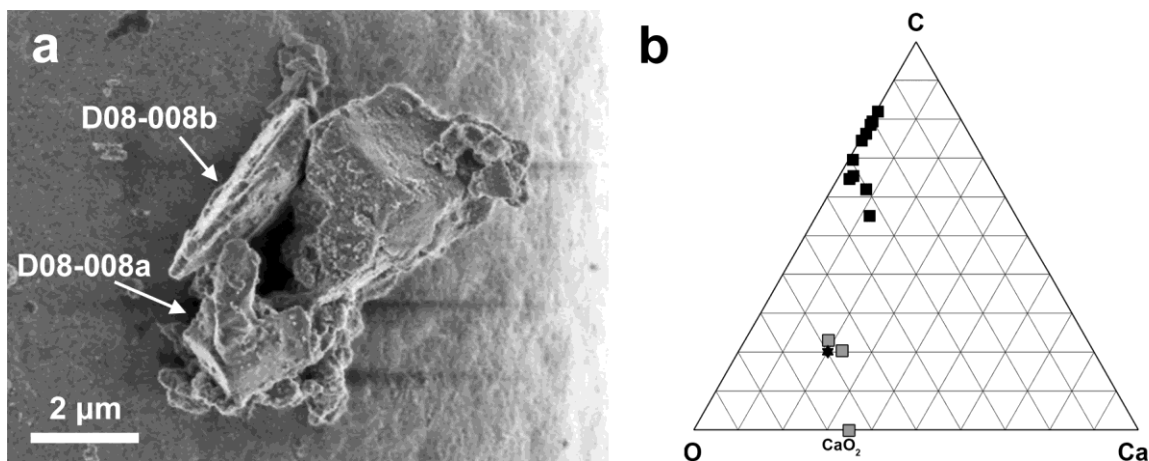
Figure 7: FE-SEM/SE image of particle D08-008 showing the two analyzed fragments (a), and (b) the compositions of both fragments in the C-O-Ca diagram (grey squares: fragment 008a; black squares: fragment 008b). The solid star represents stoichiometric $CaCO_3$; it will appear in other figures.

Fragment 008b is chemically heterogeneous albite (*Ab*)-anorthite (*An*) plagioclase with an average Na/(Na+Ca) = 0.64 composition. This ratio ranges from *Ab* = 0.4 to *Ab* = 0.84 suggesting a patchy domain distribution. Random probing of the surface found rare areas with Al_2O_3 and $Al_2O_3.Na_2O$ compositions. One side it is covered by numerous (sub-)spherical nanograins and angular fragments, the largest being 1.2 μm x 1.0 μm) (Fig. 8) that are calcite or aragonite based on the Raman feature supports (De Angelis et al., 2011). A single small Ti-O grain is probably Ti-oxide Magnéli phase (Rietmeijer and Mackinnon, 1990).
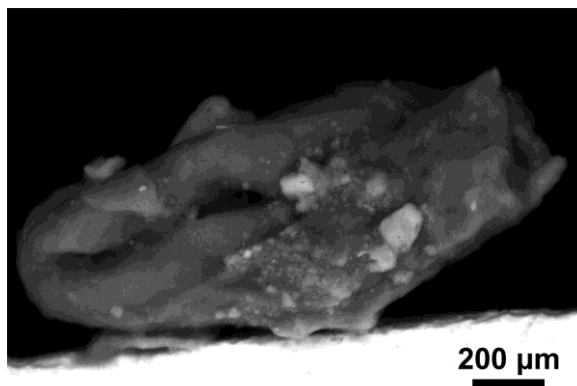
Figure 8: FE-SEM/BSE image of fragment D08-008b that is partially covered by angular Ca-carbonate fragments and nanospheres (bright grains).

Particle D08-011 is a thin aluminosilica flake (3.5 x 1.6 μm) with regular edges of a crystalline material (Fig. 9a). The surface is covered by a layer that shows what appear to be devolatilization cracks and pores (Fig. 9b, c). The measured compositions are no match for a stable alumina phase or metastable aluminosilica phase (Fig. 10; black dots). After extracting the right amount of oxygen from its

compositions to be on the Al_2O_3-SiO_2 tie-line (Fig. 10, open squares), the re-normalized composition was SiO_2 = 41.8 wt.%, Al_2O_3 = 21.3 wt.% and C = 36.9 wt.%. The C-free re-normalized composition matches a metastable aluminosilica compound (Rietmeijer and Karner, 1999). After these adjustments an excess in oxygen and carbon remains that by default must be the layer composition which on this aluminosilica particle has an O/(O + C) = 0.1(at.) ratio.
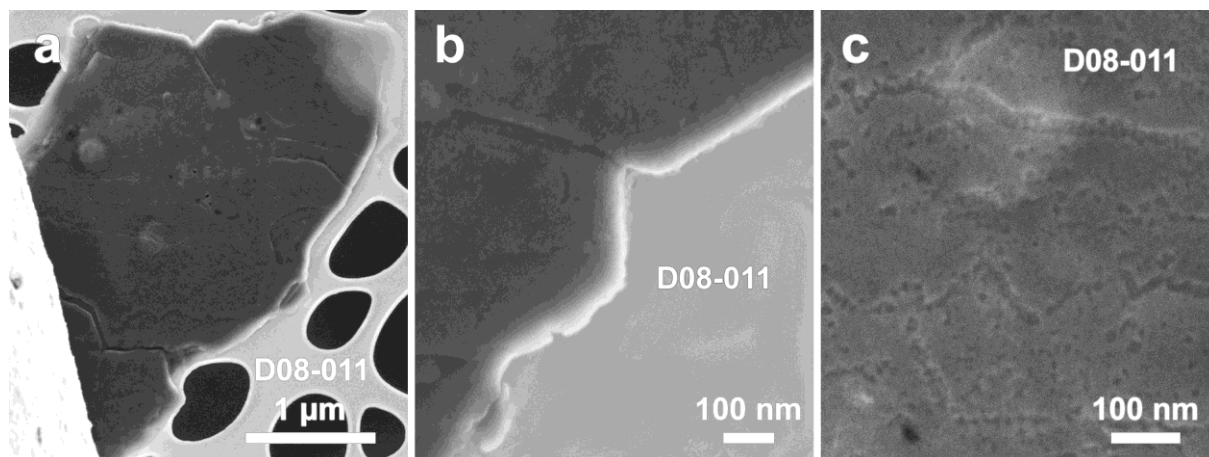
Figure 9: FE-SEM/SE images of particle D08-011(a) as found on the collector, (b) crystal-like edges and surface layer, and (c) pores and cracks in the surface layer.
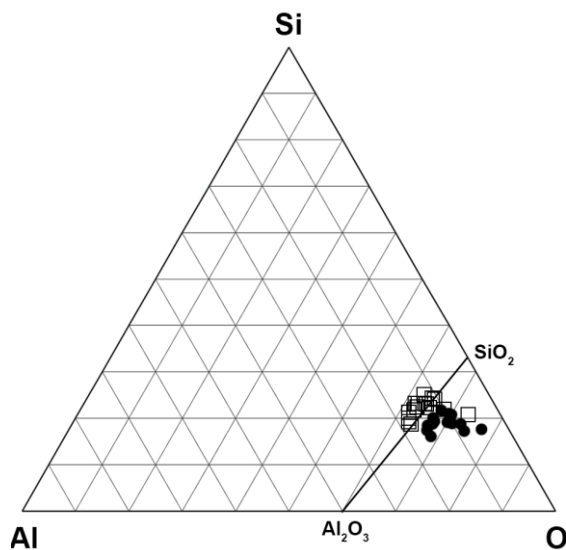
Figure 10: Si-Al-O (at.) compositions of particle D08-011 as measured (black dots) and adjusted for "excess" oxygen (open squares) located on the Al_2O_3-SiO_2 tie-line.

The silicate particles (D08-014; D08-008b) are nominally C-free solids. Yet their EDS data show carbon which could be from a pure carbon surface layer on the fassaite particle and a C-O surface layer

on particle D08-008b (Fig. 7b). We will show in the following that all particles collected in 2008 and 2011 have a C-O carbon surface layer. Melted particles assimilated the layer composition.

4.1.2 Oxocarbons

The C-O particles D08-026 and D08-032 are three-dimensional aggregates that look significantly different the other C-O particles (Fig. 11). Particle D08-017 is a cluster of spherical nanograins. Particle D08-029 is a single ~ 200 nm sphere on top of a sheeted material with smaller layered grains while D08-030 is a smooth folded sheet-like particle (Fig. 11). These morphologies suggest they are quenched-liquid particles. These three C-O particles show a trace amount of Si (<1 at.%) (Fig. 12) that could be picometer silica grains that acted as nucleation centers. Particle D08-033 is an open aggregate of nanograins some of which were deposited on the holey-carbon thin film (Fig. 11; inset). This sequence of particle morphology is consistent with melting of solid C-O particles. These C-O melts covered all other 2008 particles.
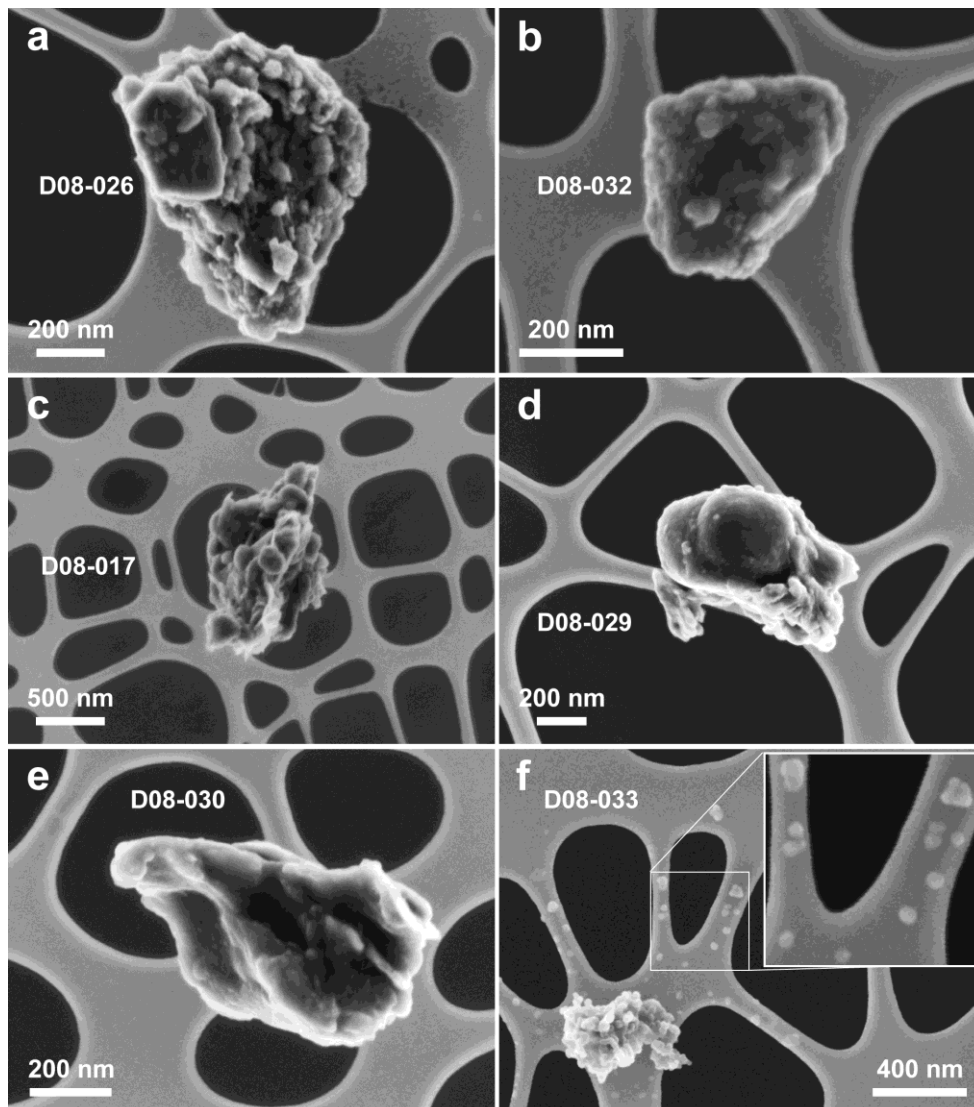
Figure 11: FE-SEM/SE images of oxocarbon particles arranged in order of increased melting from top-left to the bottom row right.
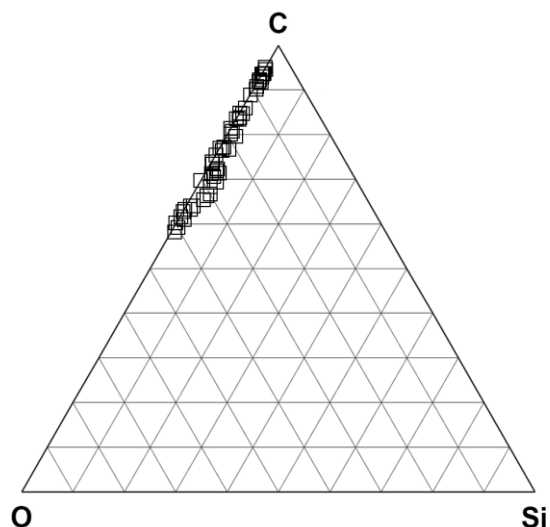
Figure 12: C-O-Si (at.%) diagram showing the compositions of all quenched liquid and vapor condensed particles that are linked to an oxocarbon surface layer present on all particles collected in 2008.

4.2. Mantled aggregate particles

Particle D08-005 is a porous aggregate of nanograins contained within a carbon film (Fig. 13a) with associated angular grains. After relocation the entire cocoon with nanograins was lost leaving a cluster of angular fragments (Fig. 13b) of low-F (2 at.%) fragments with an approximate Ca-carbonate stoichiometry. The co-presence of the porous aggregate and the fragments is probably fortuitous but their compositions are consistent with those of similar particles that will be discussed below.
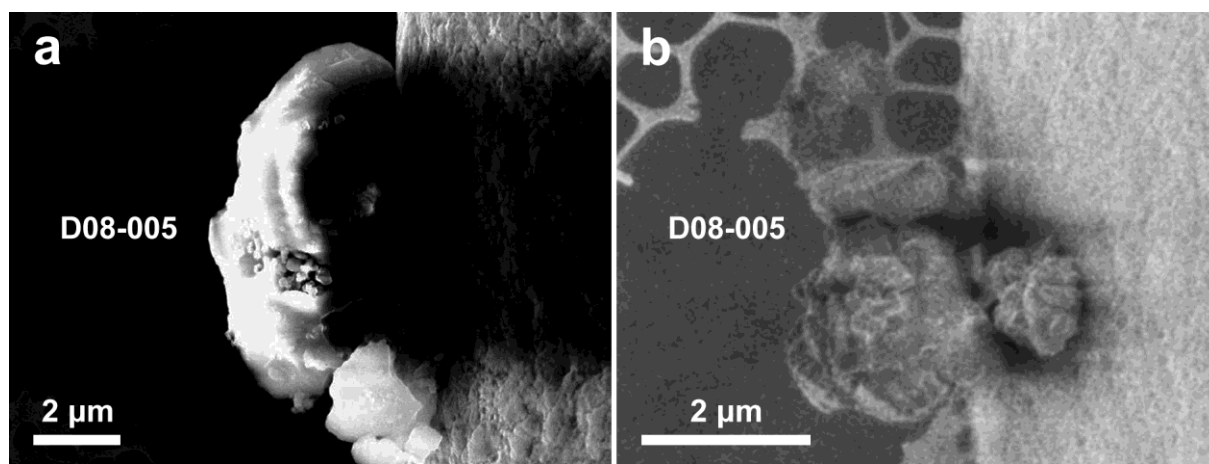
Figure 13: FE-SEM/SE images of particle D08-005 as initially collected (a) and after the EDS analyses when the cocoon with its content had disappeared (b).

4.3. CaCO₃ particles

Particle D08-006 is a compact aggregate of highly angular massive fragments (Fig. 14a). Particle D08-009 is another compact aggregate of angular and platy fragments. Spherical and platy nanometer grains are dispersed across the surface (Fig. 14b). The cubic shape of particle D08-007 suggests an originally euhedral grain as can still be seen in its massive lowermost part (Fig. 14c). The upper part is an open aggregate of irregularly shaped, angular and (sub-)rounded, fragments. The ample void space suggests significant loss of material. Particles D08-006 and D08-009 are both low-F (1-4 at.%) Ca-carbonate; particle D08-007 contains 16 at.% fluorine. The EDS data support the presence of CaO, from carbonate decomposition, and CaO_2. The CaO_2 composition probably indicates $Ca(OH)_2$ due to post-collection aging of collected carbonate particles (see below). The largest particles experienced significant fragmentation. The FTIR C-F (800-1000 cm^{-1}) features for particles D08-007 and D08-009, and the Raman features at 1080 cm^{-1}, which can be assigned to calcite or aragonite ($CaCO_3$), for particle D08-006 (De Angelis et al., 2011) are consistent with the EDS data (Fig. 15).
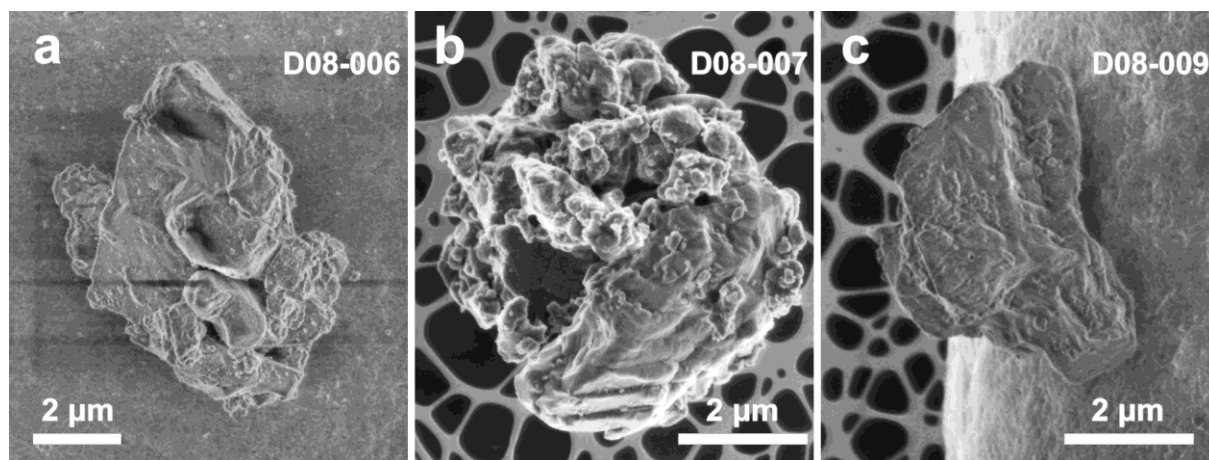
Figure 14: FE-SEM/SE images of particles D08-006 (a), D08-009 attached to the supporting grid (b), and D08-007 (c). They are the largest Ca-carbonate particles collected in 2008 (Table 1).
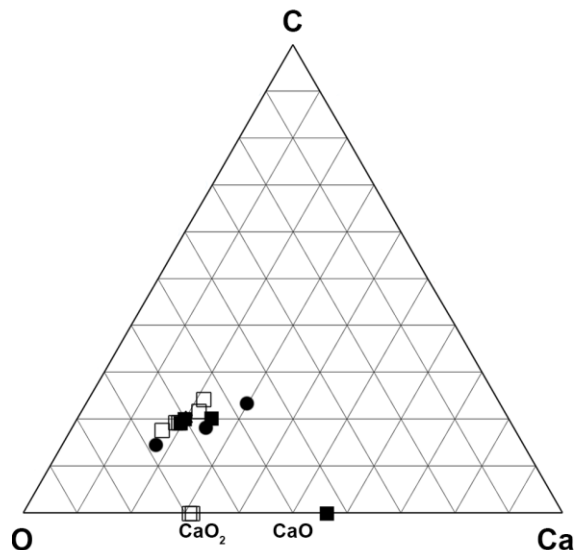
Figure 15: C-O-Ca (at.%) compositions of particles D08-006 (open squares), D08-007(solid squares) and D08-009 (dots).The star for stoichiometric calcite is hidden in the cluster.

4.4. Extreme F-rich C-O-Ca particles

Particle D08-034 is a chain-like aggregate of nanograins showing grain fusion (Fig. 16a). It is unique among the collected particles. Its morphology is typical of quenched-liquid nanodroplets due to liquid or vapor condensation (Rietmeijer et al., 2008; Rotundi et al., 1998). Particle D08-035 consists of smooth layers with both angular and spherical contours (Fig. 16b). They are the most F-rich particles collected (Fig. 17a). Vesicles, especially present in particle D08-035, suggest the presence of a C-O layer (Fig. 17b), which is supported by their compositions. A "bunch-of-grape" particle D08-031 consisting of pure CaO nanospheres is attached to a single 250-nm CaO sphere (Della Corte et al., 2013). Its morphology is also typical for liquid or vapor phase condensation. It is F-free which might suggest that particle formation and F-content are uncorrelated properties.
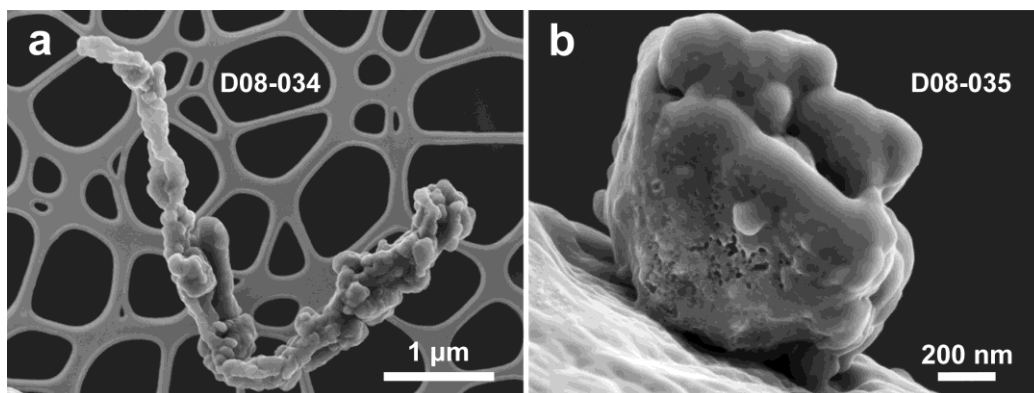
Figure 16: FE-SEM/SE images of extreme F-rich particles D08-034 (a) and D08-035 (b).
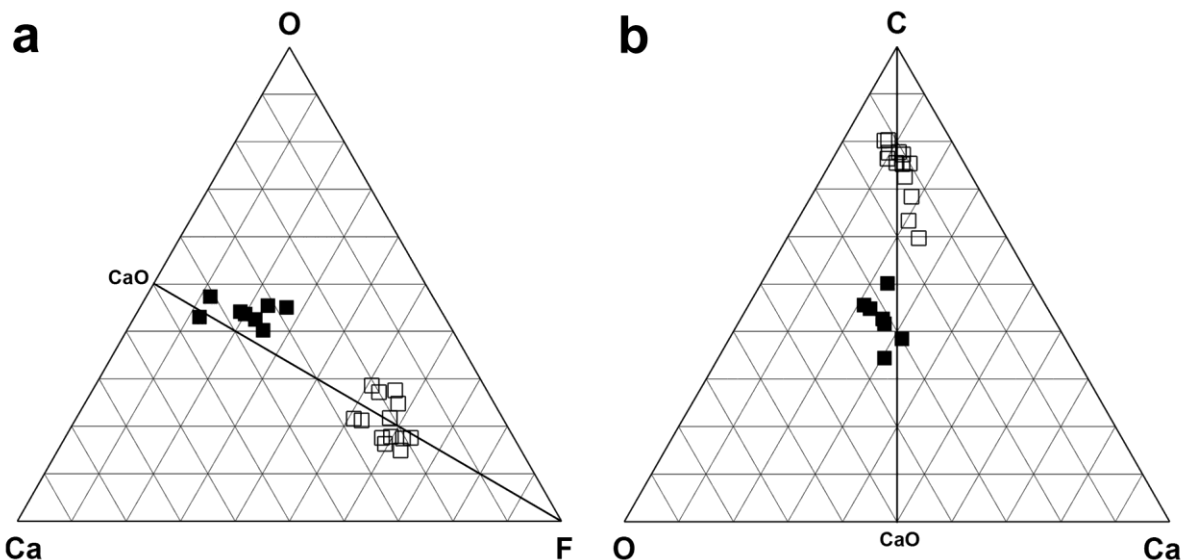
Figure 17: (a) O-Ca-F compositions of F-rich particles D08-034 (open squares) and D08-035 (solid squares) with Ca/(Ca+F) ratios of 0.3 and 0.6, resp., and (b) the C-O-Ca compositions on a mixing line between CaO particles and a partially assimilated oxcocarbon layer.

5   Morphing F-bearing $CaCO_3$ particles

Six carbonate particles that were first analyzed during October 2008 were revisited for additional imaging and re-analyses in April 2010, March 2011, and again in January 2012. During this time these particles had undergone significant changes in their appearances. Initially well-defined outlines and surfaces became smooth and featureless and developed a bubbly crust with occasional pores. Their equivalent SQRT grain sizes range from 0.8 μm to 2.5 μm which is smaller than the $CaCO_3$ particles describe above that are 4.6 μm, 6.4 μm and 6.9 μm in size. These changes were probably controlled by the surface-to-volume ratio of thermodynamically unstable particles. They were not due to exposure in the incident FE-SEM electron beam, or a FIB artifact. It is noted that FTIR spectra of several of these Ca-O-C particles showed an O-H (3200-3500 cm^{-1}) feature (Ciucci 2011), which provided a hint of this post-collection secondary process. The DUSTER storage protocol did not foresee chemical interactions between the collected particles and the humid ambient air in the laboratory in Naples (Italy). There are several pathways for this interaction of Ca-carbonate with atmospheric water, *viz.*

$CaCO_3 + H_2O = Ca(OH)_2 + CO_2$ (1) and

$H_2O + CO_2 \rightarrow H_2CO_3$ (2a) followed by $CaCO_3 + H_2CO_3 = Ca(HCO_3)_2$ (2b).
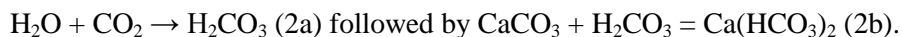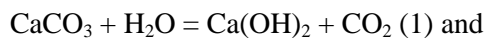
The product of the first reaction, $Ca(OH)_2$, cannot be detected by the EDS system that cannot detect hydrogen; it will reduce the input CaO_2 (Ca-peroxide) (Rietmeijer et al., 2008).

This morphing process is most spectacularly displayed by particle D08-012.The main particle is rather flat with a few angular platy grains on top (Fig. 18a). The main flat part shows a straight gash of unknown origin and many small pores (Fig. 18b). Initially the particle contours are rather sharp; after the

morphing process the particle dissolved into a massive blob that retained vestiges of the original shape (Fig. 18c) and ultimately only a trace of the original gash survived (Fig. 18d). The morphing process preserved the compositions expected for Ca-carbonate with a carbon surface layer (Fig. 19).
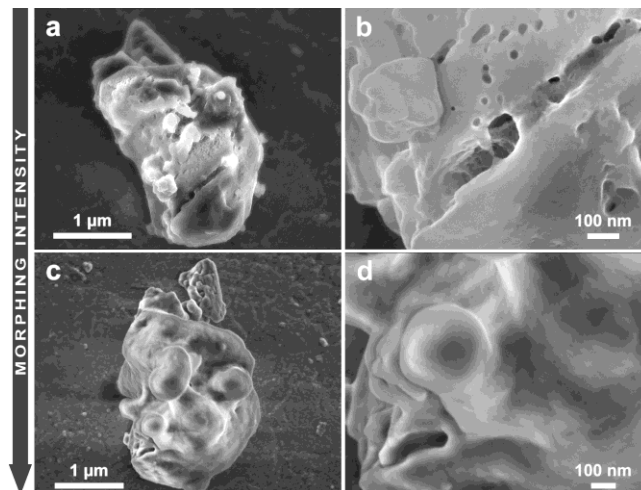
Figure 18: FE-SEM/SE images showing the morphing sequence of D08-012 beginning with the original particle (a) with its distinct gash (b), and (c) after complete morphing with a vestige of the original gash (d).
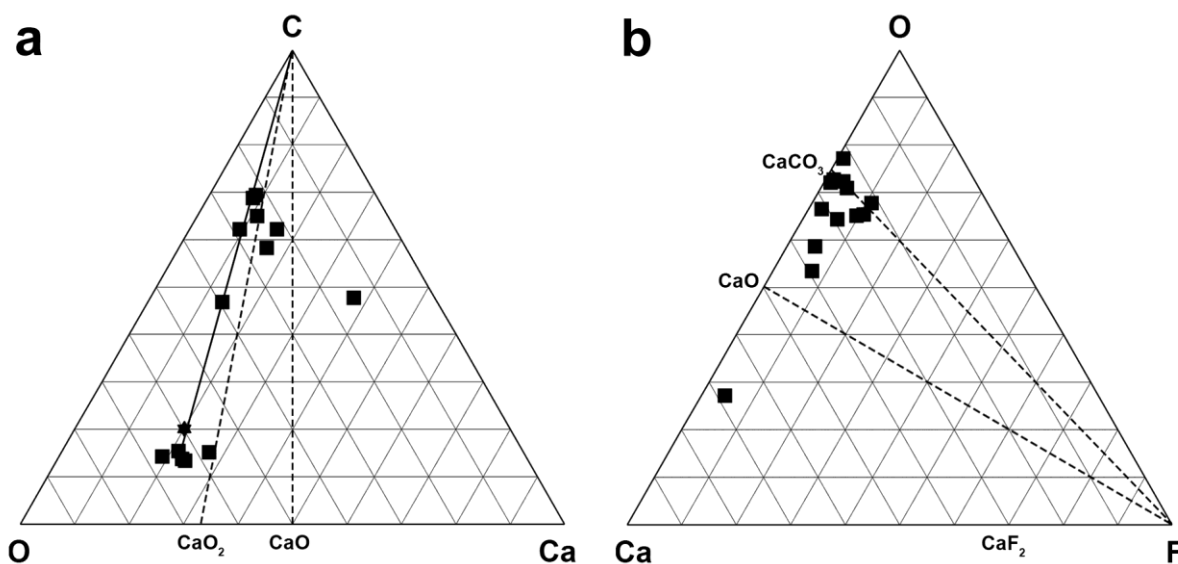
Figure 19: C-O-Ca compositions of morphed particle D08-012 (a) and stoichiometric Ca-carbonate (star), and the low-F O-Ca-F compositions (*b*).

The same morphing process also affected other particles that ultimately dissolved into amorphous blobs (Fig. 20). Morphing of the smallest particles may have started well before April 2010 when it was first noticed that some of the collected particles had developed surface blisters, *e.g.* particle D08-028 (Fig.

20). In a rare case, particle D08-015, the blister had an open pore at the top (Fig. 21). We speculated that these blisters mark the onset of the built-up of a gas phase. Particle D08-023 is actually two chemically homogeneous components, (1) a platy part decorated with smaller (sub-)spherical particles and (2) a compact cluster of rectangular prismatic and (sub-)spherical droplets.
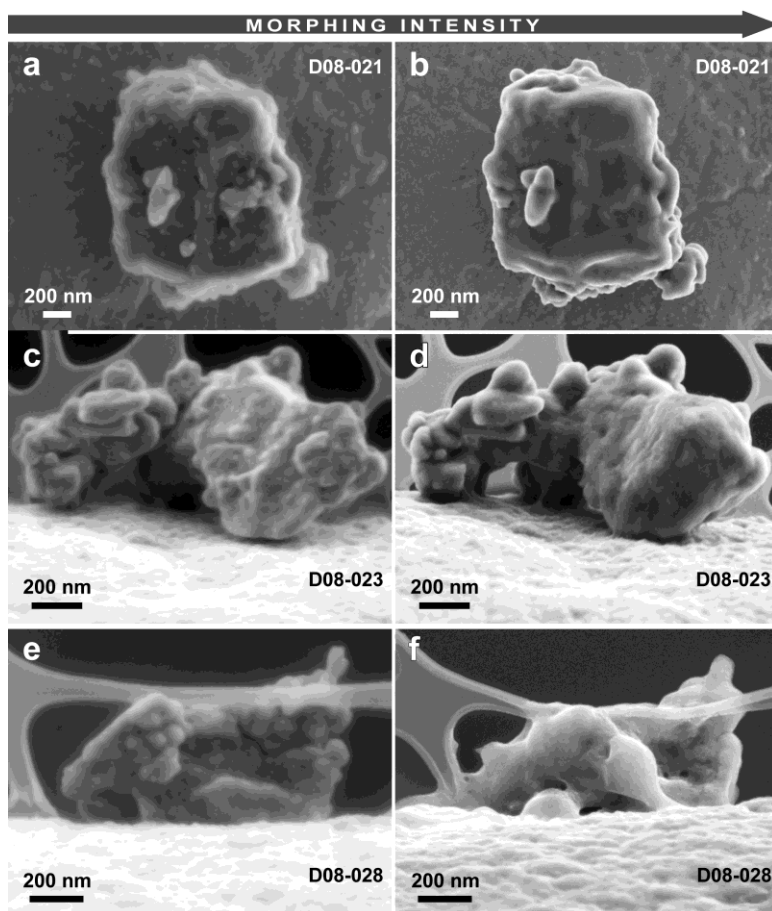
Figure 20: FE-SEM/SE images showing particle morphing due to interactions with the ambient humid atmosphere. Each row shows the particle as collected (left) and the final change due to morphing (right).
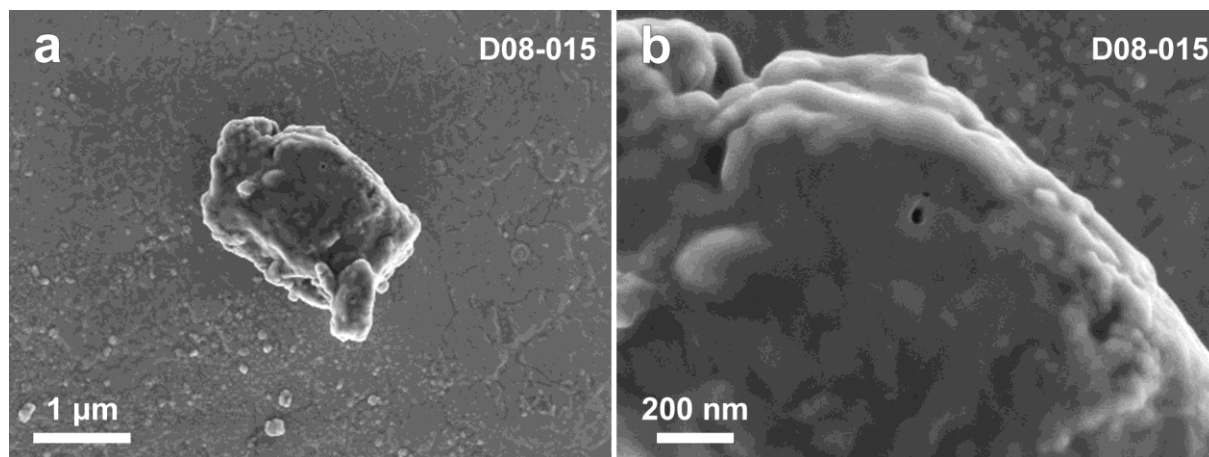
Figure 21: FE-SEM/SE images showing particle D08-015 (a) on which blistering caused an open pore (b).

The morphing process was chemically consistent with regard to C-O-Ca compositions (Fig. 22a) but there is a slight shift from F-free particles (D08-023, D08-028) to particle D08-012 with an average 2.25 at.% F-content, ranging from 0.8 to 4.0 at.% (Fig. 22b). Intermediate fluorine contents range from 0.8 to 3.1 at.% (average: 1.95 at.%).
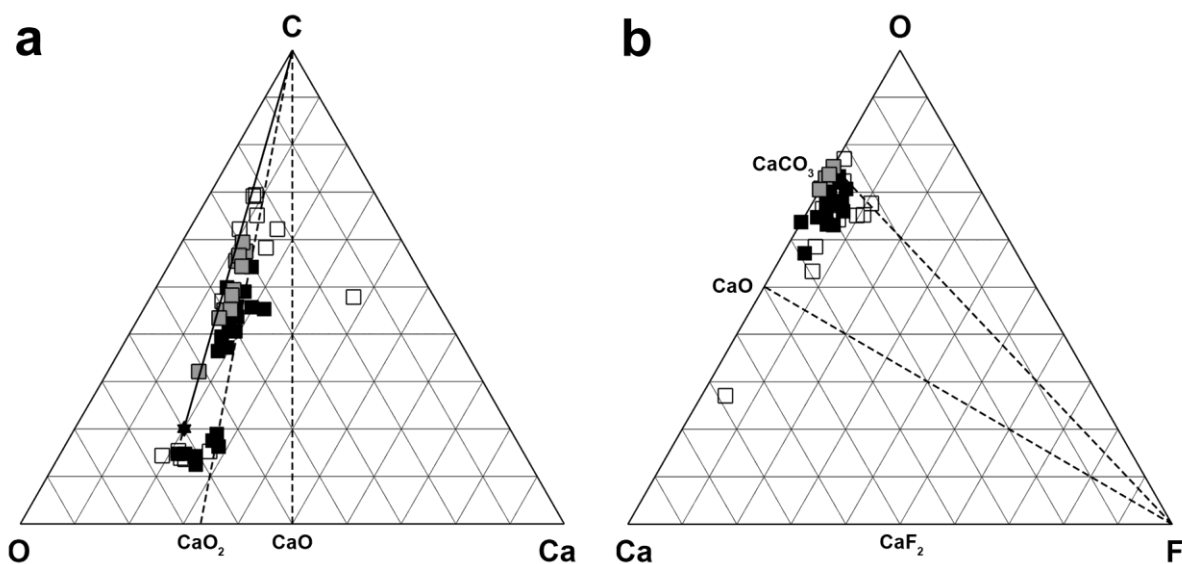
Figure 22: (a) C-O-Ca compositions of morphed particles, *viz.* high-F particle D08-012, (open squares), F-free particles D08-023 and D08-028 (gray squares), and morphed particles with intermediate fluorine contents (solid black squares), and (b) their O-Ca-F compositions.

6 PARTICLES COLLECTED IN 2011

6.1.1: Alumina particles

Particle D11-163 is a euhedral fragment (Fig. 23a). Particle D11-167 is just a thin flake (Fig. 23b). Both alumina particles have a carbon layer. Particle D11-159 (Fig. 23c) is a nondescript very thin flake with a slightly off-(pure) alumina composition; it also has a carbon layer (Fig. 24).
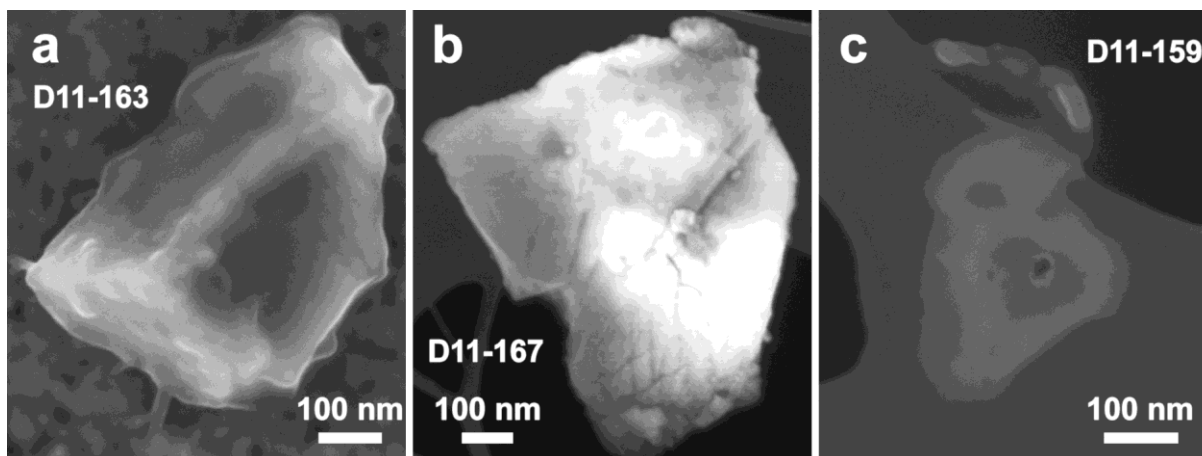
Figure 23: FE-SEM/SE images of alumina (Al_2O_3) particles: a) D11-163 a euhedral fragment; b) D11-167 a thin flake; c) D11-159 a nondescript very thin flake.
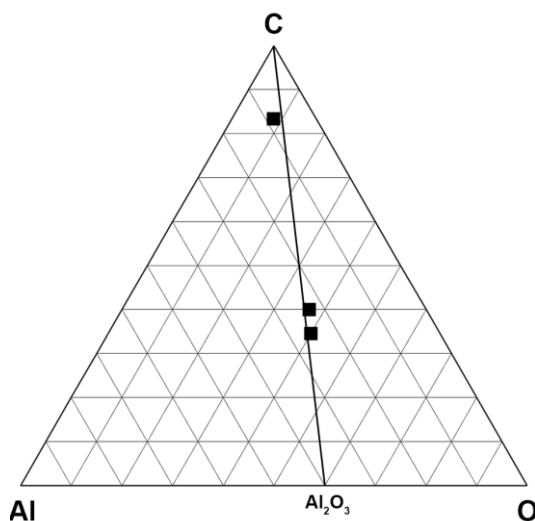
Figure 24: C-Al-Si (at.%) compositions of Al_2O_3 particles with a carbon layer in Fig. 23.

6.1.2. Aluminosilica particles

Particle D11-291 appears to be folded (Fig. 25). Small holes in this particle and in D11-238 suggest they are thermally annealed particles. Similar holes were observed during thermal annealing of amorphous magnesiosilica smokes (Rietmeijer et al., 2002). Particle D11-247 is a dense aggregate of (sub-)spherical grains with a trace of Ca (0.8 at.%) and 7.7 at.% fluorine. Calcium and fluorine could be from CaF_2 fragments or droplets. The low-Mg aluminosilica compositions of these grains are no match

for a specific mineral but they fit a mixture of mullite and metastable smectite-dehydroxylate ($Mg_6Si_8O_{22}$; Rietmeijer and Karner, 1999; Rietmeijer and Nuth, 2011) (Fig. 26). The EDS data show carbon in all three particles.
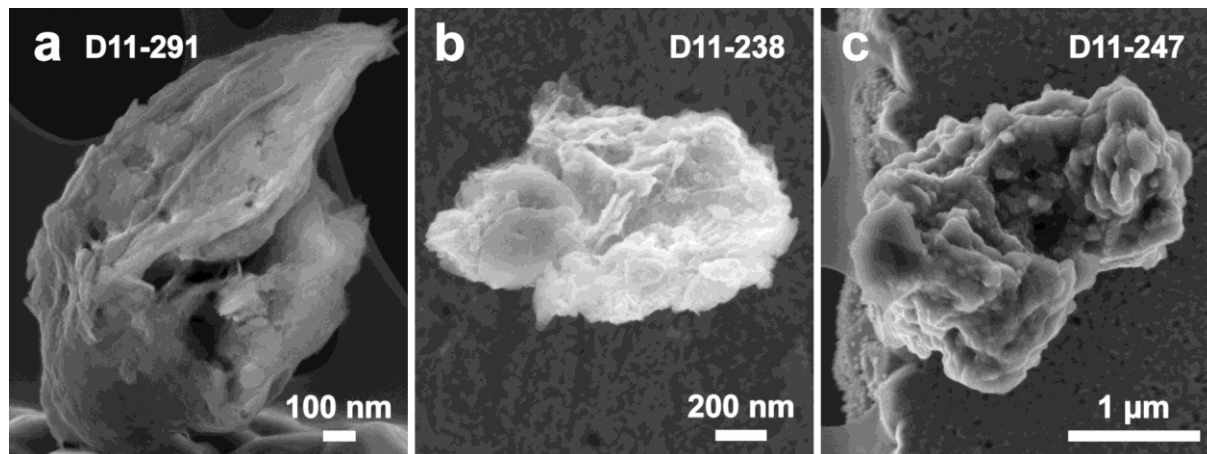
Figure 25: FE-SEM/SE images of low-Mg aluminosilica particles: (a) D11-291 has small holes and appears to be folded; (b) D11-238 is a thermally annealed particle; (c) D11-247 is a dense aggregate of (sub-)spherical grains.
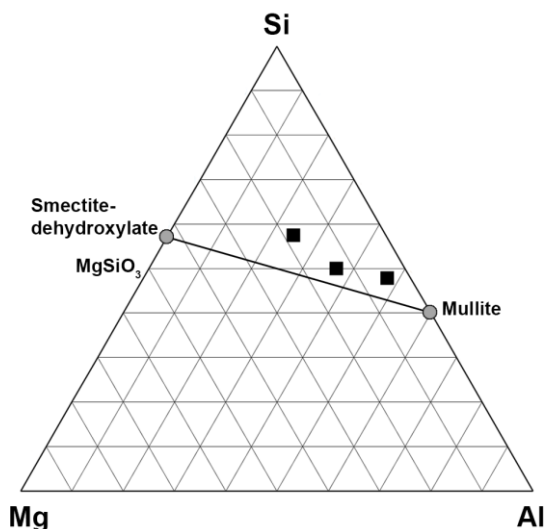
Figure 26: Si-Mg-Al (at.%) composition of these low-Mg aluminosilica grains (solid squares). The gray dots designate the mullite ($3Al_2O_3 \cdot 2SiO_2$) and smectite-dehydroxylate ($Mg_6Si_8O_{22}$) compositions.

6.1.2. Silica particles

Morphologically they present a rather diverse group (Fig. 27). In this figure they are arranged according to their morphology ranging from (1) irregularly-shaped layered particles with numerous droplets scattered across the layers, to (2) smooth platy grains that can be attached to particles (1) or forming aggregates of smooth platy grains, to (3) smooth disc-like grains, and (4) clusters of smooth silica spheres. They are mostly pure silica but some particles show a trace amount of Al (<1 at.%). All

particles have a C-O mantle (Fig. 28). From top to bottom the particles are arranged according to increased silica melting, quenching and agglomeration (Fig. 27) prior to acquiring an oxocarbon layer as there is no evidence of chemical mixing.
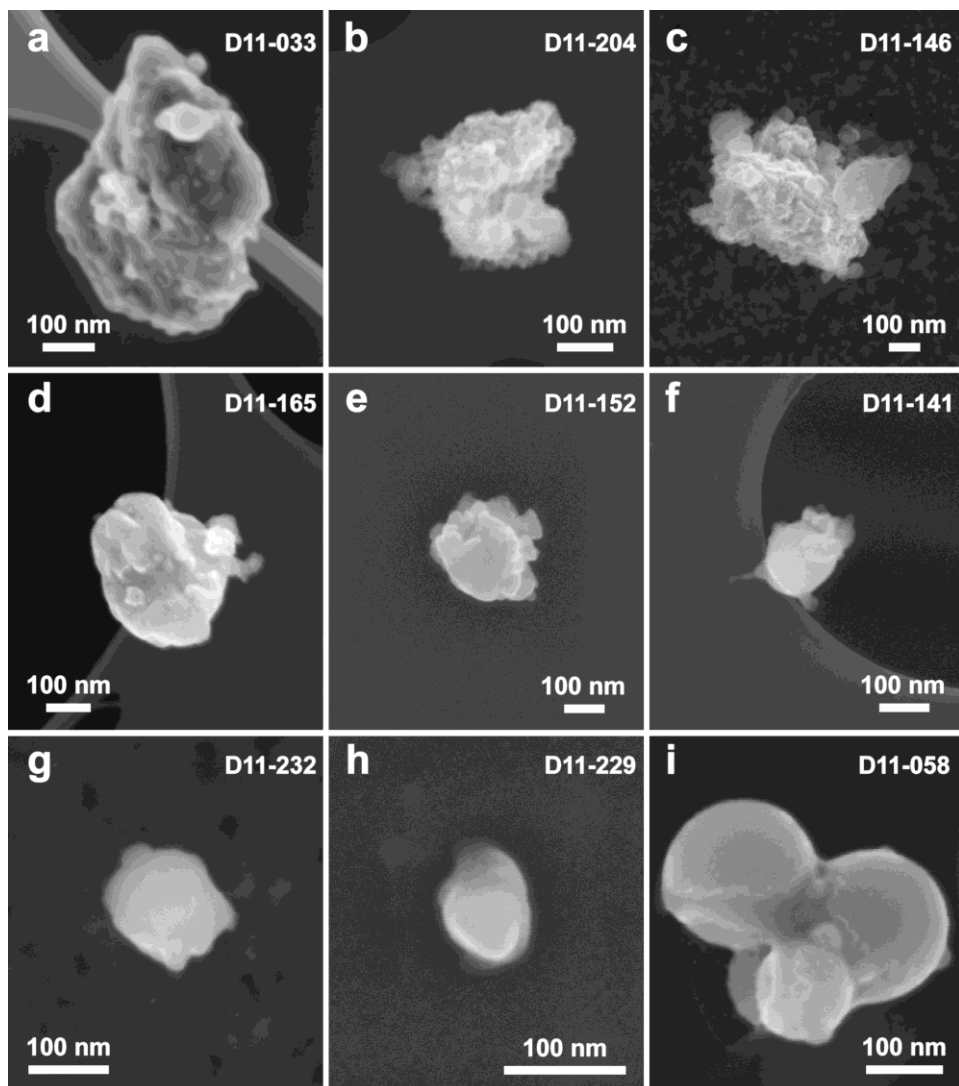
Figure 27: FE-SEM/SE images of the silica particles arranged in increasing order of melting from irregularly aggregates (top row; left) to quenched melt spheres (bottom row; right).
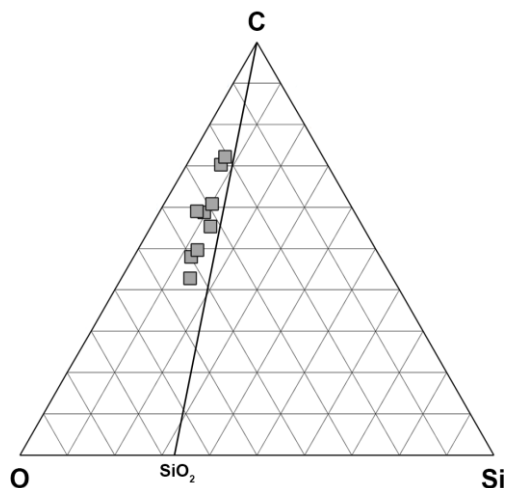
Figure 28: C-O-Si (at.%) compositions of silica particles with an oxocarbon layer.

6.1.4. Oxocarbon particles

These mostly pure C-O particles may contain trace amounts of Si (0.3 at.%) (Fig. 29), Mg (0.6 at.%) and Al (0.5 at.%) in randomly variable combinations when present; particle D11-244 contains 0.6 at.% calcium. Particle D11-244 is rather massive with only small platy grains at the surface (Fig. 30). All other particles consist of smooth layers, and all show at least a single pore (Fig. 30), which is a typical feature of thermally annealed condensate grains (Rietmeijer et al., 2002).
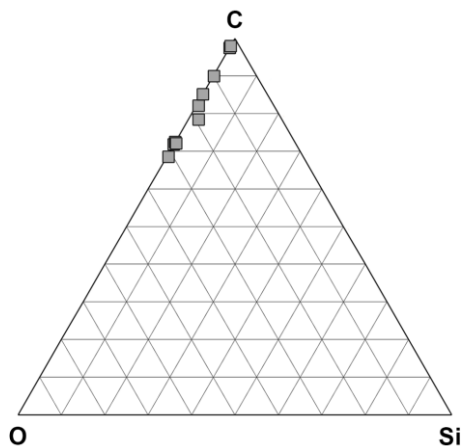
Figure 29: C-O-Si (at.%) particle compositions
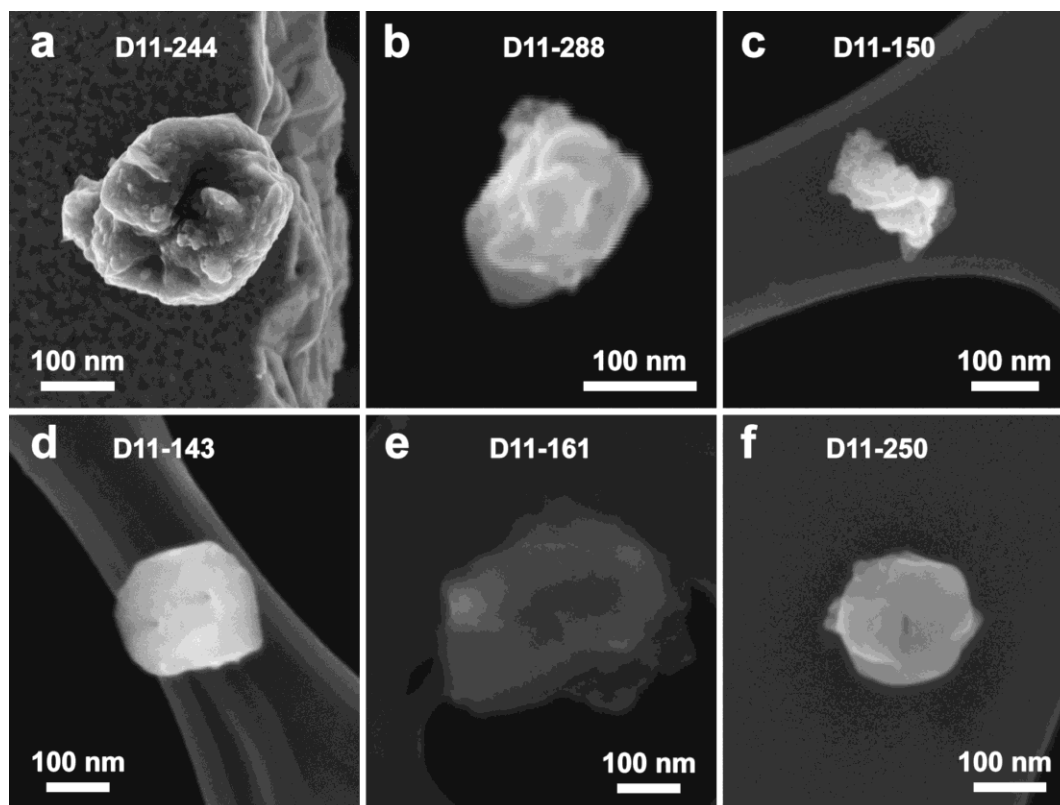
Figure 30: FE-SEM/SE images of an original oxocarbon particle (clockwise from top row; left) and thermally annealed condensed oxocarbon aggregates. Note: particle D11-244 was deposited onto the supporting grid.

6.1.5. CaO-particles

They are layered particles with a smooth surface. Tiny holes indicate that they are thermally annealed quenched melted or condensed particles (Fig. 31). Their compositions show a mixture of CaO and C-O particles; the latter with O/(O+C) = 0.3 (Fig. 32).
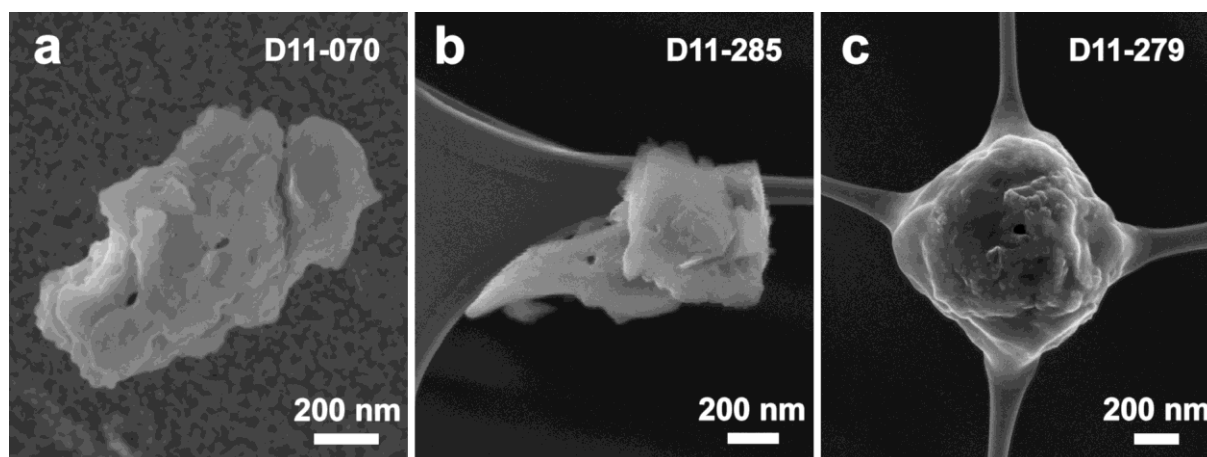
Figure 31: FE-SEM/SE images of CaO particles.
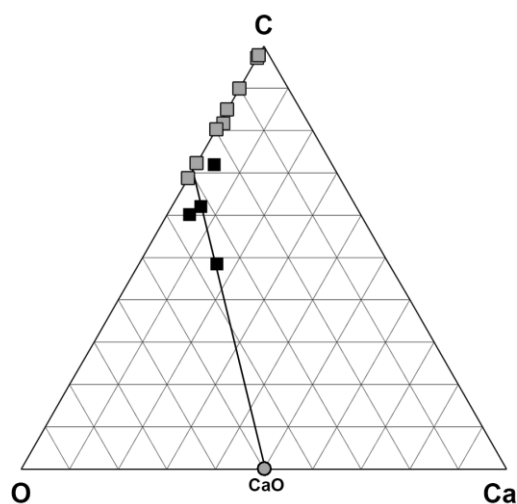
Figure 32: C-O-Ca (at.%) compositions of CaO particles (black squares) that are mixtures of C-O (gray squares) and pure CaO (gray dot).

7-DISCUSSION

The particles here presented were collected from a random volume of stratospheric air along the balloon's flight path. The particles represent independent snapshots of the stratospheric dust burdens that were determined only by the time of each flight opportunity. There are differences and similarities among the particles collected in 2008 and 2011 that need an explanation (Table 3). Both collections contain Al-oxides, C-O (oxocarbon) particles and Ca-C-O±F particles. Technically, CO and CO_2 are the simplest oxocarbons but there are many stable and metastable oxocarbons (Seitz and Imming, 1992), yet little is known of their thermal stabilities and the extent of their natural occurrences. It is known that oxocarbon particles with O/(O+C) ratios < 0.4 will condense from carbon-oxygen gas mixtures at temperatures slightly below the pure carbon melting point (Horowitz et al., 2010).

Table 3: **PARTICLES COLLECTED IN 2008 AND 2011**

D08 collection	D11 collection
Fassaite	
Plagioclase	
	SiO_2
Aluminosilica	Mg-aluminosilica
TiO2	
low-F phosphate	
	Al_2O_3

Calcite/aragonite ± Fluorine

CaO ± Fluorine	CaO ± Fluorine
Carbon	Carbon
O/(O + C) < 0.4 Oxocarbons	O/(O + C) < 0.4 Oxocarbons

The 2008 collection from the stratosphere between 37-38.5 km altitudes is dominated by Ca-carbonate particles while the 2011 collection, which was collected between 31.6-33.7 km altitudes three years later, is rich in silica particles. Is it possible that largest 2008 carbonate particles had fallen to altitudes below 37 km during this 33.5-month interval? The stratospheric residence times for most of the collected particles were probably very low given their combinations of shape, mass and size but not identical (equant vs. platy shapes) (Fig. 3). It also depends on the deposition altitudes. But, the actual stratospheric residence times of sub-micron dust is not entirely determined by gravitational settling alone. It was found that the stratospheric residence times of sub-micron dust from 1982 El Chichón volcanic eruption with a similar size range and size distribution as the DUSTER particles were still present between 34 and 36 km altitude three years after the eruption, and in fact had risen ~3 km above the maximum plume height (Testa et al., 1990; Rietmeijer, 1993). When differential settling rates as a function of grain size alone caused the observed differences and similarities it could follow that the 2008 and 2011 had a common origin.

The timing of the DUSTER 2008 and 2011 flights was determined by the availability of flight opportunities, which carried the risk that the flight paths might encounter stratospheric air laden with fine-grained volcanic ejecta. Using the on-line available the Smithsonian Institution Scientific Event Alert Network (SEAN-) bulletins, we found no volcanic activities several months prior to each flight that could have caused volcanic ash along the 2008 and 2011 flight paths. Also the very fine ash compositions of mineral and salt of the El Chichón volcanic ejecta (Rietmeijer, 1993) were very different from those of the collected particles described here. Furthermore the high DUSTER altitudes offer a measure of confidence that the collected dust particles were not from sources at the Earth surface.

We submit that the particles here described are due to fragmentation of meteoroids decelerating in the atmosphere, their sudden disintegration, incandescent dust trains and clouds (Klekociuk et al., 2005), and ultimately low-altitude persistent dust clouds. Incoming meteorite-dropping meteoroids are mostly ordinary chondrite meteorites with a small contribution from CI and CM carbonaceous meteorites. These meteorites are structurally coherent, often fragile, rocks dominated by Mg-Fe-silicates (±Al and Ca in various combinations), refractory oxide minerals and Fe(Ni)-sulfides (Brearley and Jones, 1998) but with a wide variety of individual mineral species (Rubin, 1997; Kerridge and Macdougall, 1976). The Stardust mission that collected dust in the coma of comet 81P/Wild 2 for laboratory analyses showed that the dust

particles from this ==Jupiter-family comet== is an unconsolidated collection of the same minerals and mineral clusters found in ordinary chondrite meteorites (Zolensky et al., 2008; Joswiak et al., 2009, 2012; Rotundi et al. 2014; Simon et al., 2008; Chi et al., 2009, among others). Thus, this unconsolidated dust sample is really an excellent analog for dust due to meteor fragmentation and disintegration. The collected particles presented in this paper (Table 2) are found in these meteorites and comet Wild 2. The Ca-carbonate and carbon particles suggest an affinity to fireballs caused by CI and CM carbonaceous chondrite meteorites, such as the Sutter's Mill meteorite (Jenniskens et al., 2012), and especially Ca-carbonates in the Tagish Lake meteorite (Brown et al., 2000). Also, Della Corte et al. (2013) observed that carbon in meteorites is present as organic carbons and elemental carbon forms but there is no mention of oxocarbons. This could be an analytical issue as no deliberate searches for oxocarbons were made in meteorite samples. We note that Nakamura-Messenger et al. (2006) found CHON-like organic globules in the Tagish Lake meteorite.

The observations so far put the temperatures between ~4,300^{o}C and ~430°C for 5 seconds and high cooling rates. The properties and chemical reactions of D08 and D11 particles support temperatures between ~2000°C and ~1000°C, as high as 3,700^{o}C and as low as ~650°C after 9s, followed by rapid quenching (μs) to below 1,600^{o}C (Table 4). ==The question is, "Are these conditions achieved in fireballs and bolides?"==

Table 4: **THERMAL REGIMES OF DUST PROCESSING**

Minerals/compounds	Temperatures	Sources
Surviving but thermally modified grains		
Calcite/aragonite (CaCO$_3$)	Flash-heating at 950°C; Calcite decomposition at ~650°C after 9s [D08]	Han et al., 2007; Rietmeijer et al., 2003; Della Corte et al., 2013
albite-anorthite plagioclase	1,120 to 1,550^{o}C [D08]	Ehlers, 1972
metastable aluminosilica grain	Rapidly quenched (μs) below 1,600^{o}C [D08]	Rietmeijer and Karner,1999
	Grain melting	
CaO melting	2,570^{o}C [D08]	Han et al., 2007
SiO$_2$ (silica)	570 – 1,610^{o}C [D11]	Deer et al., 1978
Fluorite (CaF$_2$)	1,350^{o}C [D08 & D11]	Okamoto, 1997
Oxocarbon; O/(O+C) = 0 - 0.4	3,650 to 3,700^{o}C [D08 & D11]	Horowitz et al., 2010
	Newly formed grains	
low-Mg aluminosilica grains; a	Mullite melting 1,500 to	Jung et al., 2001; Rietmeijer and

mullite-magnesiosilica solid solution mixture	1,850°C; Rapidly quenched (μs) deep metastable eutectic smectite dehydroxylate ($Mg_6Si_8O_{22}$) quenched <1,550°C [D11]	Karner,1999; Rietmeijer and Nuth, 2012
F-bearing $CaCO_3$ and Ca-oxide aging; $Ca(OH)_2$ formation	Room temperature	

The time-temperature conditions inside fireball clouds and incandescent dust trains (Fig. 1) are still poorly understood. As a general rule meteoric dust survival is possible up to the temperatures of the so-called "main spectrum" meteor regime of~4,300°C but this peak temperature decreases rapidly (Borovička, 1993). For example, the close to 5,000K gas temperature in a Leonid fireball had decayed to 1,200K in 2 seconds (Borovička and Jenniskens, 2000). In general, some of the relevant chemical reactions occur this so-called 'warm air plasma' due to the interactions of the impinging air molecules with the meteoroid and its vapor cloud (Jenniskens et al., 2004). The Chelyabinsk fireball was an exceptionally energetic event with only two other events of comparable energies in over a century, *viz.* the '1963 August 3 bolide' and the Tunguska impact in 1908 (Popova et al., 2014). Chelyabinsk fireball had the equivalent energy of $570 \pm 150kt$ TNT (Popova et al., 2013) which implies that physiochemical processes inside the Chelyabinsk train were at their most extreme ever witnessed before. After reaching peak brightness at 29.7 km altitude a thermal-emitting debris cloud formed that came to rest between 27 and 28 km altitude. Fragmentation started between about 50-60 km, but final catastrophic fragmentation occurred between 40 and 30 km altitude (Popova et al., 2013). Only 4 to 6 tons of surviving meteorite material reached the ground including a large > 570 kg meteorite recovered from a lake. These surviving meteorites represent 0.03-0.05% of the initial meteoroid mass. It was estimated that 76% of the initial meteoroid evaporated because of the intense radiation in the incandescent debris cloud which caused evaporation of most fragments that were further reduced to dust (Popova et al., 2013). The fate of the vapors is unknown. Most likely they condensed as nanograins and/or coatings on surviving dust. About 5 seconds after the formation of the smoke clouds in the Chelyabinsk superbolide the cloud temperatures were 700 ± 100 K. Assuming that the initial temperature in the cloud was that of dust evaporation, the resulting cooling rate was ≥240 K/s (Popova et al., 2013). Cooling rates of this magnitude would be sufficient to quench Ca-oxide melts, and cause melting carbon nanograins, some of which still surviving, forming C-O melts and/or vapors and final deposition as oxocarbon layers or condensation. In this context it is noted that Mid-infrared spectroscopy of persistent Leonid trains detected enhanced emissions of warm CH_4, CO_2, CO and H_2O (Russell et al., 2000). These species, that include the CO and CO_2 oxocarbons, may have originated from heated trace components in the ambient air or from materials that

Most likely in the Chelyabinsk event some fraction of larger dust particles probably survived while cascades of particle fragmentation would also produce dust fragments well into the micro- and nanometer ranges. In the TC_3 cloud from the Almahata Sitta meteorite entry (Jenniskens et al., 2009) the temperature had held steady at ~1000°C for at least one minute, but five minutes after the end of the luminous phase the temperature of dust that was settling in cloud was just over 725°C for one minute (Borovička and Charvát, 2009). These conditions would have sufficed to cause surface melting on micrometer-size grains and melting of smaller grains. As the conditions inside hot, dust-carrying bolide trains will favor kinetically-controlled reactions, the final solid compositions will be an *a priori* unpredictable mixture of (partial) surviving, modified and newly-formed dust particles. The similarities between the temperature-time regimes of the natural events and those indicated by the collected particles make a strong case that DUSTER collected meteoric dust particles. Bolides and fireballs will remain events with their own unique temperature-time constrains that are different from other naturally occurring catastrophic events.

There are other implications. The numerous (sub-)spherical Ca-carbonate nanograins at the surface of plagioclase particle D08-008b show that these fragments were in close proximity. Proximity of particles is also supported by the quenched-liquid and/or vapor condensed CaO and CaF_2 nanograins arranged in the typical "bunch-of-grape" morphology (Della Corte et al., 2013) alongside surviving grains. We submit that the collected dust DUSTER particles were entrained in closed-system environments during (ultra)rapid physiochemical processes in bolide/fireball events. That being said, it is noted that fluorine, which is classified as a moderately volatile lithophile element, actually has a low cosmic abundance. It is only a minor element (ppm level) in carbonaceous and undifferentiated ordinary chondrite meteorites wherein this element is found in apatite, carbonate-fluorapatite, fluorapatite (Rubin, 1997). Low-F phosphate was present in the 2008 collection (Table 3). It is reasonable then to assume that fluorine was available to the many particles in 2008, fewer in 2011, for chemical reactions constrained in a Ca-O-C-F system. The F/(F+Ca) = 0.7 bulk composition of extreme F-rich C-O-Ca particle D08-034, which is a chain-like aggregate of nanograins, closely matches pure CaF_2 (fluorite). Sub-angular layered, extreme F-rich C-O-Ca particle D08-035 that has a F/(F+Ca) = 0.35 composition. Its composition suggests a deep metastable eutectic composition that is the result of ultrafast quenching from the vapor or liquid phase. The Ca-F (at.) phase diagram has two eutectic points, one at 2 at.% and another at 60 at.% F. This particular configuration allows a DME (deep metastable eutectic) composition (Rietmeijer and Nuth, 2012, 2015) that for the D08 particles is located at F/(F+Ca) = 0.35. The other Ca-F particle compositions show some scatter but are generally consistent with this DME composition, and with CaF_2. However the Ca-F compositions of these other particles favor F/(F+Ca) ratios between 0.05 and 0.15 for a mixture of the low eutectic composition and the DME composition. It is a potential clue to chaotic conditions flip-

flopping between eutectic, *i.e*. equilibrium, and DME, *i.e*. non-equilibrium, behaviors. The Ca-F grains are recorders of ultrafast reactions in a closed-system environment of melting and evaporation of F-bearing precursors, followed by rapid cooling of chain-like CaF_2 aggregates, but also larger grains with DME compositions, and finally acquiring an oxocarbon surface layer.

8. CONCLUSIONS

The compositions, morphologies and chemical interactions among particles that were randomly collected in the upper stratosphere in 2008 and 2011 are consistent with ultra-rapid, non-equilibrium processes within a closed-system environment. These conditions require catastrophic geological processes such as volcanic eruptions and meteoroid impact cratering. It is highly unlikely that the collected dust particles have terrestrial origins, which leaves an extraterrestrial (meteoritic) origin as the only plausible origin. Specifically bolide and fireball fragmentation events and their incandescent dust trains and clouds that provide the conditions for closed-system chemical evolution. We showed that their thermal regimes match those inferred for the properties of the dust particles collected in the stratosphere in 2008 and 2011. We showed that the surviving dust particles have counterparts among the minerals in undifferentiated ordinary chondrite and in carbonaceous chondrite meteorites. To the best of our knowledge ours is the first time that extraterrestrial dust from these sources has been intercepted while falling in the Earth's stratosphere. Clearly more work, that is, more DUSTER flights, are needed to assess the full impact of dust particles from bolide and fireball events on the stratospheric dust burden and composition that are the result of non-equilibrium chemical reactions and interactions.

REFERENCES

Bigg, E.K., Kviz, Z., Thompson, W.J., 1971. Electron microscope photographs of extraterrestrial particles. Tellus 23, 247-260.

Blake, D.F., Kato, K., 1995. Latitudinal distribution of black carbon in the upper troposphere and lower stratosphere. J. Geophys. Res. 100(D4), 7195-7202.

Borovička, J., 1993. A fireball spectrum analysis. Astron. Astrophys. 279, 627-635.

Borovička, J., Jenniskens, P., 2000. Time resolved spectroscopy of a Leonid fireball afterglow. Earth Moon Planets 82-83, 399-428.

Borovička, J., Kalenda, P., 2003. The Morávka meteorite fall: 4. Meteoroid dynamics and fragmentation in the atmosphere. Meteorit. Planet. Sci. 38, 1023-1043.

Borovička, J., Charvát, Z., 2009. Meteosat observation of the atmospheric entry of 2008 TC$_3$ over Sudan and the associated dust cloud. Astrophys Astron. 507, 1015-1022.

Borovička, J., Weber, H.W., Jopek, T., Jakeš, P., Randa, Z., Brown, P.G., Revelle, D.O., Kalenda, P., Schultz, I., Kucera, J., Haloda, J., Týcová, P., Frýda, J., Brandstätter, F., 2003. The Moravka meteorite fall: 3. Meteoroid initial size, history, structure and composition. Meteorit. Planet. Sci. 38, 1005-1021.

Borovička, J., Spurný, P., Brown, P., Wiegert, O., Kalenda, P., Clark, D., Shrbený, L., 2013.The trajectory, structure and origin of the Chelyabinsk asteroidal impactor. Nature 503, 235-237.

Brearley, A.J., Jones R.H., 1998. Chondritic Meteorites. In: Papike, J.J. (Ed.), Planetary Materials, Reviews in Mineralogy, 36, Mineralogical Society of America, Chantilly, pp. 3-1-3-398.

Brown, P.G., Hildebrand, A.R., Zolensky, M.E., Grady, M., Clayton, R.N., Mayeda, T.K., Tagliaferri, E., Spalding, R., MacRae, N.D., Hoffman, E.L., Mittlefehldt, D.W., Wacker, J.F., Bird, J.A., Campbell, M.D., Carpenter, R., Gingerich, H., Glatiotis, M., Greiner, E., Mazur, M.J., McCausland, P.J.A., Plotkin, H., Mazur, T.R., 2000. The fall, recovery, orbit, and composition of the Tagish Lake meteorites: A new type of carbonaceous chondrite. Science 290, 320-325.

Ceplecha, Z., Spalding, R.E., Jacobs, C., ReVelle, D.O., Tagliaferri, E., Brown, P., 1999. Superbolides. Meteoroids 1998, Astron. Inst. Slovak Acad. Sci., Bratislava, 37-54.

Ciucci, A., 2011. Stratospheric dust collection by DUSTER (Dust in the Upper Stratosphere Tracking Experiment and Retrieval), a balloon-borne instrument and laboratory analyses of collected dust. PhD thesis, Department of Aerospace Engineering, Universita degli Studi di Napoli Federico II, Naples, Italy.

Cziczo, D.J., Thomson, D.S., Murphy, D.M., 2001. Ablation, flux, and atmospheric implications of meteors inferred from stratospheric aerosol. Science 291, 1772-1775.

Chi, M., Ishii, H.A., Simon, S.B., Bradley, J.P., Dai, Z., Joswiak, D., Browning, N.D., Matrajt, G., 2009. The origin of refractory minerals in comet 81P/Wild 2. Geochim. Cosmochim. Acta 73, 7150-7161.

Deer, W.A., Howie, R.A., Zussman, J., 1978. An introduction to the rock forming minerals. Longman Group Ltd, 528p.

De Angelis, S., Della Corte, V., Baratta, G.A., Rietmeijer, F.J.M., Brunetto, R., Palumbo, P., Ciucci, A., Rotundi , A., 2011. Raman micro-spectroscopy performed on extraterrestrial particles. Spectroscopy Lett. 44, 549-553.

Della Corte, V., Palumbo, P., Rotundi, A., De Angelis, S., Rietmeijer, F.J.M., Bussoletti, E, Ciucci, A., Ferrari, M., Galluzzi, V., Zona, E., 2012. In situ collection of refractory dust in the upper stratosphere: The DUSTER Facility. Space Sci. Revs. 169, 159-180; DOI 10.1007/s11214-012-9918-9

Della Corte, V., Rietmeijer, F.J.M., Rotundi, A., Ferrari, M., Palumbo, P., 2013. Meteoric CaO and carbon smoke particles collected in the upper stratosphere from an unanticipated source. Tellus B 2013, 65, 20174, http://dx.doi.org/10.3402/tellusb.v65i0.20174

Della Corte, V, Rietmeijer, F.J.M., Rotundi, A. Ferrari, M., 2014. Introducing a new stratospheric dust collecting system with potential use for upper atmospheric microbiology investigations. Astrobiology 14; 694-705; doi:10.1089/ast.2014.1167

Ehlers E.G., 1972. The interpretation of geological phase diagrams. W.H. Freeman and Company, San Francisco, 280p.

Han, R., Shimamoto, T., Hirosi, T., Ree, J-H., Ando, J-I., 2007. Ultralow friction of carbonate faults caused by thermal decomposition. Science 316, 878-881.

Hervig, M.E., Deaver, L.E., Bardeen, C.G., Russell, III, J.M., Bailey, S.M., Gordley, L.L., 2012. The content and composition of meteoric smoke in mesospheric ice particles from SOFIE observations. JAS-TP. 84/85, 1-6.

Hervig, M.E., Gordley, L.L., Deaver, L.E., Siskind, D.E., Stevens, M.H., Russell, III, J.M., Bailey, S.M., Megner, L, Bardeen, C.G., 2009. First satellite observations of meteoric smoke in the middle atmosphere. Geophys. Res. Lett. 36, L18805; doi:10.1029/2009GL039737

Horowitz, C.J., Schneider, A.S., Berry, D.K., 2010. Crystallization of carbon-oxygen mixtures in White Dwarf stars. Phys. Rev. Lett. 104, 231101(4)

Janches, D., Dyrud, L.P., Broadley, S.L., Plane, J.M.C., 2009. First Observation of micrometeoroid differential ablation in the atmosphere. Geophys. Res. Lett. 36, L06101, 1-5.

Jenniskens, P., Laux, C.O., Wilson, M.A., Schaller, E.L., 2004. The mass and speed dependence of meteor air plasma temperatures. Astrobiology 4, 81-94.

Jenniskens, P., 2013. Recent documented meteorite falls, a review of meteorite – asteroid links. In Meteoroids 2013, Proceedings of the Astronomical Conference, held at A.M. University, Poznań, Poland, Aug. 26-30, 2013, eds. Jopek, T.J., Rietmeijer, F.J.M., Watanabe, J., Williams, I.P., Adam Mickiewicz University Press in Poznań, 57–68 (available online).

Jenniskens, P, Shaddad, M.H., Numan, D., Elsir, S., Kudoda, A.M., Zolensky, M.E., Le, L, Robinson, G.A., Friedrich, J.M., Rumble, D., Steele, A., Chesley, S.R., Fitzsimmons, A., Duddy, S., Hsieh, H.H., Ramsay, G., Brown, P.G., Edwards, W.N., Tagliaferri, E., Boslough, M.B., Spalding, R.E., Dantowitz, R., Kozubal, M., Pravec, P., Borovicka, J., Charvat, Z., Vaubaillon, J., Kuipe,r J., Albers, J., Bishop, J.L., Mancinelli, R..L, Sandford, S.A., Milam, S.N., Nuevo, M., Worden, S.P., 2009. The impact and recovery of asteroid 2008 TC$_3$. Nature 458, 485-488.

Jenniskens, P., Fries, M.D., Yin, Q-Z., Zolensky, M., Krot, A.N., Sandford, S.A., Sears, D., Beauford, R., Ebel, D.S., Friedrich, J.M.,Nagashima, K., Wimpenny, J., Yamakawa, A., Nishiizumi, K., Hamajima, Y., Caffee, M.W., Welten, K.C., Laubenstein, M., Davis, A.M., Simon, S.B., Heck, Ph. R., Young, E.D., Kohl, I.E., Thiemens, M.H., Nunn, M.H., Mikouchi, T., Hagiya, K., Ohsumi, K., Cahill, T.A., Lawton, J.A., Barnes, D., Steele, A., Rochette, P., Verosub, K.L., Gattacceca, J., Cooper, G., Glavin, D.P., Burton, A.S., Dworkin, J.P., Elsila, J.E., Pizzarello, S., Ogliore, R., Schmitt-Kopplin, Ph., Harir, M., Hertkorn, N., Verchovsky, A., Grady, M., Nagao, K., Okazaki, R., Takechi, H., Hiroi, T., Smith, K., Silber, E.A., Brown, P.G., Albers, J., Klotz, D., Hankey, M., Matson, R., Fries, J.A., Walker, R.J., Puchtel, I., Lee, C-T A., Erdman, M.E., Eppich, G.R., Roeske, S., Gabelica, Z.,Lerche, M., Nuevo, M., Girten, B., Worden S.P., (the Sutter's Mill Meteorite Consortium), 2012. Radar-enabled recovery of the Sutter's Mill meteorite, a carbonaceous chondrite regolith breccia. Science 338, 1583-1587.

Jenniskens, P., Rubin, A.E., Yin, Q-Z., Sears, D.W.G., Sandford, S.A., Zolensky, M.E., Krot, A.N., Blair, L., Kane, D., Utas, J., Verish, R., Friedrich, J.M., Wimpenny, J., Eppich, G.R., Ziegler, K., Verosub, K.L., Rowland, D.J., Albers, J., Gural, P.S., Grigsby, B., Fries, M.D., Matson, R., Johnston, M., Silber, E., Brown, P., Yamakawa, A., Sanborn, M.E., Laubenstein, M., Welten, K.C., Nishiizumi, K., Meier, M.M.M., Busemann, H., Clay, P., Caffee, M.W., Schmitt-Kopplin, P., Hertkorn, N., Glavin, D.P., Callahan, M.P., Dworkin, J.P., Wu, Q., Zare, R.N., Grady, M., Verchovsky, S., Emel'Yanenko, V., Naroenkov, S., Clark, D.L., Girten, B., Worden, P.S., (The Novato Meteorite Consortium), 2014. Fall, recovery, and characterization of the Novato L6 chondrite breccia. Meteorit. Planet. Sci. 49, 1388-1425.

Jessberger, E.K., Bohsung, J., Chakaveh, S., Traxel, K., 1992. The volatile element enrichment of chondritic interplanetary dust particles. Earth Planet. Sci. Lett. 112, 91-99.

Joswiak, D.J., Brownlee, D.E., Matrajt, G., Westphal, A.J., Snead, C.J., 2009. Kosmochloric Ca-rich pyroxenes and FeO-rich olivines (Kool grains) and associated phases in Stardust tracks and chondritic porous interplanetary dust particles: Possible precursors to FeO-rich type II chondrules in ordinary chondrites. Meteorit. Planet. Sci. 44, 1561-1588.

Joswiak, D.J., Brownlee, D.E., Matrajt, G., Westphal, A.J., Snead C.J., Gainsforth, Z., 2012. Comprehensive examination of large mineral and rock fragments in Stardust tracks: Mineralogy, analogous extraterrestrial materials, and source regions. Meteorit. Planet. Sci. 47, 471-524.

Jung, J.S., Park, H.C., Stevens, R., 2001. Mullite ceramics derived from coal fly ash. J. Mat. Sci. Lett. 20, 1089-1091.

Kerridge, J.F., Macdougall, J.D., 1976. Mafic minerals in the Orgueil carbonaceous meteorite. Earth Planet. Sci. Lett. 29, 341-348.

Klekociuk, A.R., Brown, P.G., Pack, D.E, DeRevelle, D.O., Edwards, W.N., Spalding, R.E., Tagliaferri, E., Yoo, B.B., Zagari, J., 2005. Meteoritic dust from the atmospheric disintegration of a large meteoroid. Nature 436, 1132-1135.

Millera, S.D., Straka, III, W.C., Bachmeier, S.A., Schmit, T.J., Partaina , Ph.T., Noh, Y-J., 2013. Earth-viewing satellite perspectives on the Chelyabinsk meteor event. Proc. Natl. Acad. Sci. 110, 18092-18097, www.pnas.org/cgi/doi/10.1073/pnas.1307965110

Murphy, D.M., Thomson, D.S., Mahonay, M.J., 1998. In situ measurements of organics, meteoritic material, mercury, and other elements in aerosols at 5 to 19 kilometers. Science 282, 1664-1669.

Nakamura-Messenger, K., Messenger, S., Keller, L.P., Clemett, S.J., Zolensky, M.E., 2006. Organic globules in the Tagish Lake meteorite: Remnants of the protosolar disk. Science 314, 1439-1442.

Neely, III, R.R., English, J.M., Toon, O.B., Solomon, S., Mills, M., Thayer, J.P., 2011. Implications of extinction due to meteoritic smoke in the upper stratosphere. Geophys. Res. Lett 38, L24808, DOI:10.1029/2011GL049865

McNeil, W.J., Lai, S.T., Murad, E., 1998. Differential ablation of cosmic dust and implications for the relative abundances of atmospheric metals. J. Geophys. Res. 103, 10,899-10,911.

Murad, E., Williams, I.P., (Eds.), 2002. Meteors in the Earth's Atmosphere. Cambridge University Press, Cambridge, United Kingdom.

Nuth, III, J.A., Hallenbeck, S.L., Rietmeijer, F.J.M., 2000. Laboratory studies of silicate smokes: Analog studies of circumstellar materials. J. Geophys. Res. 105, 10,387-10,396.

Okamoto, H., 1997. Ca-F (Calcium-Fluorine). J. Phase Equilibria 18(4), 401.

Plane, J.M.C., 2003. Atmospheric chemistry of meteoric metals. Chem. Rev. 103, 4963-4984.

Popova, O., Jenniskens, P., Shuvalov, V., Emel'yanenko,V., Rybnov, Y., Kharlamov, V., Kartashova, A., Biryukov, E., Khaibrakhmanov, S., Glazachev, D., Trubetskaya, I., 2014. Chelyabinsk meteoroid entry and airburst damage. In Meteoroids 2013, Proceedings of the Astronomical Conference, held at A.M.University, Poznán, Poland, Aug. 26-30, 2013, eds, Jopek ,T.J., Rietmeijer, F.J.M., Watanabe, J., Williams, I.P., Adam Mickiewicz University Press in Poznán, pp 3-9 (available online)

Popova, O.P., Jenniskens, P., Emel'yanenko, V., Kartashova, A., Biryukov, E., Khaibrakhmanov, S., Shuvalov, V., Rybnov, Y., Dudorov, A., Grokhovsky, V.I., Badyukov, D.D., Yin, Q-Z., Gural, P.S., Albers, J., Granvik, M., Evers, L.G., Kuiper, J, Kharlamov, V., Solovyov, A., Rusakov, Y.S., Korotkiy, S., Serdyuk, I., Korochantsev, A.V., Larionov, M.Y., Glazachev, D., Mayer, A.E., Gisler, G., Gladkovsky, S.V., Wimpenny, J., Sanborn, M.E., Yamakawa, A., Verosub, K.L., Rowland, D.J., Roeske, S., Botto, N.W., Friedrich, J.M., Zolensky, M.E., Le, L., Ross, D., Ziegler, K., Nakamura, T., Ahn, I., Lee, J.L., Zhou, Q., Li, X-H., Li, Q-L., Liu, Y., Tang, G-Q., Hiroi, T., Sears, D., Weinstein, I.A., Vokhmintsev, A.S., Ishchenko, A.V., Schmitt-Kopplin, P., Hertkorn, N., Nagao, K., Haba, M.K., Komatsu, M., Mikouchi, T., (the Chelyabinsk Airburst Consortium), 2013. Chelyabinsk Airburst, Damage Assessment, Meteorite Recovery, and Characterization. Science 342, 1069-1073.

Renard, J.B., Brogniez, C., Berthet, G., Bourgeois, Q., Gaubicher, B., Chartier, M., Balois J.Y., Verwaerde, C., Auriol, F., Francois, Ph., Daugeron, D., Engrand, C., 2008. Vertical distribution of the different types of aerosols in the stratosphere: detection of solid particles and analysis of their spatial variability. J. Geophys. Res. 113, D21303. DOI: 10.1029/2008JD010150.

Rietmeijer, F.J.M., 1993. Volcanic dust in the stratosphere between 34 and 36 km altitude during May, 1985. J. Volc. Geothermal Res. 55, 69-83.

Rietmeijer, F.J.M., 1995. Post-entry and volcanic contaminant abundances of zinc, copper, selenium, germanium and gallium in stratospheric micrometeorites. Meteoritics 30, 33-41.

Rietmeijer, F.J.M., 2002. Collected extraterrestrial materials: Interplanetary dust particles, micrometeorites, meteorites and meteoric dust. In Meteors in the Earth's Atmosphere (Murad E., Williams, I.P., (eds.), 215-245, Cambridge University Press.

Rietmeijer, F.J.M., Karner, J.M., 1999. Metastable eutectic gas to solid condensation in the Al_2O_3–SiO_2 system. J. Chem. Phys. 110, 4554-4558.

Rietmeijer, F.J.M., Mackinnon, I.D.R., 1990. Titanium oxide Magnéli phases in four chondritic interplanetary dust particles. Proc. 20th Lunar Planet. Sci. Conf., Lunar and Planetary Institute, Houston, 323-333.

Rietmeijer, F.J.M., Nuth, III, J.A., 2011. Deep metastable eutectic nanometer-scale particles in the MgO-Al_2O_3-SiO_2 system. J. Nanoparticle Res. 13, 3149-3156.

Rietmeijer, F.J.M., Nuth, III, J.A., 2012. Nanoparticles that are out of this world. In, Nature's Nanostructures, Barnard, A.S, Guo H., (eds), 329-360, Pan Stanford Publishing Pte Ltd, Singapore.

Rietmeijer, F.J.M., Nuth, III, J.A., 2015. Gas-phase condensation experiments of magnesium iron silicates. In, Laboratory Modern Astrochemistry, From molecules through nanoparticles to grains, Schlemmer, S., Giessen, T., Mutschke, H.,Jäger, C., (eds), Wiley-VCH Verlag GmbH & Co. KGaA, 455-466.

Rietmeijer, F.J.M., Schultz, P.H., Bunch, T.E., 2003. Carbon calabashes in a shock-produced carbon melt. Chem. Phys. Lett. 374, 464-470.

Rietmeijer, F.J.M., Hallenbeck, S.L., Nuth, III, J.A., Karner, J.M., 2002. Amorphous magnesiosilicate smokes annealed in vacuum: The evolution of magnesium silicates in circumstellar and cometary dust. Icarus 156, 269-286.

Rietmeijer, F.J.M., Pun, A., Kimura, Y., Nuth, III, J.A., 2008. A refractory Ca-SiO-H_2-O_2 vapor condensation experiment with implications for calciosilica dust transforming to silicate and carbonate minerals. Icarus 195, 493-503.

Rose, W.I., Durant, A.J., 2009. Fine ash content of explosive eruptions. J. Volc. Geothermal Res. 186, 32-39.

Rotundi, A., Rietmeijer, F.J.M., Colangeli, L., Mennella, V., Palumbo, P., Bussoletti, E., 1998. Identification of carbon forms in soot materials of astrophysical interest. Astron. Astrophys. 329, 1087-1096.

Rotundi, A., Rietmeijer, F.J.M., Ferrari, M., Della Corte, V., Baratta ,G.A., Brunetto, R., Dartois, E., Djouadi, Z., Merouane, S., Borg, J., Brucato, J.R., Le Sergeant d'Hendecourt, L., Mennella, V., Palumbo, M.E., Palumbo, P., 2014. Two refractory Wild2 terminal particles from a carrot-shaped track characterized combining MIR/FIR/Raman micro-spectroscopy and FE-SEM/EDS analyses. Meteorit. Planet. Sci. 49, 550-575; doi: 10.1111/maps.12274

Rubin, A., 1997. Mineralogy of meteorite groups. Meteorit. Planet. Sci. 32, 231-247.

Russell, R.W., Rossano, G.S., Chatelain, M.A., Lynch, D.K., Tessensohn, T.K., Abendroth, E., Kim, D., 2000. Mid-Infrared spectroscopy of persistent Leonid trains. Earth Moon Planets 82-83, 439-456.

Seitz, G., Imming, P., 1992. Oxocarbons and pseudooxocarbons. Chem. Rev. 92, 1227-1260.

Simon, S.B., Joswiak, D.J., Ishii, H.A., Bradley, J.P., Chi, M., Grossman, L., Aléon, J., Brownlee, D.E., Fallon, S., Hutcheon, I.D., Matrajt, G., McKeegan, K.D., 2008. A refractory inclusion returned by Stardust from comet 81P/Wild 2. Meteorit. Planet. Sci. 43, 1861–1877.

Testa, J.P., Stephens, J.R., Berg, W.W., Cahill, T.A., Onaka, T., Nakada, Y., Arnold, J.R., Fong, N., Sperry, P.D., 1990. Collection of microparticles at high balloon altitudes in the stratosphere. Earth Planet. Sci. Lett. 98, 287-302.

Zolensky, M.E., Nakamura, K., Gounelle, M., Mikouchi, T, Kasama, T, Tachikawa, O., Tonui, E., 2002. Mineralogy of Tagish Lake: An ungrouped type 2 carbonaceous chondrite. Meteorit. Planet. Sci. 37, 737-761.

Zolensky, M., Nakamura-Messenger, K., Sverdrup, J., Rietmeijer, F., Leroux, H., Mikouchi, T., Ohsumi, K., Simon, S., Grossman, L., Stephan, T., Weisberg, M., Velbel, M., Zega, T., Stroud, R., Tomeoka, K., Ohnishi, I., Tomioka, N., Nakamura, T., Matrajt, G., Joswiak, J., Brownlee, D., Langenhorst, F.,

Krot, A., Kearsley, A., Ishii, H., Graham, G., Dai, Z.R., Chi, M., Bradley, J., Hagiya, K., Gounelle, M., Bridges, J., 2008. Comparing Wild 2 particles to chondrites and IDPs. Meteorit. Planet. Sci. 43, 261-272.

Highlights

- We build DUSTER to collect dust between 30 and 40 km altitude in the upper stratosphere above the stratospheric aerosol layer
- DUSTER has built-in rigorous controls on particulate contamination during collection and laboratory handling
- Forty five nanometer to micrometer particles were collected and identified
- They are a mixture of silicates, Ca-carbonates and oxocarbons
- They formed rapidly between ~4,300^{o}C and ~430°C at high cooling rates in the upper stratosphere
- These meteoric dust particles formed in the immediate wake of fragmenting bolides and fireballs

Figure 1

Figure 2
Click here to download high resolution image

a

2

3

4

1

5

collector 2008

b

1

2

3

collector 2011

Duster collections size distributions
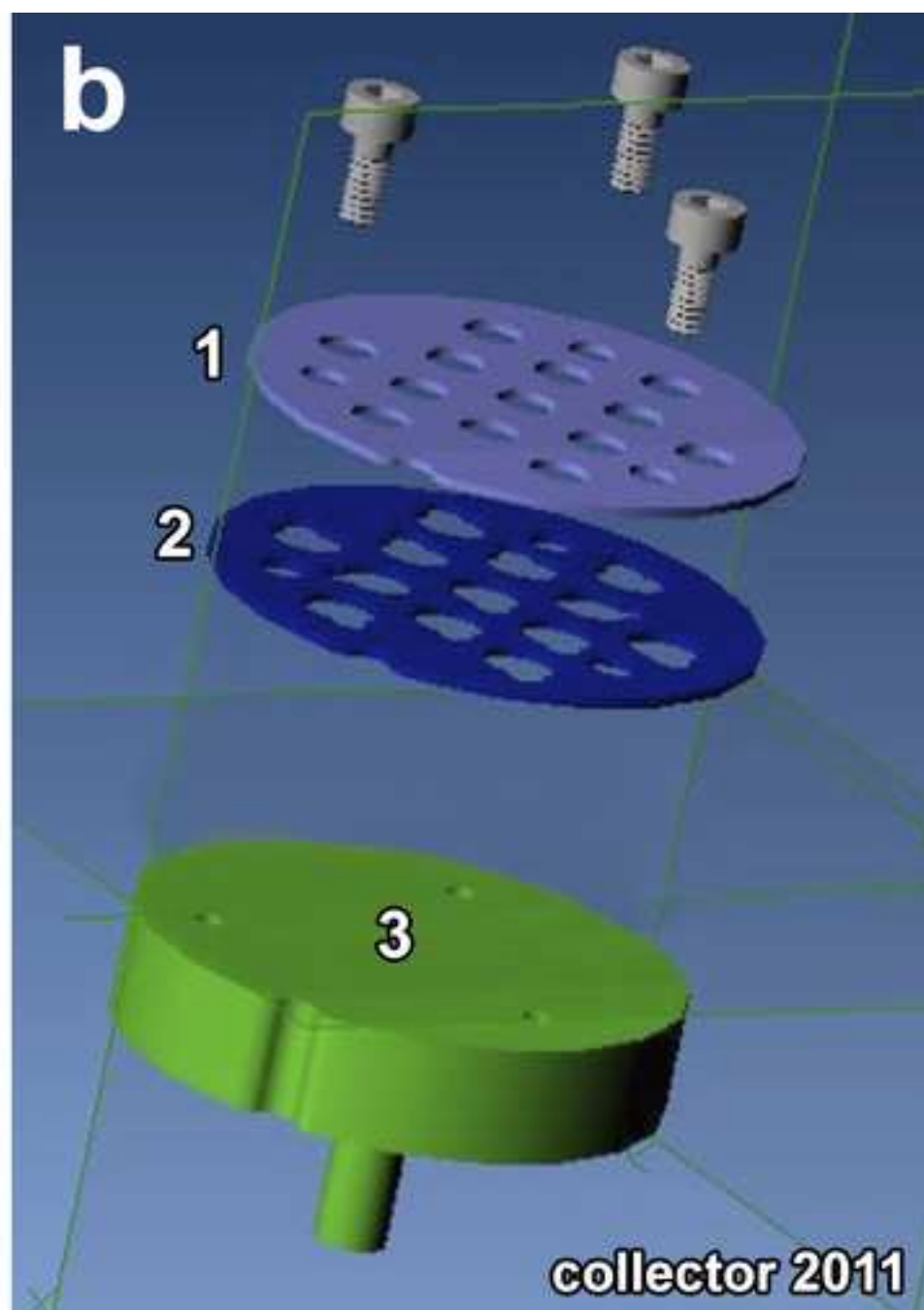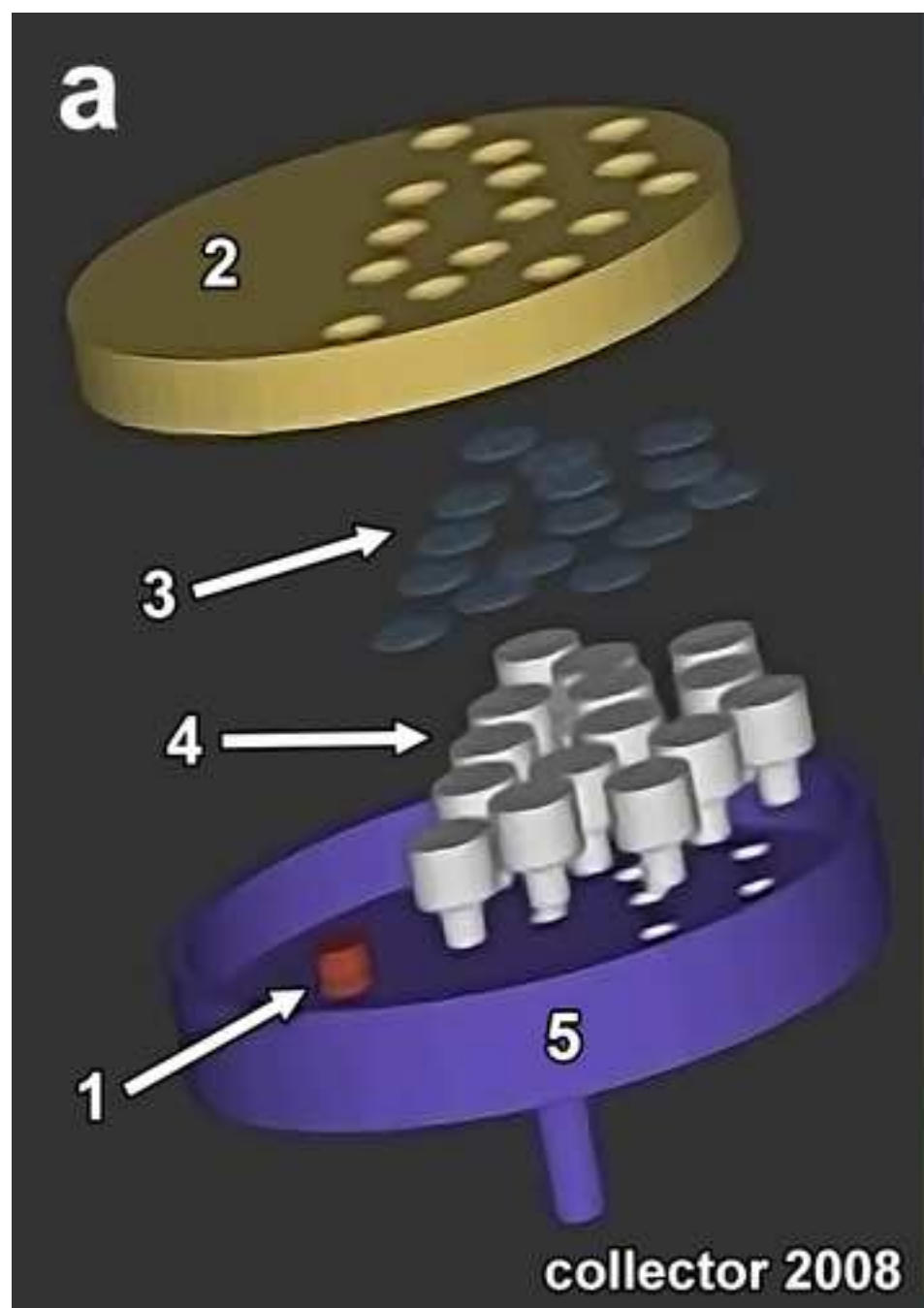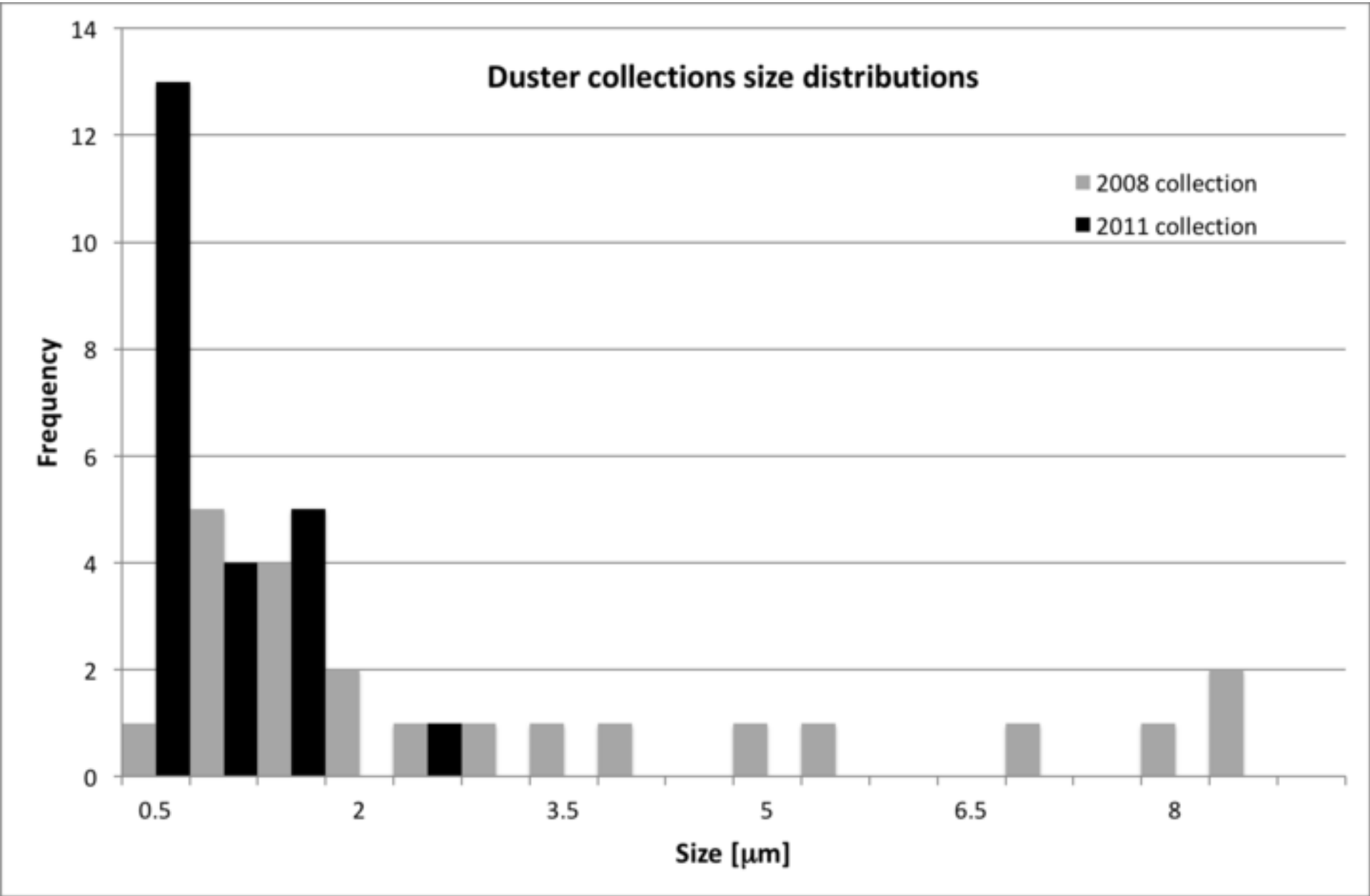
Figure 4
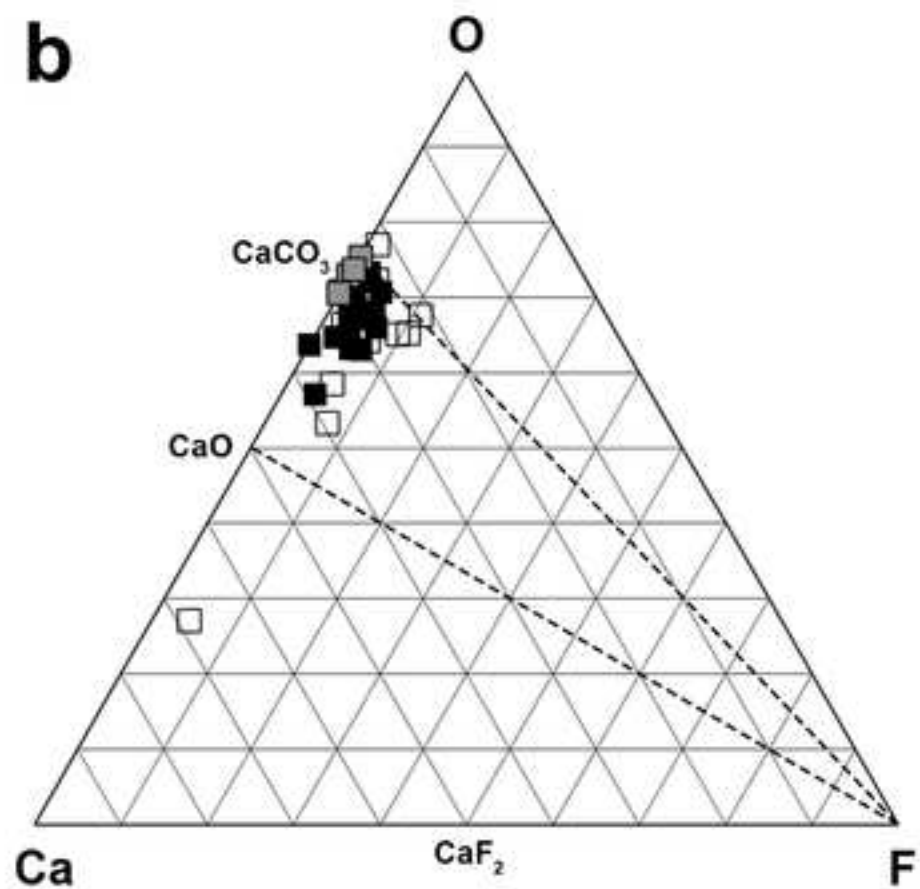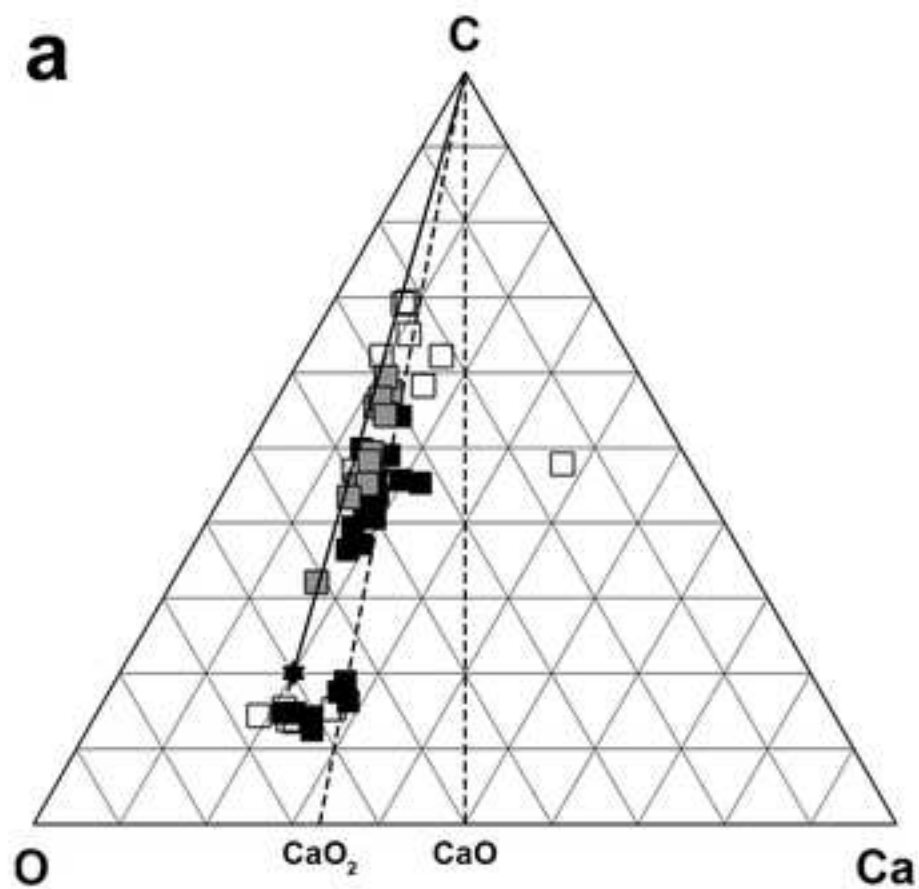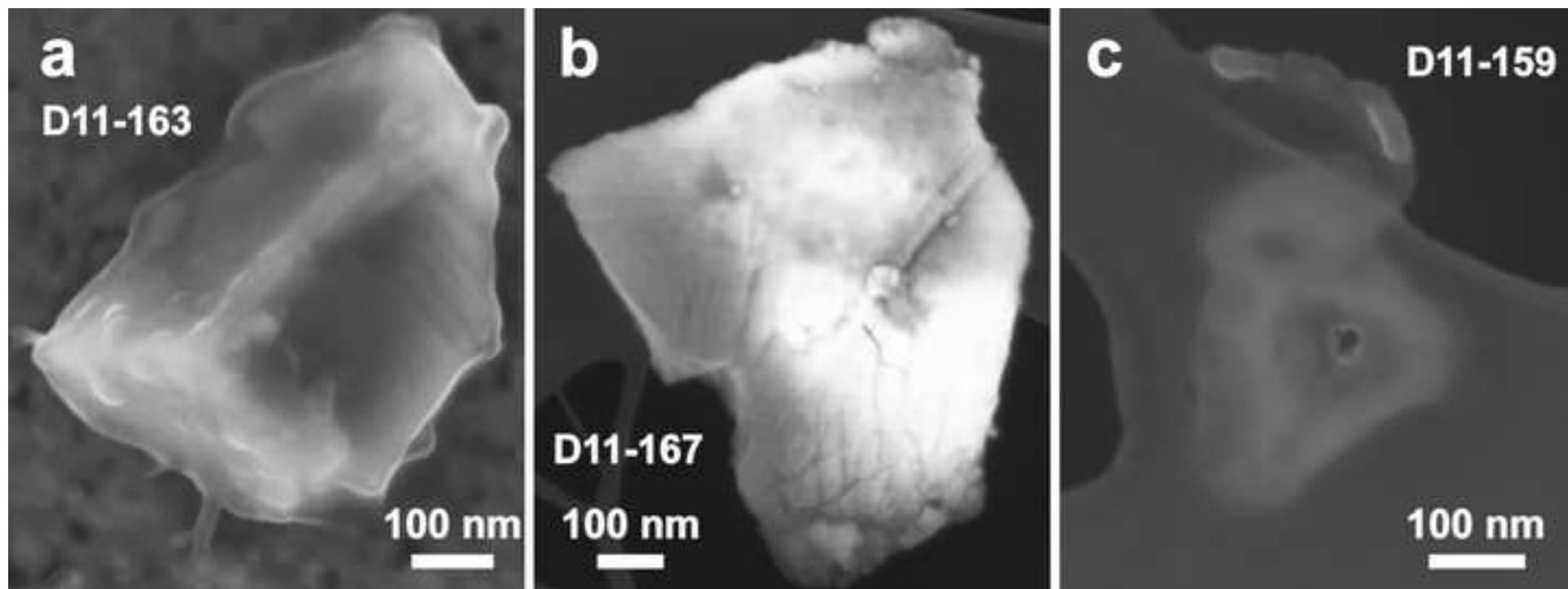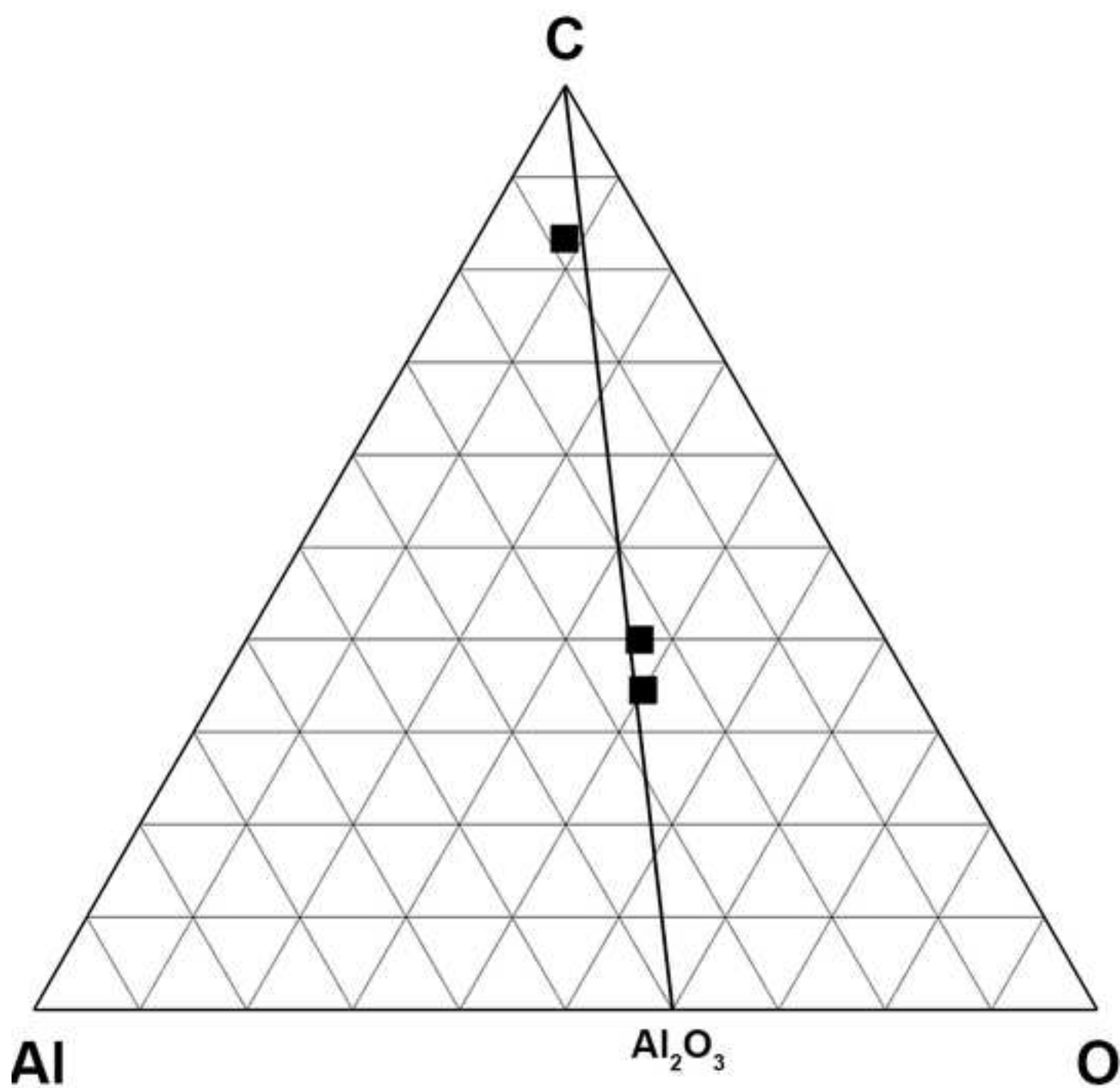**Click here to download high resolution image**
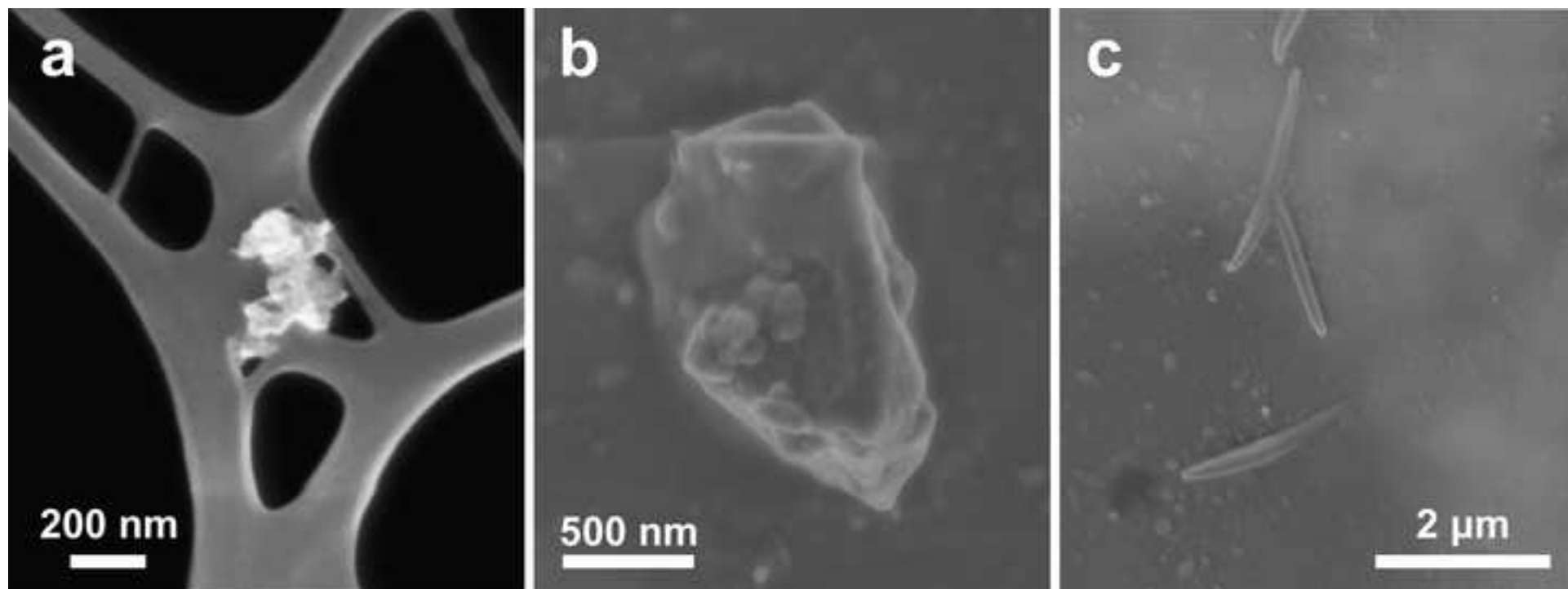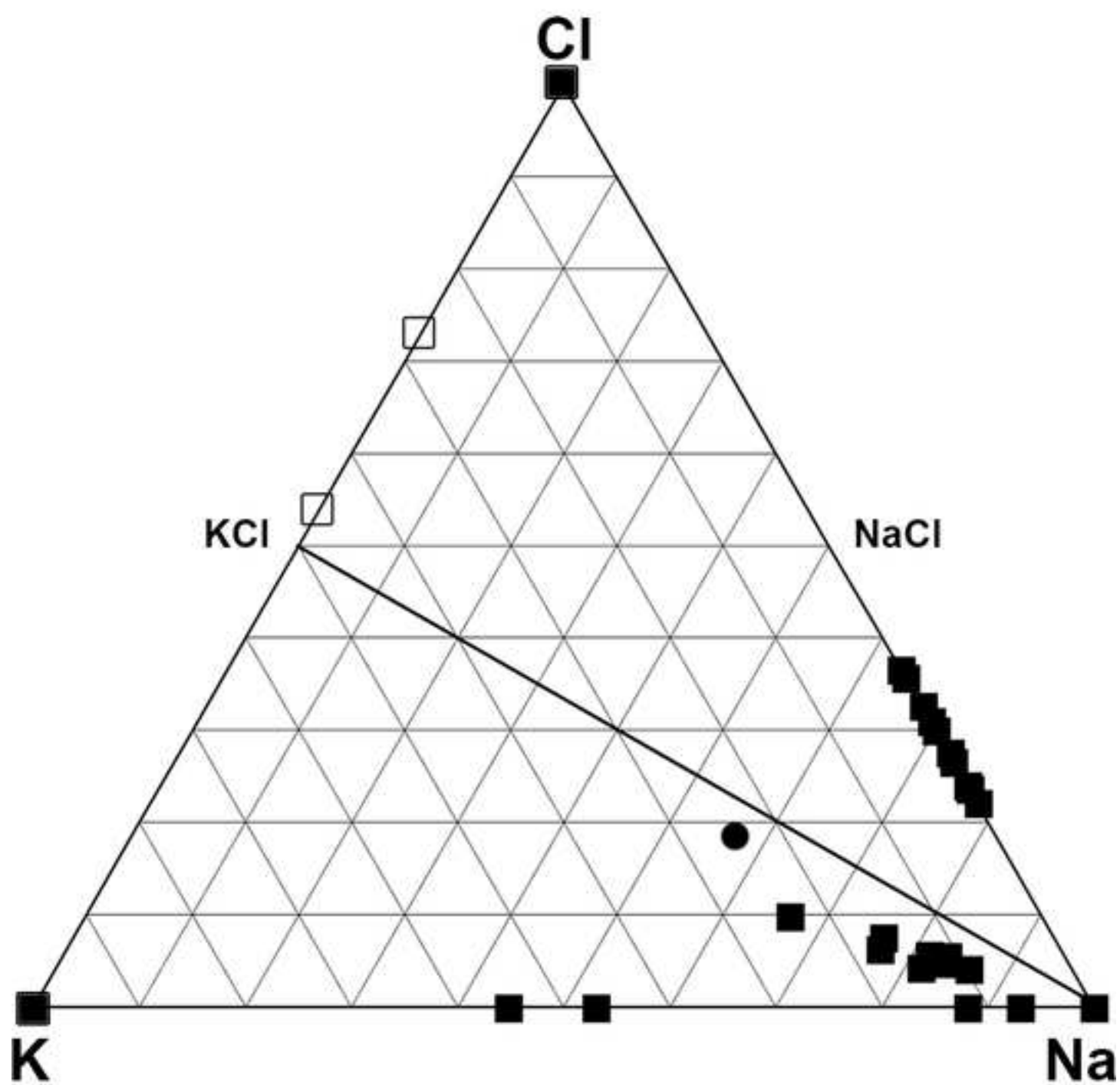
Figure 6
Click here to download high resolution image
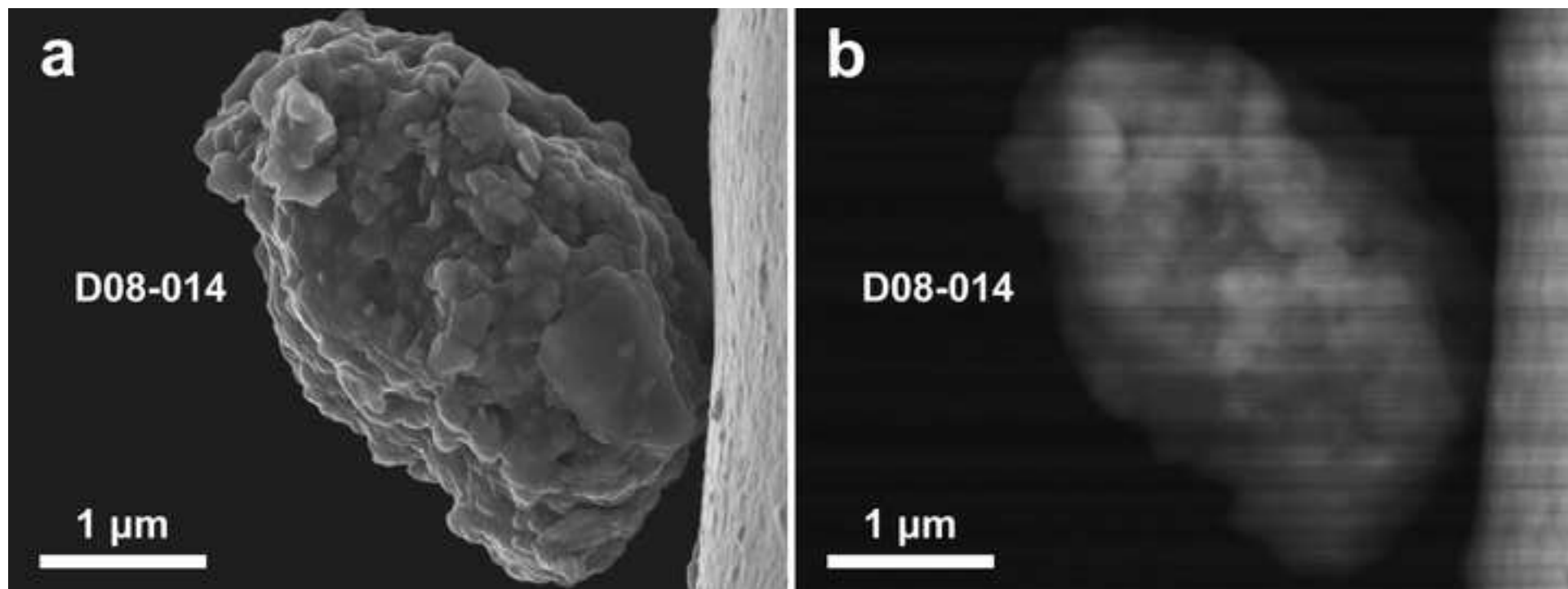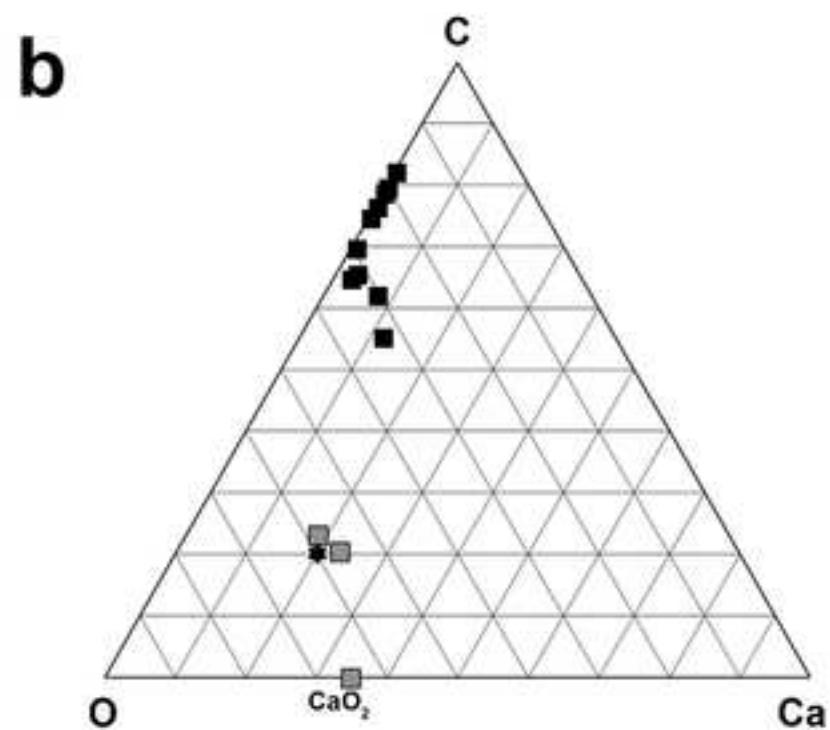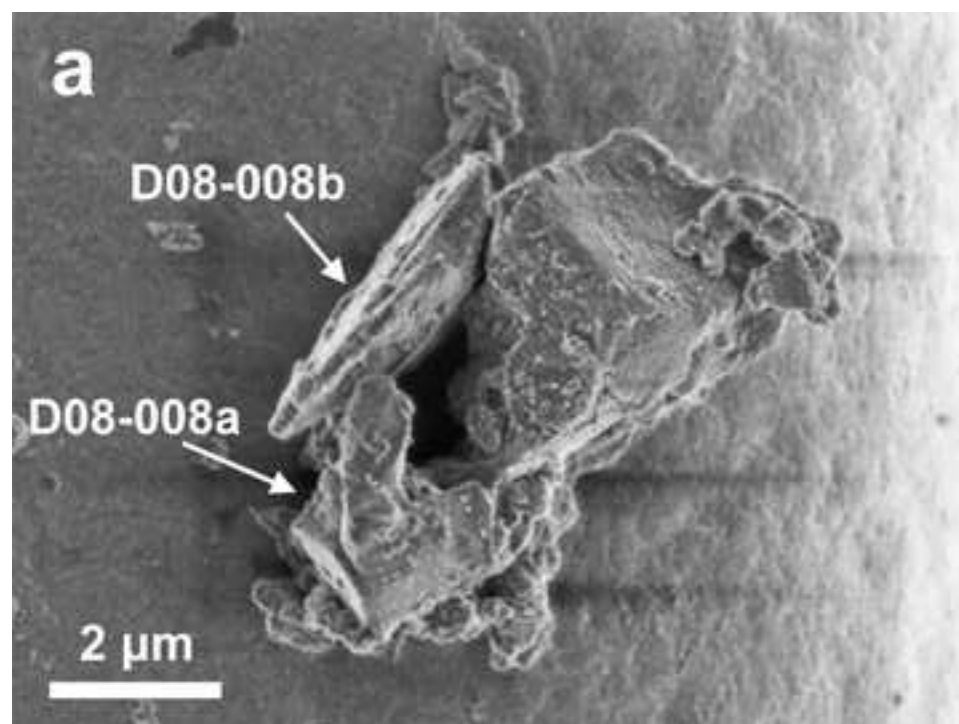
Figure 8
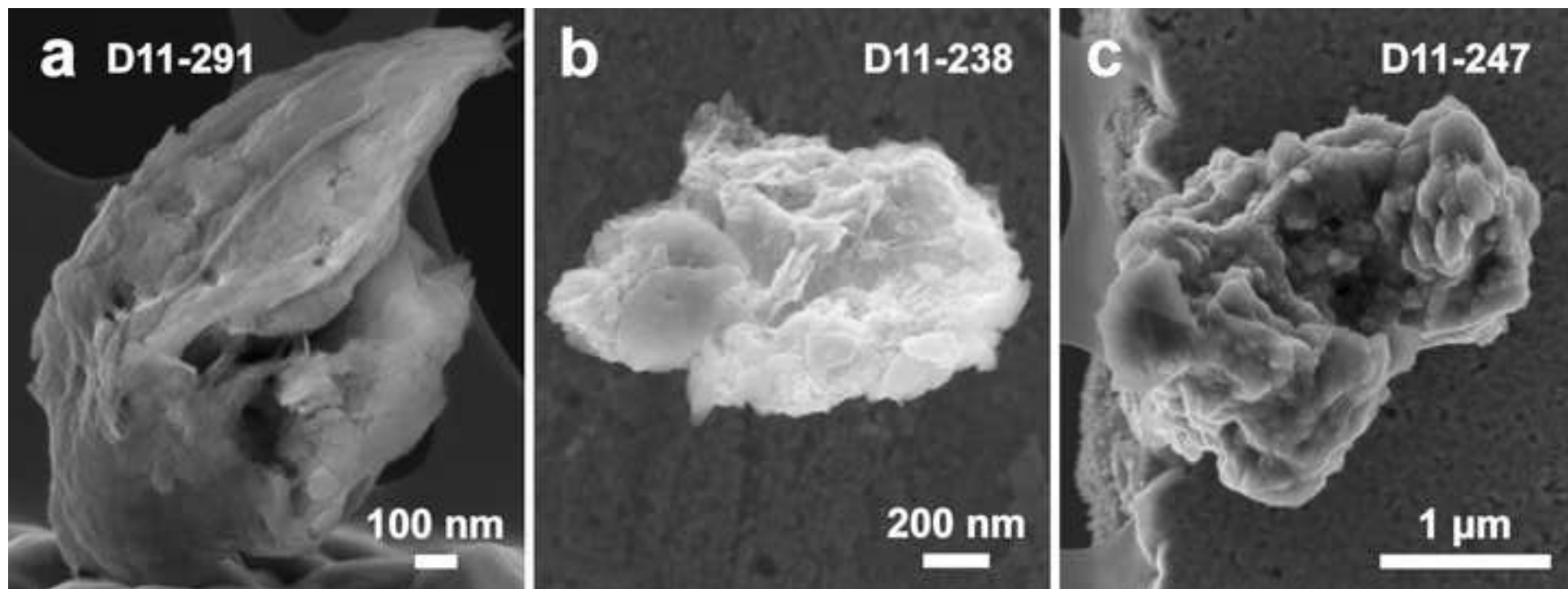[Click here to download high resolution image](#)

200 μm
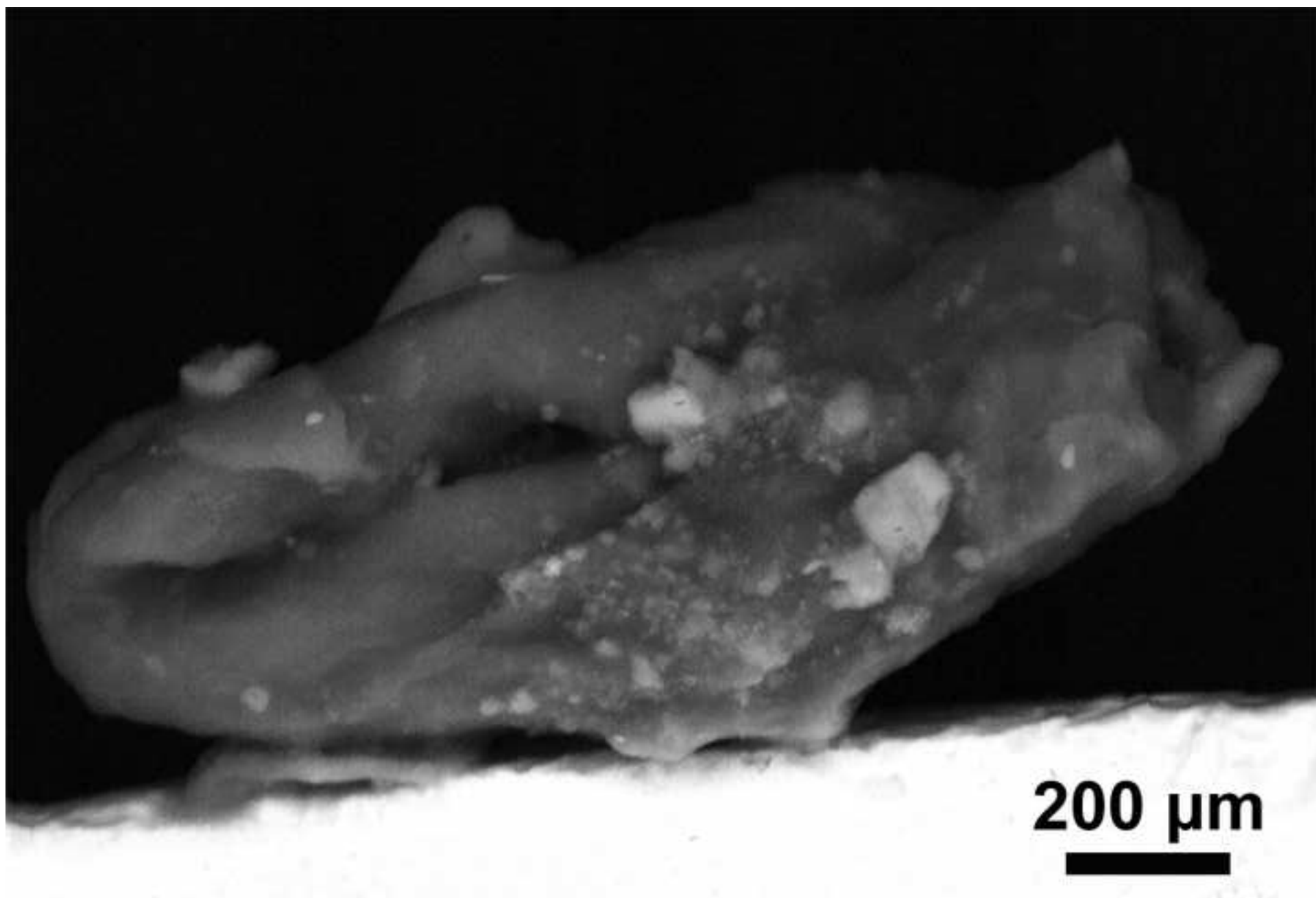
Figure 9
Click here to download high resolution image
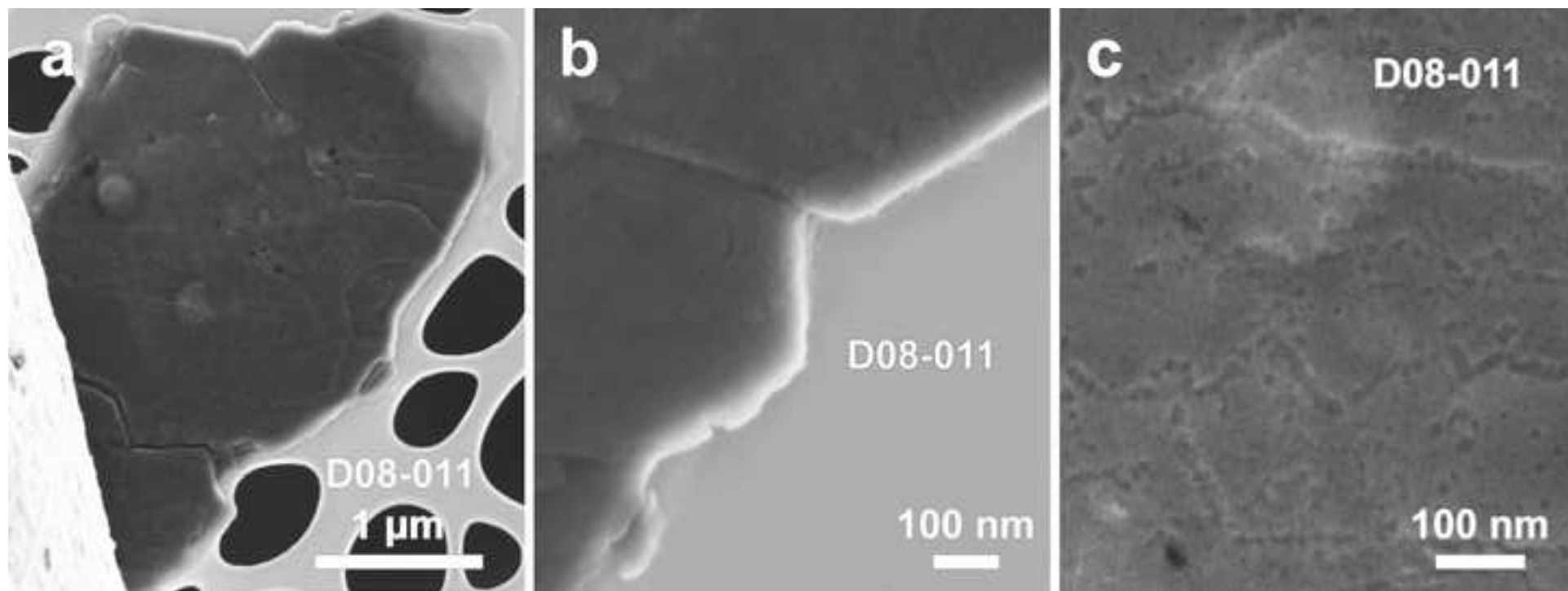
Figure 10
Click here to download high resolution image
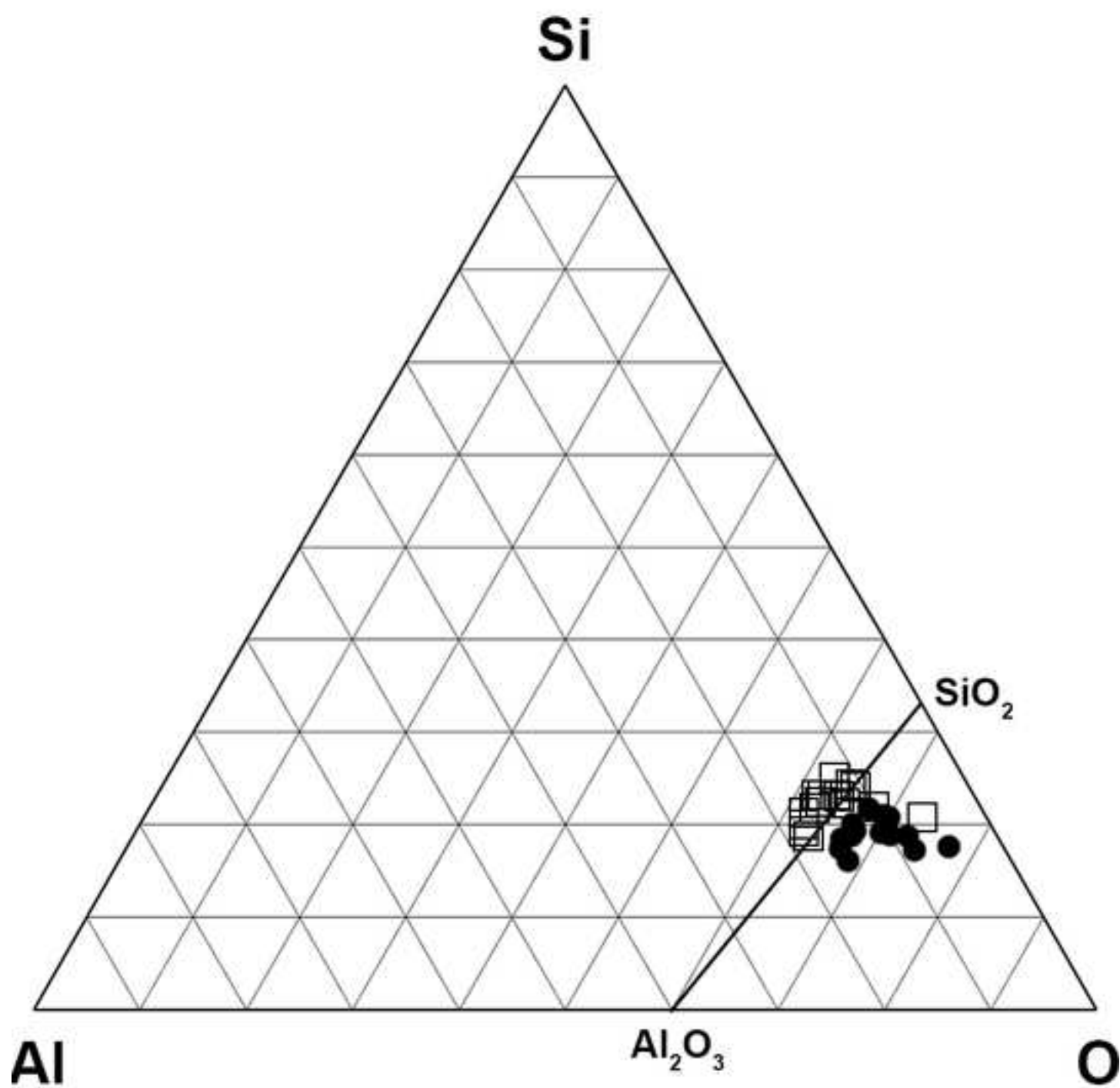
Figure 11
Click here to download high resolution image
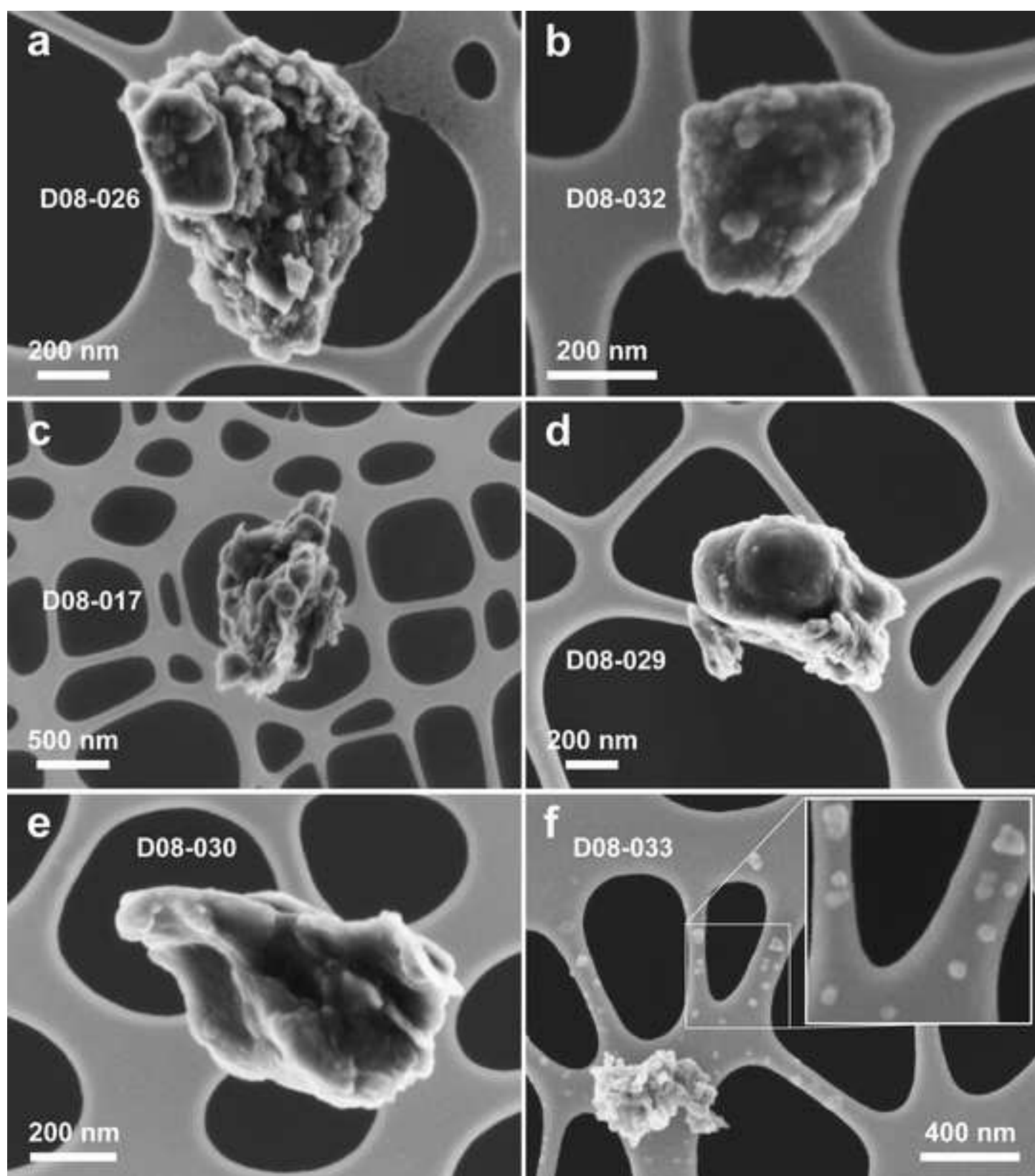
Figure 12
Click here to download high resolution image
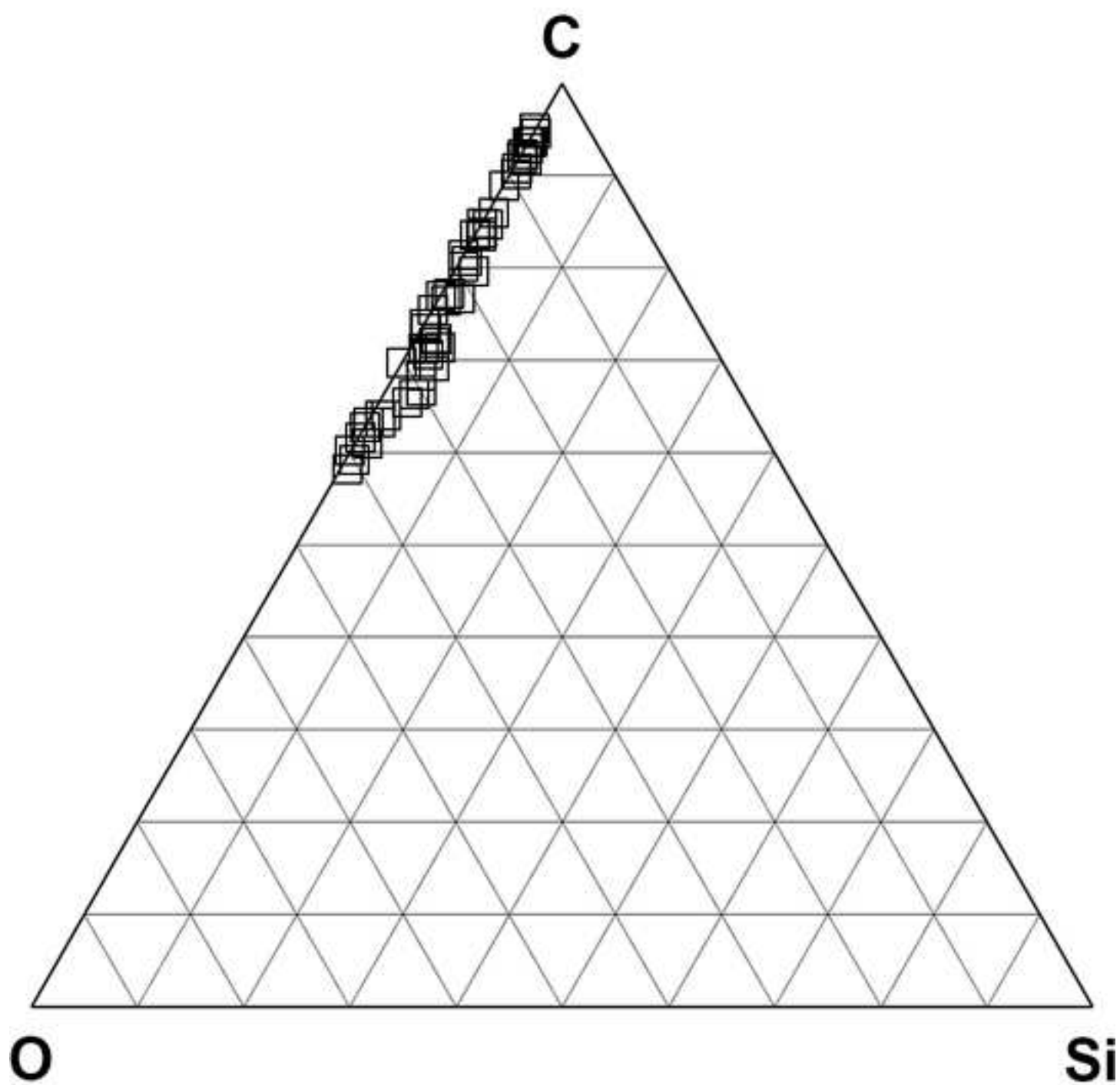
Figure 13
Click here to download high resolution image
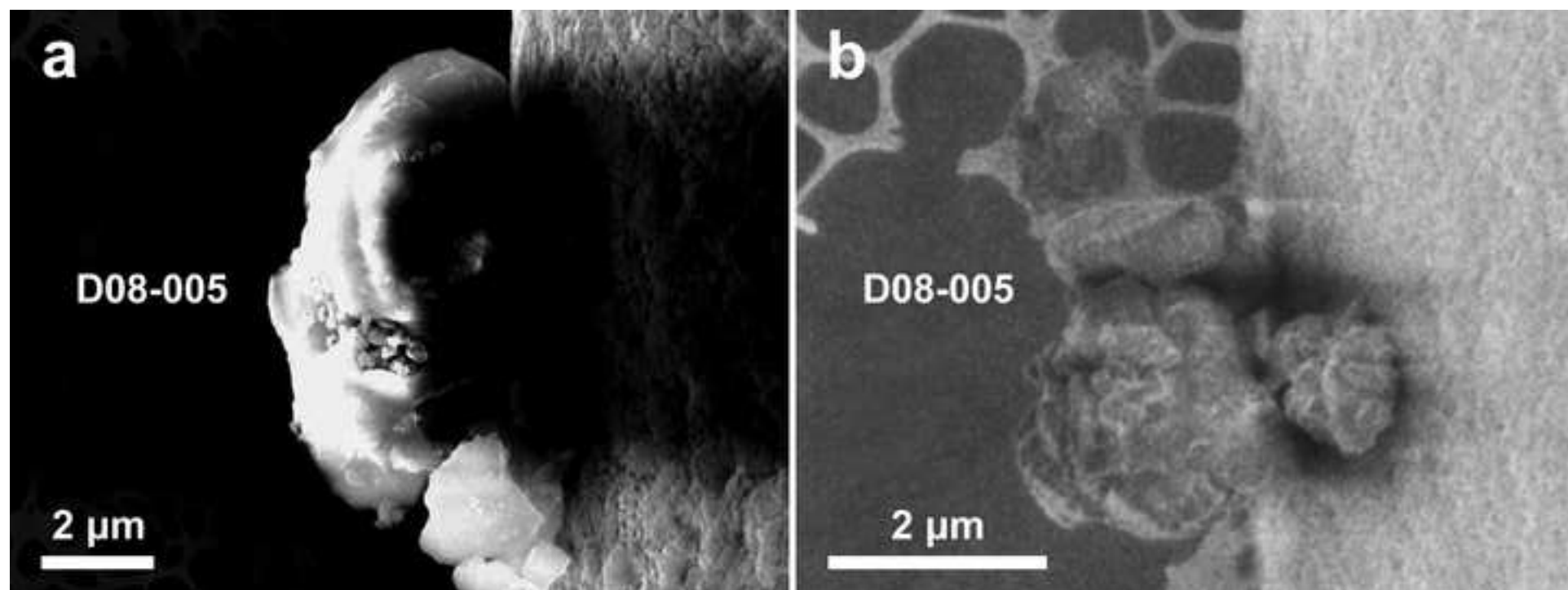
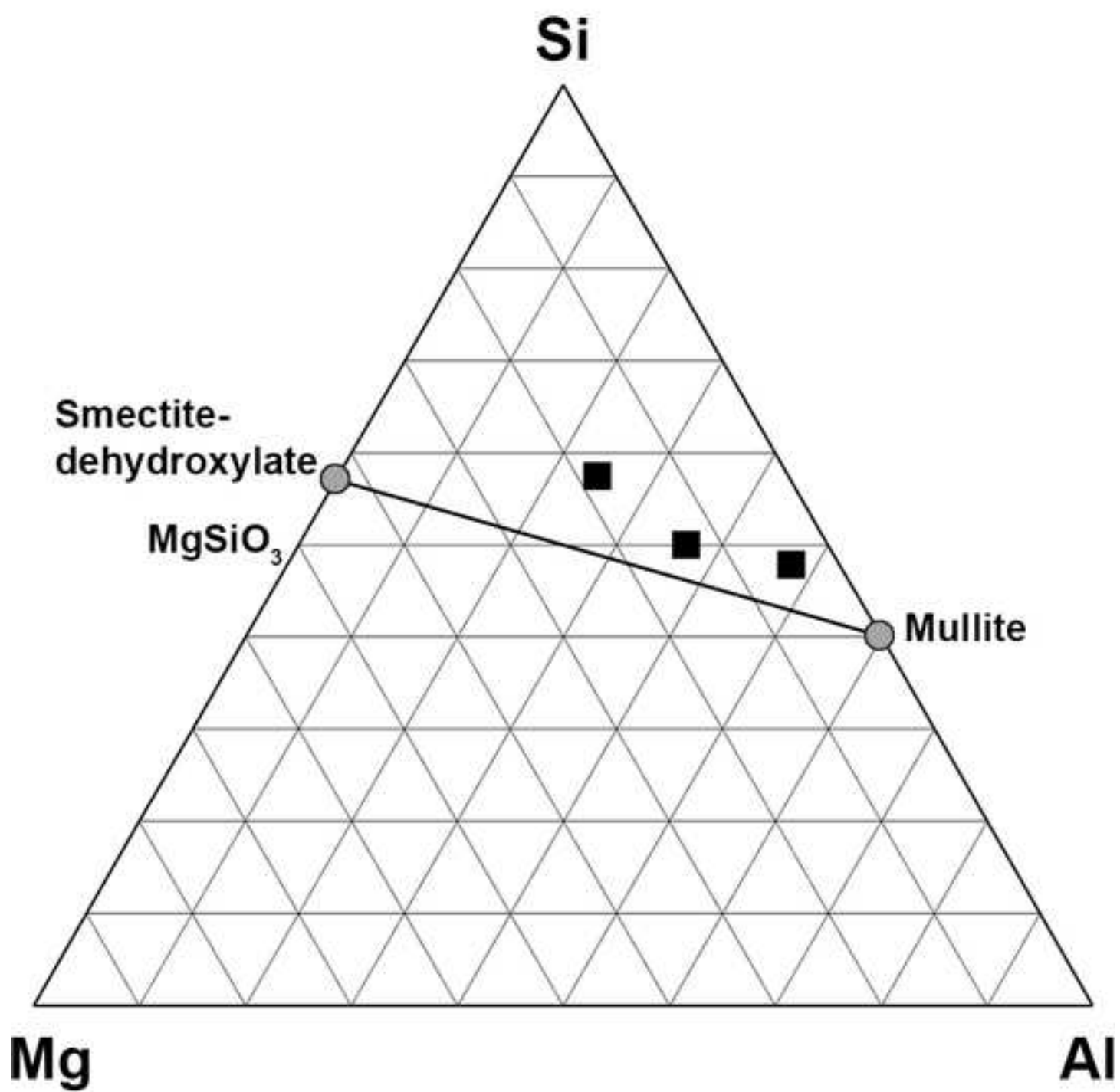**Figure 14**
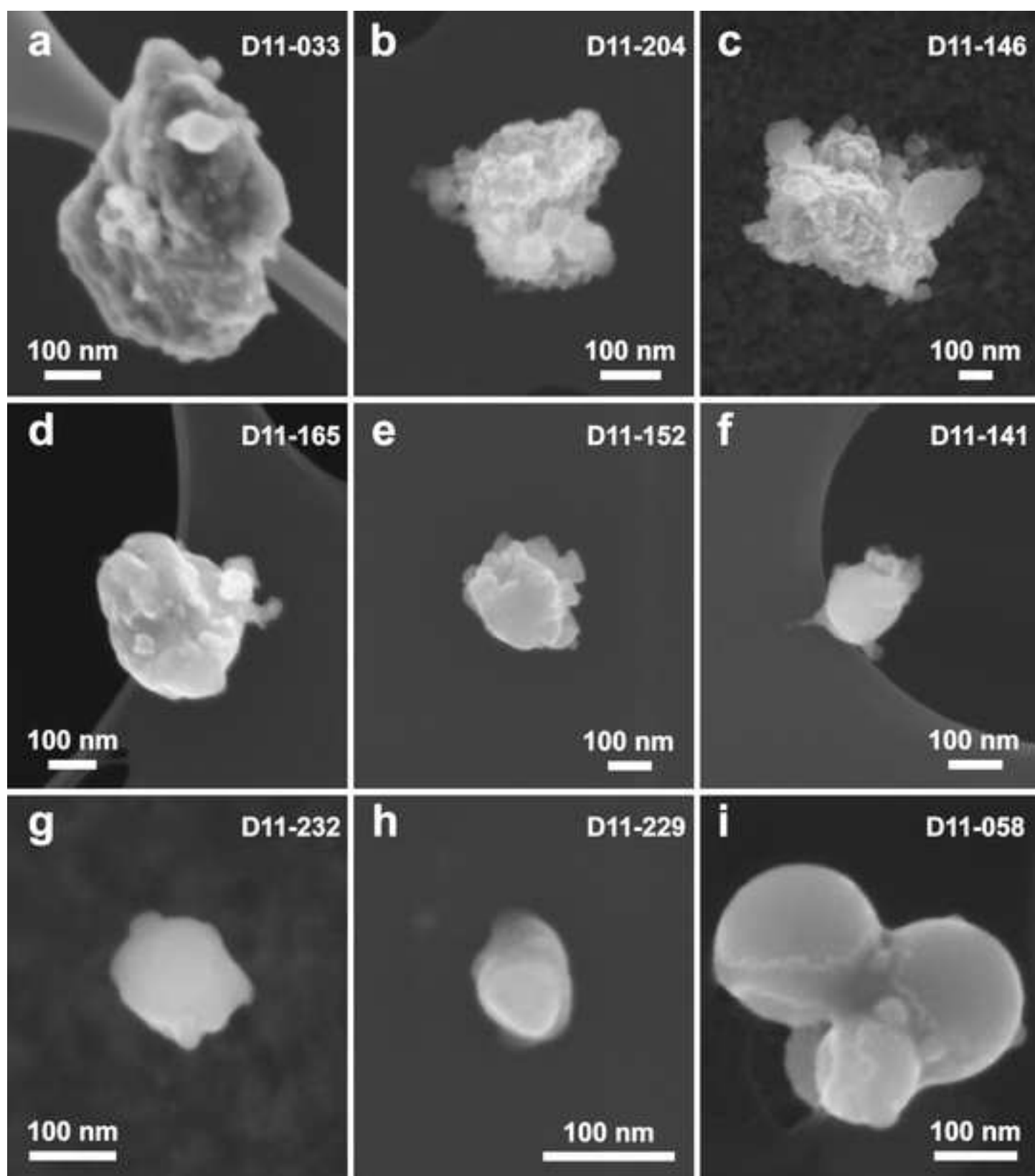[Click here to download high resolution image](#)
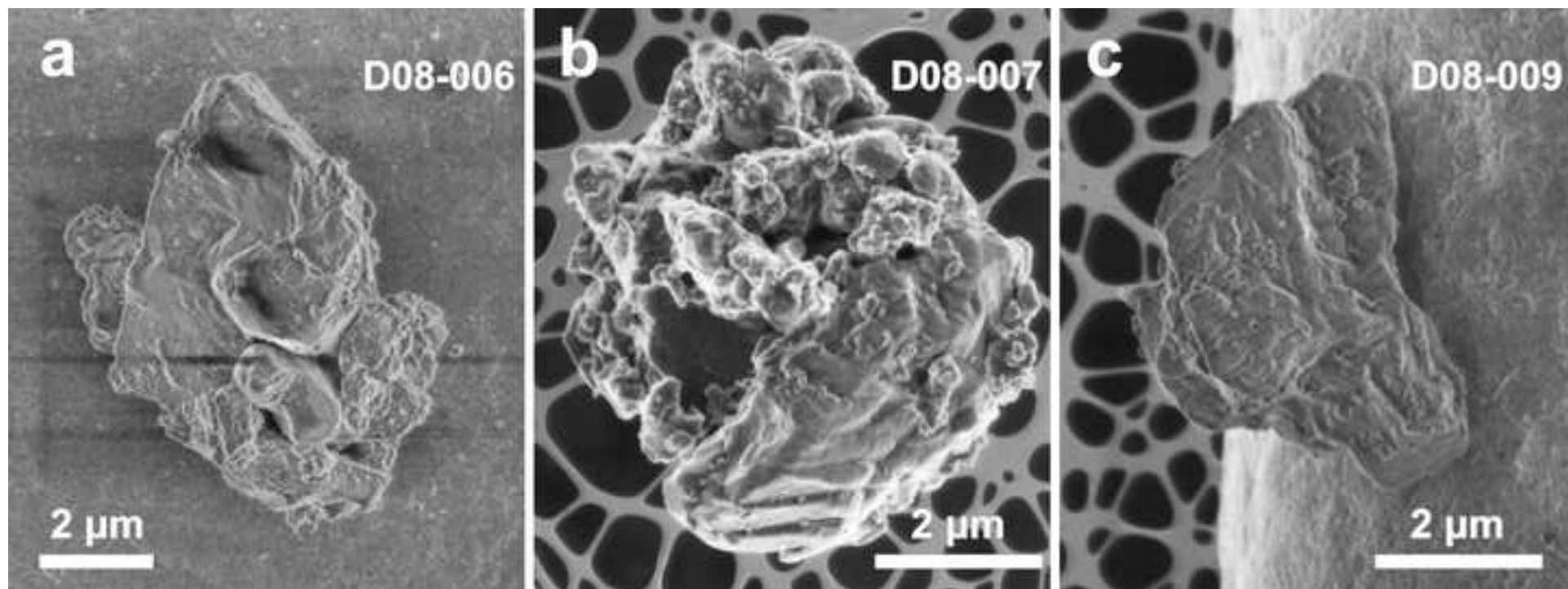
Figure 14

Figure 15
Click here to download high resolution image
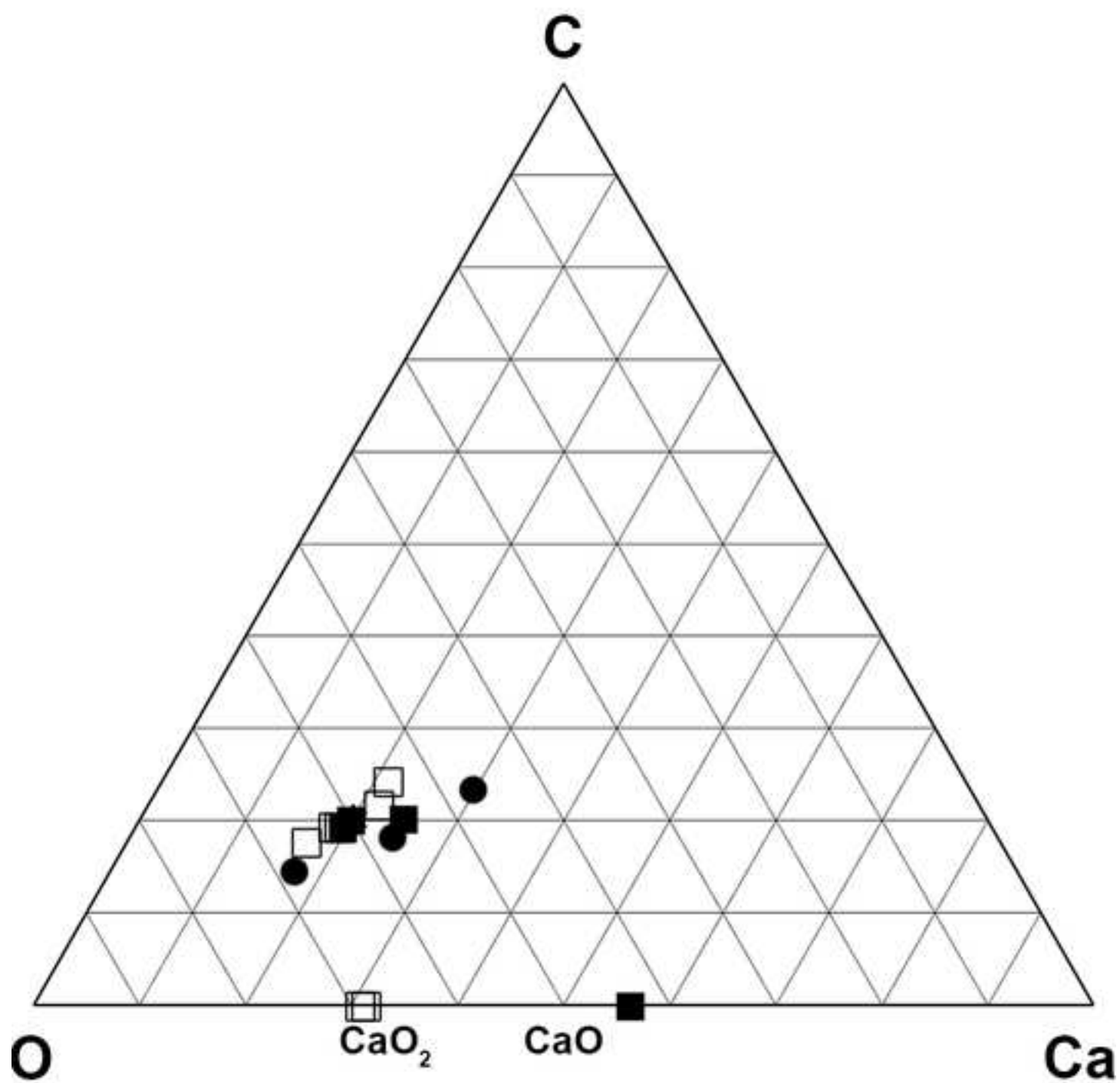
Figure 16
Click here to download high resolution image
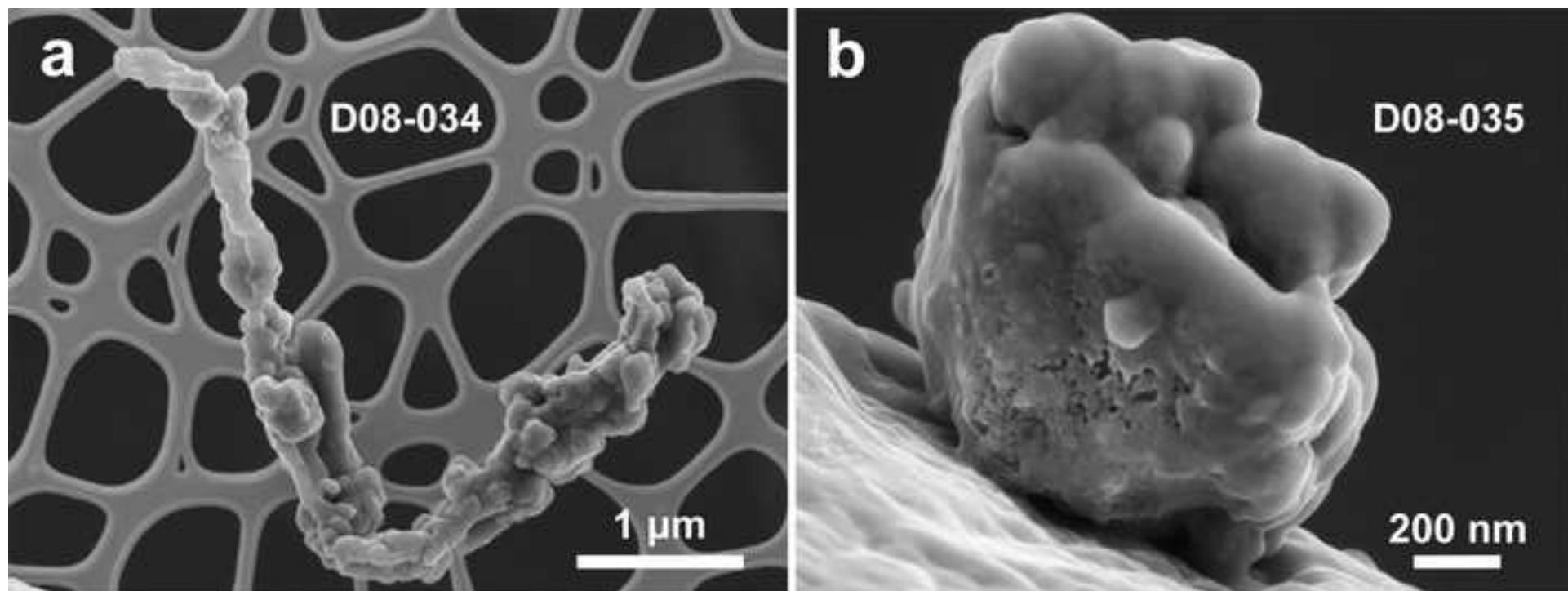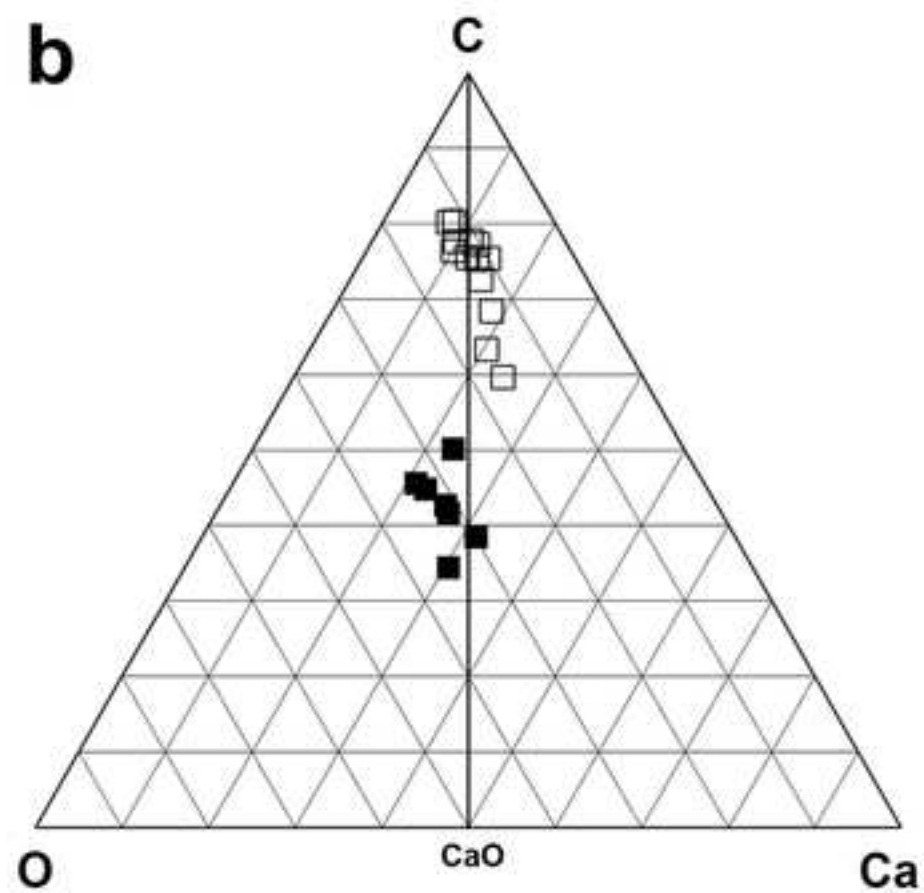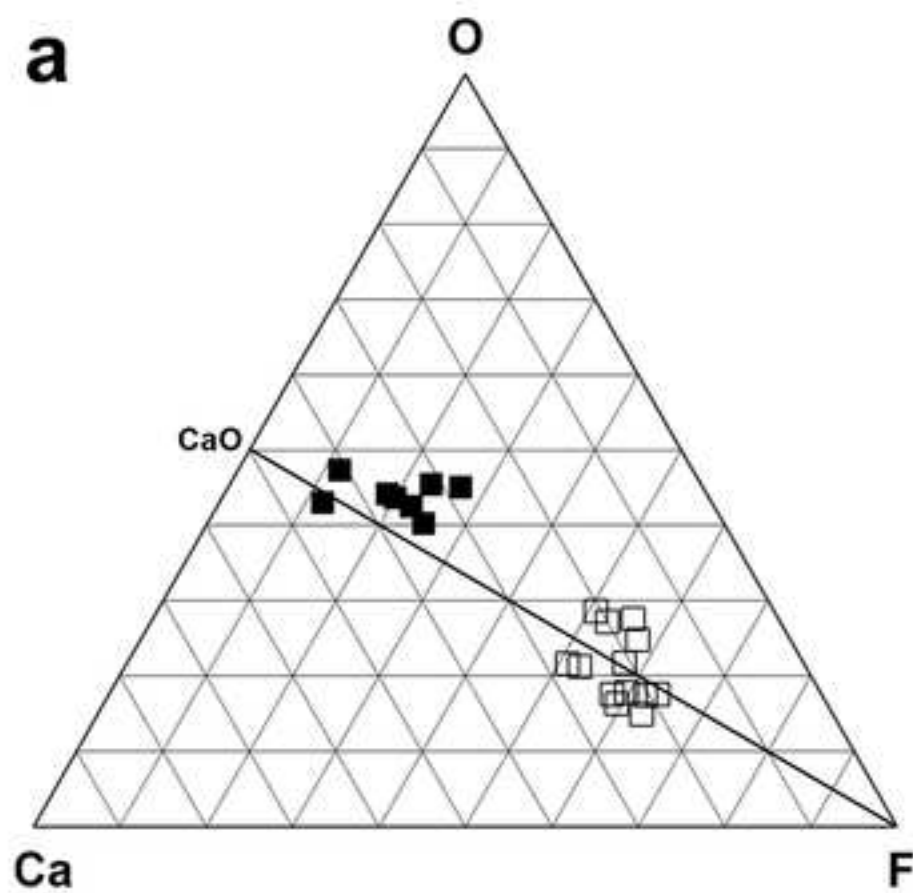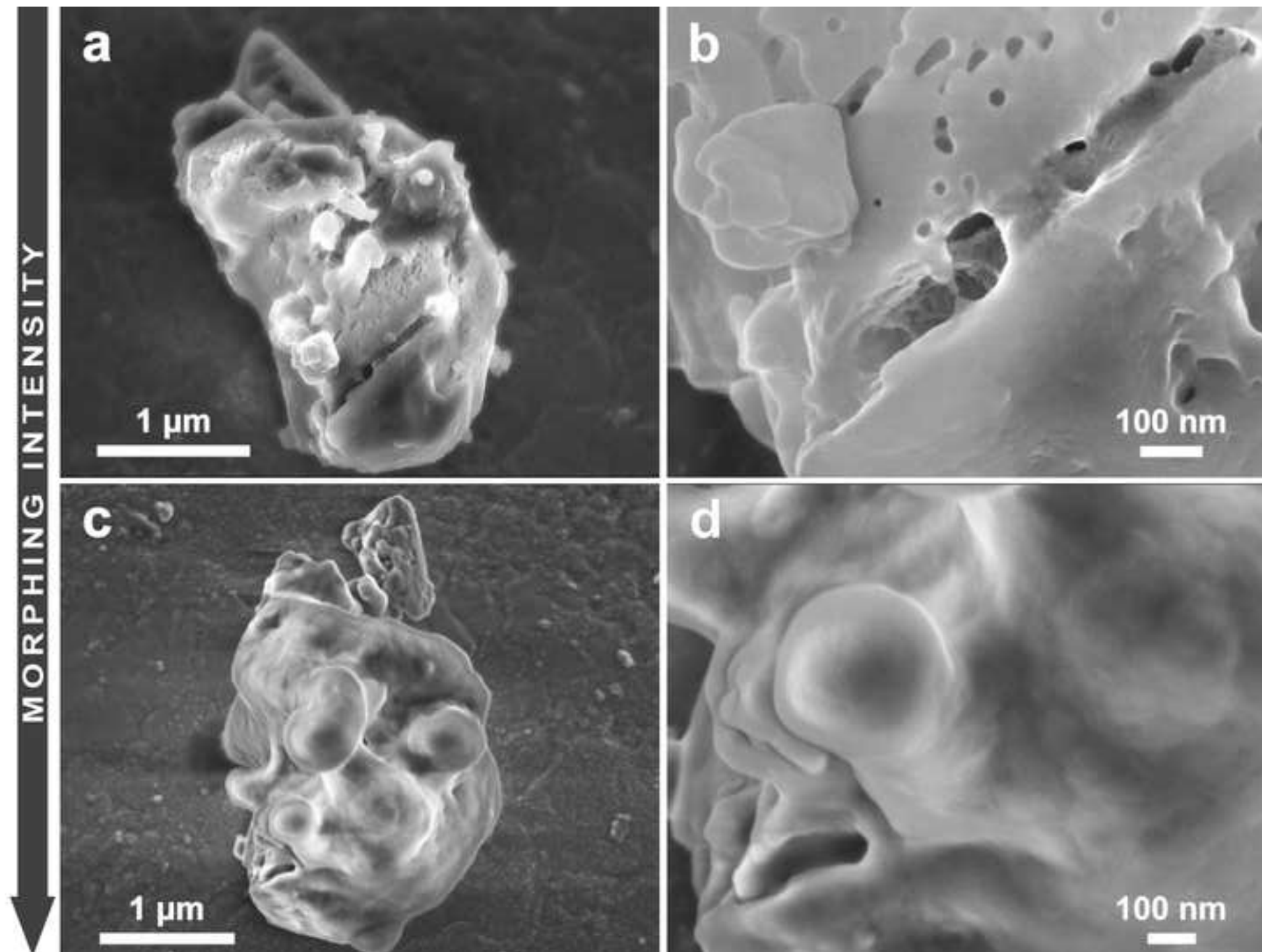
Figure 19
Click here to download high resolution image
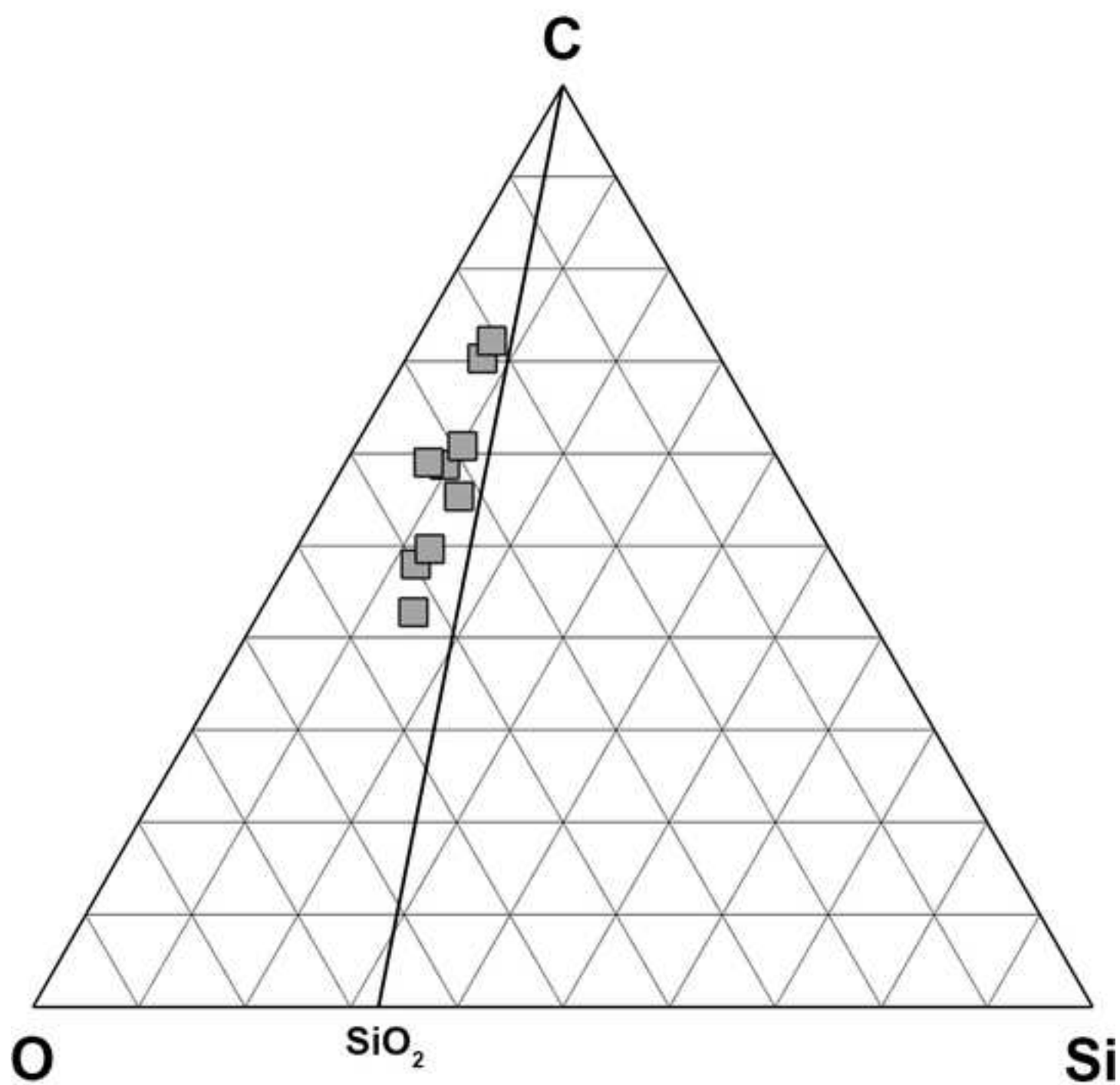
MORPHING INTENSITY
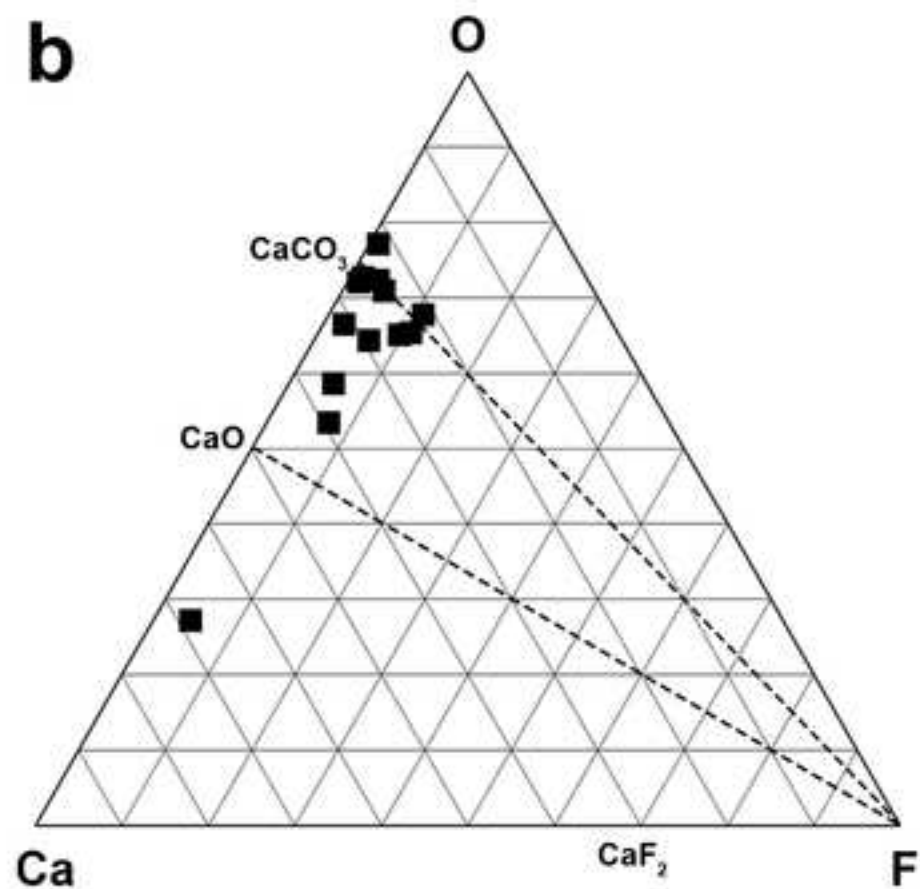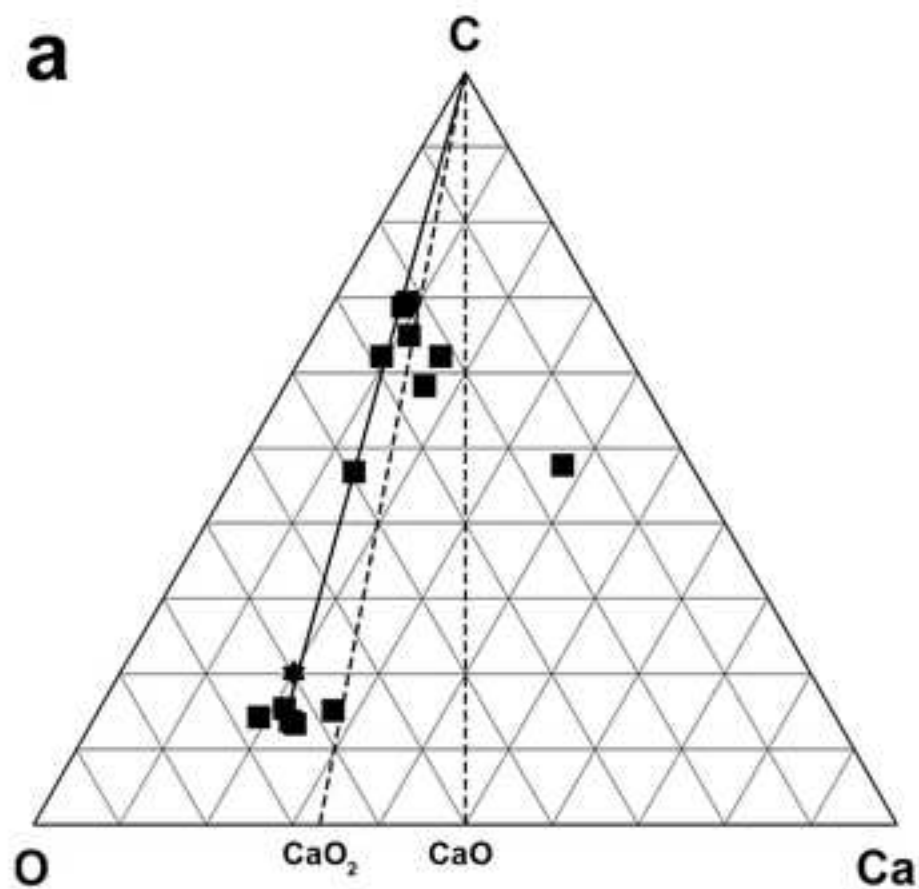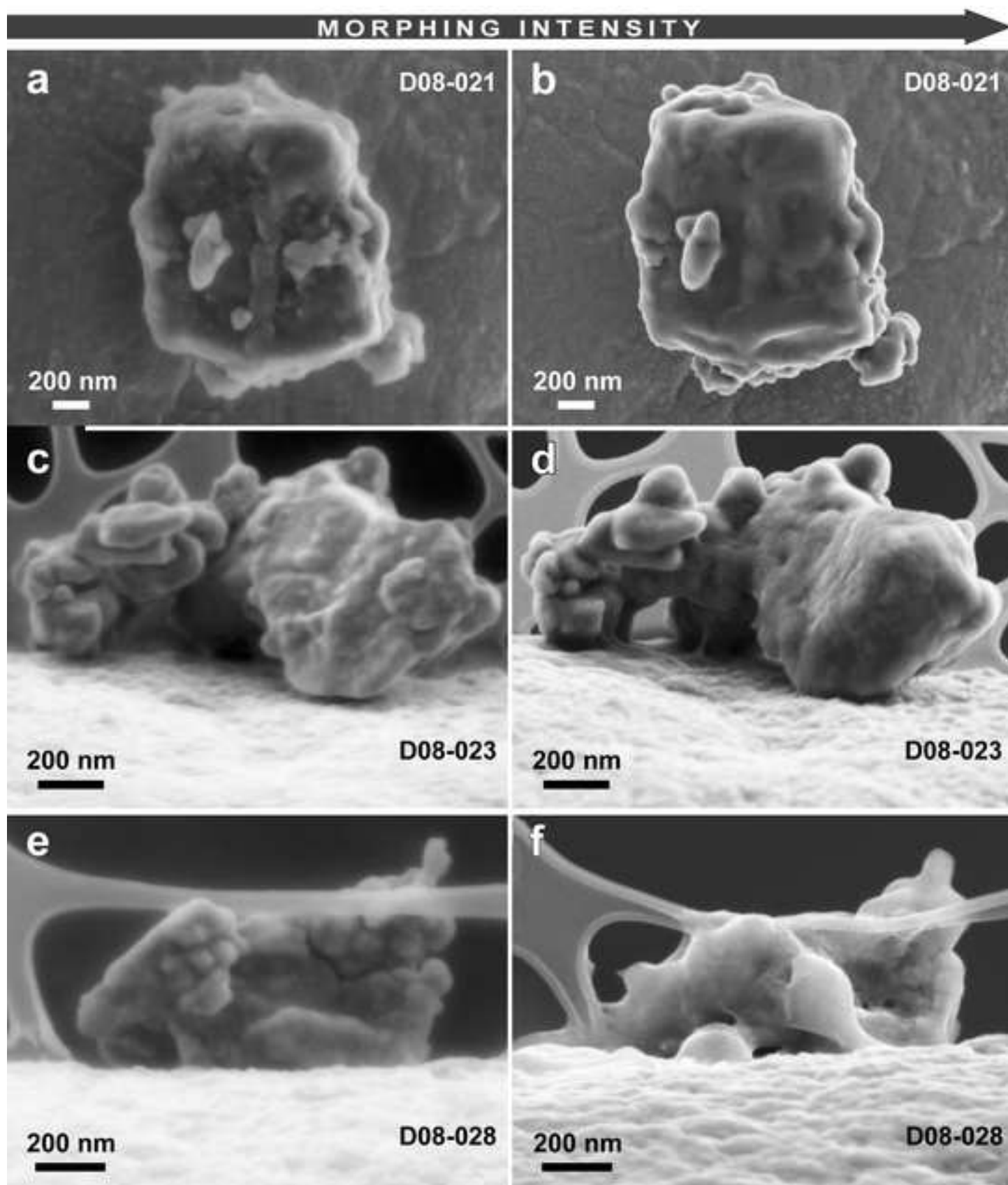
Figure 21
[Click here to download high resolution image](#)
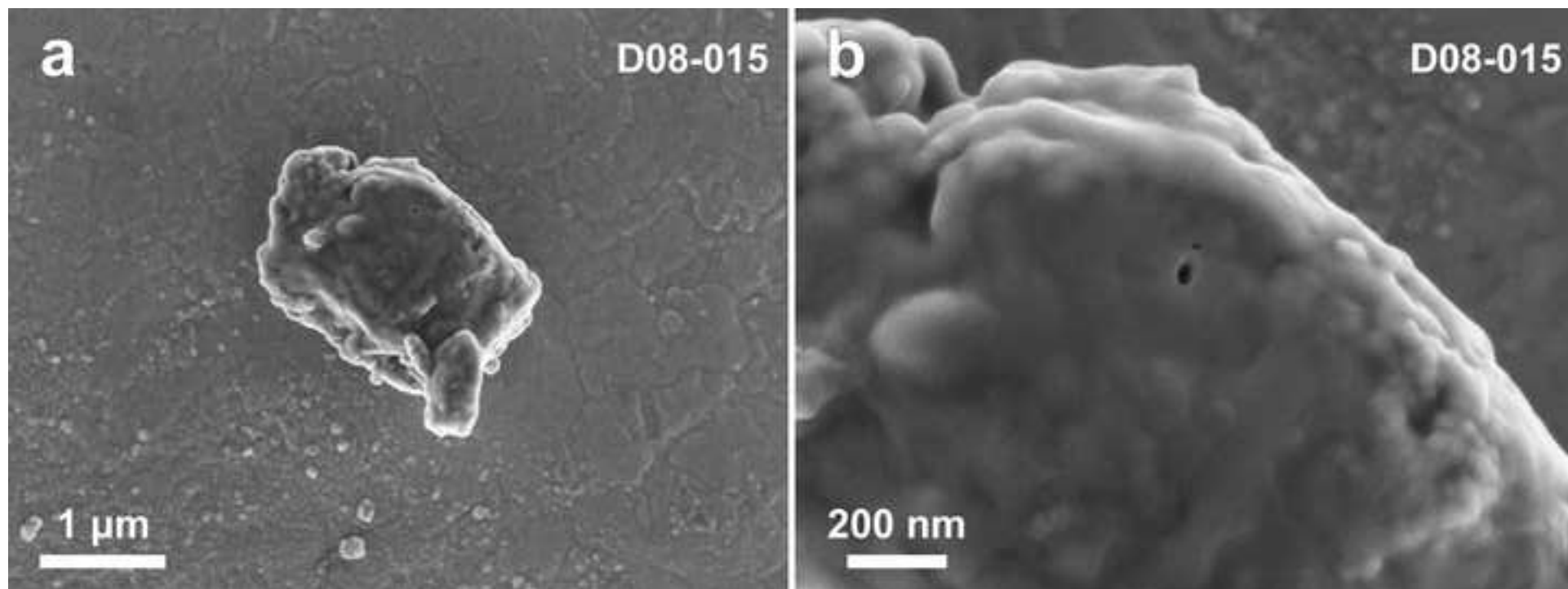
Figure 22
Click here to download high resolution image

Figure 23
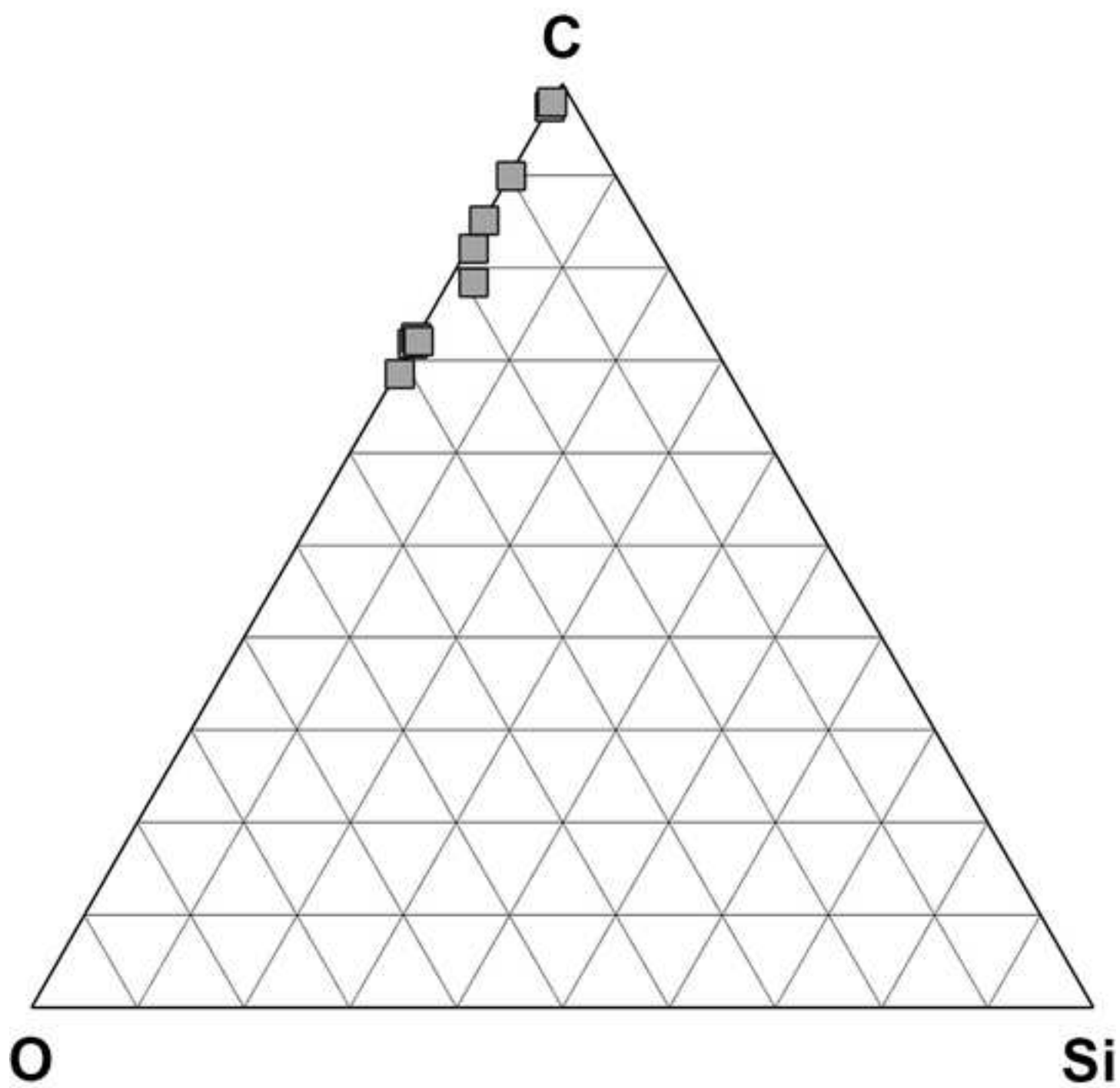**Click here to download high resolution image**

Figure 24
Click here to download high resolution image

a D11-291   100 nm
b   D11-238   200 nm
c   D11-247   1 µm

Figure 26
Click here to download high resolution image

Figure 27
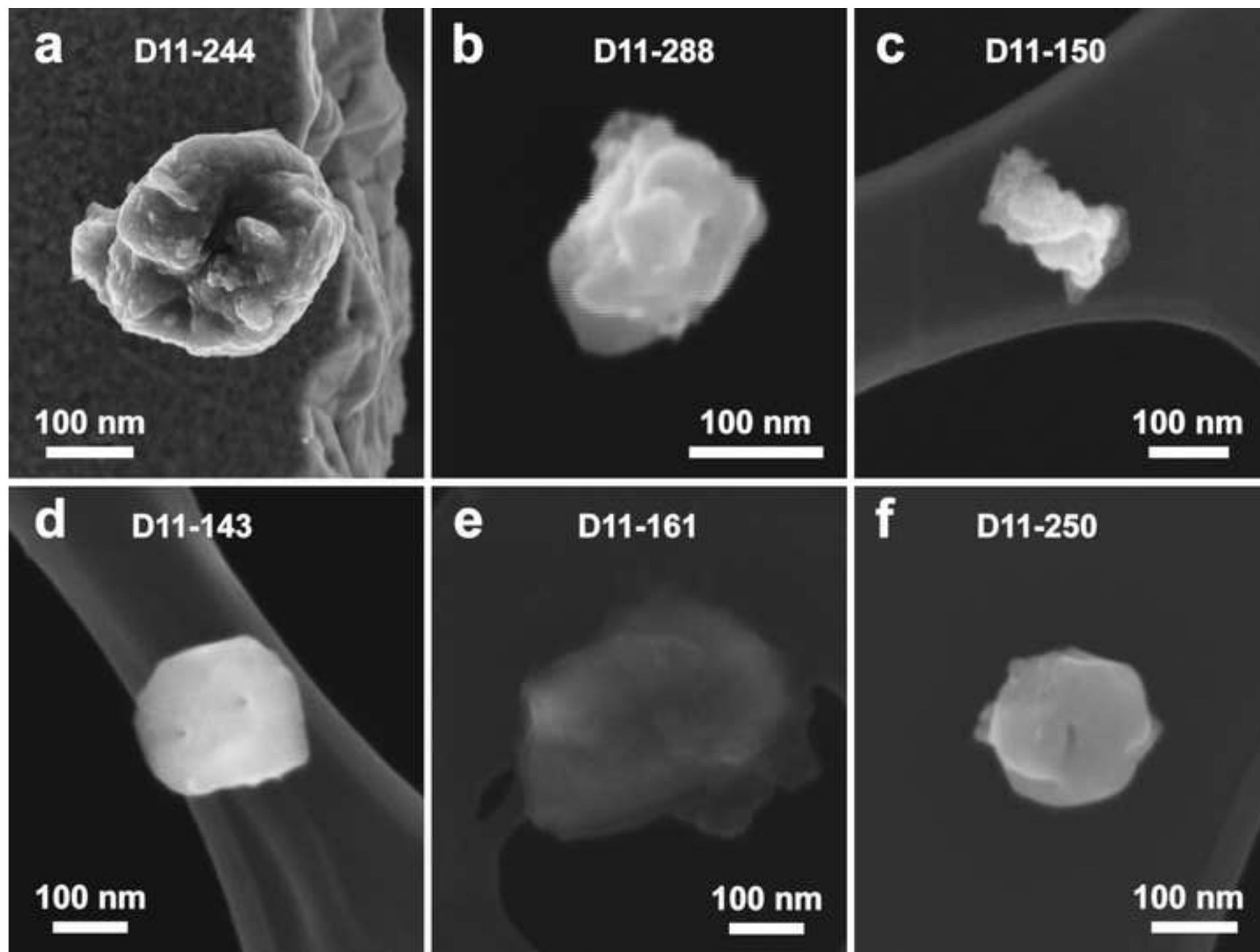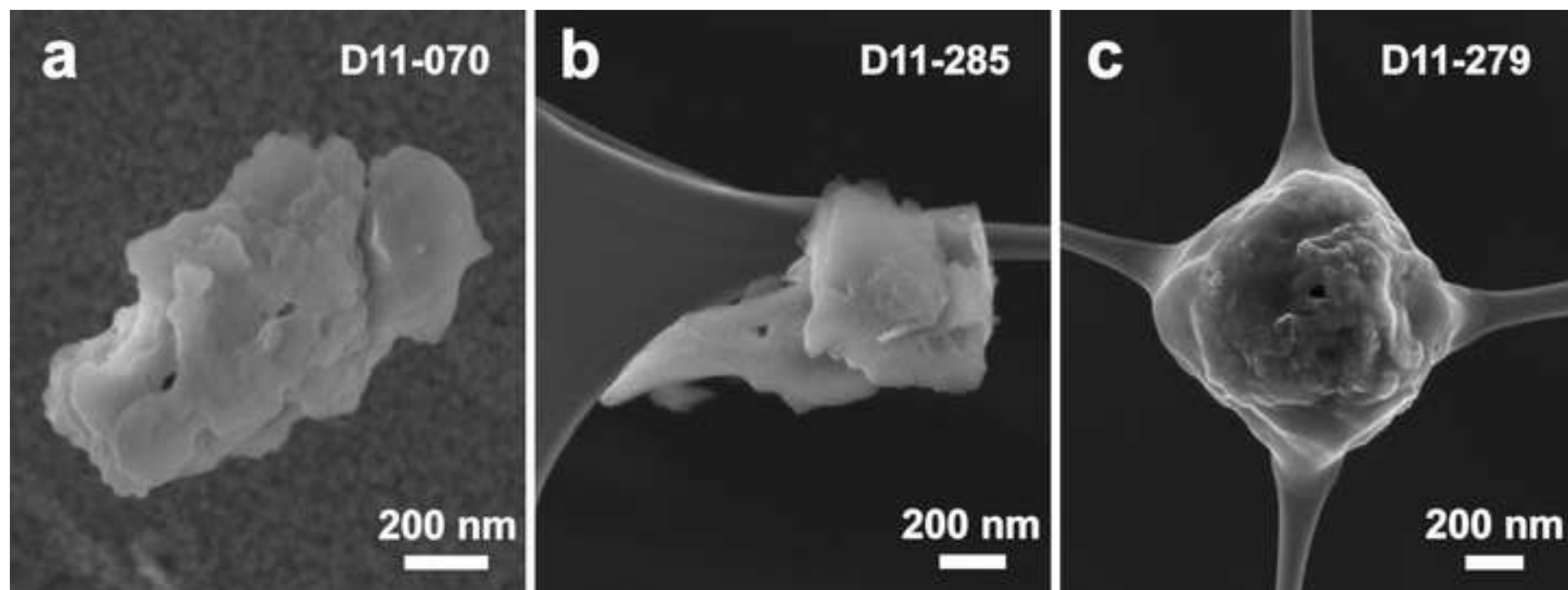**Click here to download high resolution image**

Figure 30
[Click here to download high resolution image](#)

Figure 31
Click here to download high resolution image

Figure 32
Click here to download high resolution image